# Carbide-Derived Carbon Films for Integrated Electrochemical Energy Storage

A Thesis

Submitted to the Faculty

of

Drexel University

by

Min Heon

in partial fulfillment of the

requirements for the degree

of

Doctor of Philosophy

August 2014

# DEDICATIONS

To God, for guiding me throughout the journey and to my family, for their love and prayers.

# ACKNOWLEDGEMENTS

This should be a never-ending list of names of people who have supported, and inspired me. I would like to thank Prof. Yury Gogotsi for everything. He has been the best scientist and mentor that I've ever had at schools or work through my life. Nothing could be done without his support and patience.

I also thank my committee members, Profs. Michel Barsoum, Steve May, Yossef Elabd, and Jeffrey Hettinger for their insights and advice. I also thank the faculty and staffs from Materials Science and Engineering Department at Drexel for their help and support. I give special thanks to the current and former staffs of the A.J. Drexel Nanotechnology Institute: Holly Burnside, Danielle Tadros, Jill Buckley, and Michelle Sipics for enabling us to do our work and also to the CRF staffs: Ed Basgall, Craig Johnson for their support and advice.

I am grateful for the people I've met, talked and worked together with when I was in Drexel. I thank my friends and colleagues, in no particular order, Sun-Hwa Yeon, Prof. Vadym Mochalin, Carlos Perez, Michael Naquib, Riju Singhal, Jake McDonough, Ioannis Neitzel, Prof. Volker Presser, Boris Dyatkin, Kristy Jost, Babak Anasori, Jun Jie Niu, Majid Biedaghi, Olha Mashtalir, Prof. Bastian Etzold, Patricia Reddington, Amanda Pentecost, Maria Lukatskaya, Yohan Dallagnese, Katie van Aken, Kelsey Hatzell, Jonathan Campos, Yenneeka Long, Sarit Kunz, Keiko Nakazawa.

This work is the result of collaboration with the excellent people outside Drexel. I thank Peihua Huang, who has worked most closely with me on micro-supercapacitor works over her PhD years at Université Paul Sabatier in France; David Pech and Magali Brunet of Laboratoire d'Analyse et d'Architecture des Systèmes in France, for guiding

and supporting this study; Peihua's advisor Prof. Patrice Simon and Pierre-Louis Taberna of Université Paul Sabatier for training me in their lab and shared their expertise on electrochemistry; Thomas Arruda and Nina Balke of Oak Ridge National Laboratory, who developed in-situ electrochemical AFM and tested CDC films; Prof. Jeffrey Hettinger and Prof. Samuel Lofland of Rowan University, who synthesized countless carbide films, taught me how to grow textured carbide films, and supported in every possible way for this study;

Lastly, I thank my wife, Soheon, for her love and understanding, also Joon and Jin for being my lovely boys all the time.

# TABLE OF CONTENTS

# LIST OF TABLES

# LIST OF FIGURES

# LIST OF ABBREVIATIONS

| | |
|---|---|
| AN | acetonitrile |
| BET | Brunauer Emmett Teller |
| $BF_4^-$ | tetrafluoroborate |
| CDC | carbide derived carbon |
| CN | coordination number |
| CNT | carbon nanotube |
| CVD | chemical vapor deposition |
| DTA | differential thermal analysis |
| EC | electrochemical capacitor |
| EDL | electrochemical double-layer |
| EDLC | electrochemical double-layer capacitor |
| EDS | energy dispersive X-ray spectroscopy |
| $EMI^+$ | 1-ethyl-3-methylimidazolium |
| ESR | equivalent series resistance |
| FIB | focused ion-beam |
| FTIR | Fourier transform infrared spectroscopy |
| FWHM | full width at half maximum |
| GC | galvanostatic cycling |
| GCPL | galvanostatic cycling with potential limitation |
| HOPG | highly ordered pyrolytic graphite |
| IUPAC | International Union of Pure and Applied Chemistry |
| MWCNT | multi-walled carbon nanotube |
| ND | nano-daimond |
| $NEt_4^+$ | tetraethylammonium |
| NLDFT | non-local density functional theory |
| OLC | onion-like carbon |
| PC | propylene carbonate |
| PDF | powder diffraction file |
| PECVD | plasma-enhanced chemical vapor deposition |
| PSD | pore size distribution |

| | |
|---|---|
| PTFE | polytetraflouroethylene |
| PVD | polyvinylpyrrolidone |
| PVDF | polyvinylidene fluoride |
| PZC | point of zero charge |
| QSDFT | quenched-solid density functional theory |
| RIE | reactive ion etching |
| RTA | rapid thermal anneal |
| RMC | reverse Monte Carlo |
| RTIL | room temperature ionic liquid |
| SAXS | small-angle X-ray scattering |
| SEM | scanning electron microscopy |
| SSA | specific surface area |
| SWCNT | single-walled carbon nanotube |
| TEM | transmission electron microscopy |
| $TFSI^-$ | bis(trifluoromethanesulfonyl)imide |
| TGA | thermogravimetric analysis |
| UHV | ultra high vacuum |
| VA-CNT | vertically-aligned carbon nanotube |
| XPS | X-ray photoelectron spectroscopy |
| XRD | x-ray diffraction |

# ABSTRACT

Carbide-Derived Carbon Films for Integrated Electrochemical Energy Storage

Min Heon

Advisor: Prof. Yury Gogotsi

Active RFID tags, which can communicate over tens or even hundreds of meters, MEMS devices of several microns in size, which are designed for the medical and pharmaceutical purposes, and sensors working in wireless monitoring systems, require microscale power sources that are able to provide enough energy and to satisfy the peak power demands in those applications. Supercapacitors have not been an attractive candidate for micro-scale energy storage, since most nanoporous carbon electrode materials are not compatible with micro-fabrication techniques and have failed to meet the requirements of high volumetric energy density and small form factor for power supplies for integrated circuits or microelectronic devices or sensors. However, supercapacitors can provide high power density, because of fast charging/discharging, which can enable self-sustaining micro-modules when combined with energy-harvesting devices, such as solar cell, piezoelectric or thermoelectric micro-generators.

In this study, carbide-derived carbon (CDC) films were synthesized via vacuum decomposition of carbide substrates and gas etching of sputtered carbide thin films. This approach allowed manufacturing of porous carbon films on SiC and silicon substrates. CDC films were studied for micro-supercapacitor electrodes, and showed good double layer capacitance. Since the gas etching technique is compatible with conventional micro-

device fabrication processes, it can be implemented to manufacture integrated on-chip supercapacitors on silicon wafers.

# 1. SURVEY OF LITERATURE

## 1.1. Introduction

Electricity is a form of energy that exists in nature and is not something invented. Since the Ancient Greeks discovered the static electricity by rubbing fur on amber, it has been learned and used over human history. Eventually, our lives have become too dependent on electricity that now we can't imagine how it would be to live without it. Countless scientists and engineers have contributed to not only more efficient way of generating electricity but also to better way of storing electrical energy last century. Power plants generate electricity by consuming coal, natural gas or nuclear fuel to support our lives. And numerous energy storage technologies are being utilized to keep electricity from being wasted and to make electricity usable off the grid. It includes batteries, compressed air energy storage, electrochemical capacitors, pumped hydro storage, flywheel storage, thermal energy storage, and superconducting magnetic energy storage. The need for improved electrical energy storage technology is imperative as our world becomes increasingly electrified and at the end of the day, Earth will run out of finite resources to generate electricity.

Capacitors store electrical charge with no chemical or phase changes and the process is highly reversible and the charge-discharge cycle is virtually without limit. Electrochemical capacitors (ECs) also called 'supercapacitors' or 'ultracapacitors', store electrical charge in an double layer at the interface between a high-surface-area carbon electrode and a liquid electrolyte.[1, 2] As a result, they are also often referred to as electrochemical double layer capacitors (EDLCs).

Ever since the first double layer capacitor technology was patented in 1950's, porous carbon materials have been widely utilized as electrodes for EDLCs because of its superior properties such as large surface area, high electrical conductivity, chemical stability and low cost.[1, 3] Over past decades, a wide variety of high surface area carbons have been developed for electrochemical double layer capacitors; activated carbons,[4, 5] carbon aerogels,[6-9] carbon nanotubes,[10-13] and template carbons[14-17]. Supercapacitors, Ultracapacitor® or Electrical Double Layer Capacitor are the device storing electrical energy by electrosorption of ions on the electrode surface. As ion sorption occurs quickly within very near distance to the electrode surface, EDLCs can provide high power which means more current in relatively short period time. Even though enormous effort has been put into developing porous carbon electrode materials to enhance the energy density, any of the mentioned carbon materials were not good enough to fill the fundamental gap between Lithium-ion batteries using redox reaction of Li ion throughout the electrode and supercapacitors using electrosorption onto the surface. Pseudocapacitors, a branch of EDLC family that takes advantage of electrosorption as well as redox reactions are receiving more attention.[1, 18, 19] However redox reactions of active pseudocapacitive material require relatively high volume changes which limit its life span and cyclability. Mainly due to the gap coming from energy storage mechanism, porous carbon materials have not been applicable to commercialization due to poor competitiveness in cost and manufacturing processes. Most of today's commercial electrochemical capacitors use activated carbon-based electrodes in organic electrolytes and these supercapacitors are already widely used in our daily life: the power for high bright LED flash in digital cameras, the backup power sources in the copy machines, the power boosters for forklifts

and cranes, the street lamps and signals in combination with solar panels, and the hybrid power sources for electric vehicles.

As mobile electronics is expanding its territory and MEMS (Micro-Electro-Mechanical System) technology is stepping up from fundamental to practical applications, microscale on-chip power storages receive increased attention. Activated carbon has been widely used as electrode material for regular electrochemical capacitors of canned or pouched types, however it is not the best option for microscale energy storage devices for portable applications. Primarily, the powder form limits activated carbon electrodes from being applied for powering mobile electronics or MEMS.

Recent report of a monolithic porous carbon film synthesized from bulk TiC ceramics showed clearly that porous carbide-derived carbon (CDC) thin films have a great potential for thin film electrochemical capacitors.[17] Elimination of polymer binder and no macropores between the particles are great advantages of thin film form of CDC.[17] The continuous porous carbon film on the Si wafer is expected to take current electrochemical capacitor technologies to another level, enabling utilization of a variety of conventional thin film device manufacturing processes and integration of supercapacitors and batteries on semiconductor chips.

## 1.2. Electrical Double-Layer Capacitors (EDLCs)

Supercapacitors, ultracapacitors or electrochemical double layer capacitors (EDLCs) are commonly used names for a class of electrochemical energy storage devices that are ideally suited to the rapid storage and release of electrical energy.[20] Electrochemical capacitors (ECs) store far more energy (capacitance per unit volume) than conventional

electrostatic or electrolytic capacitors due to their high porosity carbon electrode material that has inherited high surface area for electrostatic charge storage in double layers.[21]

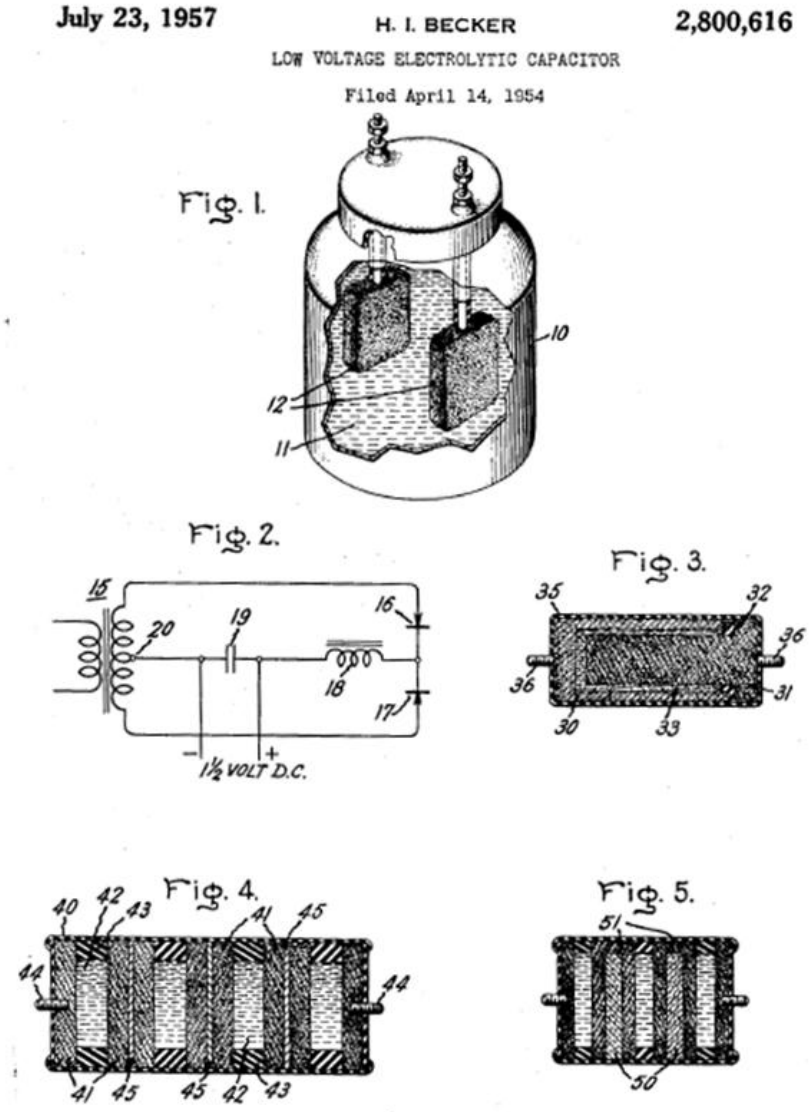


Figure 1.1: Schematic of the first the first Electrical Double Layer Capacitor (EDLC) developed in 1957.[22]

The first double layer capacitor concept developed by General Electric Co was a container holding electrolyte with two electrodes immersed in, which did not make it to commercialization. Even the inventor thought of it as electrolytic capacitor technology, therefore it was patented with a title as 'Low Voltage Electrolytic Capacitor'. Later, Standard Oil Company of Ohio (SOHIO) introduced a electrochemical capacitor using porous carbon in a non-aqueous electrolyte, which is regarded as the invention of the EDLC device in the form now commonly used.[23, 24] Later on, NEC released a EDLC product named SuperCapacitor™ that is a first successful commercialized EDLC in 1978. Since then, EDLCs have evolved through several generations of design. Their initial application was backup power devices for chips and computer memories. With increasing electrification of technology, many other applications have emerged such as compact portable electronic devices, wearable electronics, medical applications, high-power electronics, and hybrid electric propulsion systems. On the whole, EDLCs can complement the demerits of other electric energy storages - batteries and fuel cells - and have unique characteristics of high power density (fast charging/discharging), long life cycle (≥100,000 cycles), and wide operating temperatures.[25]

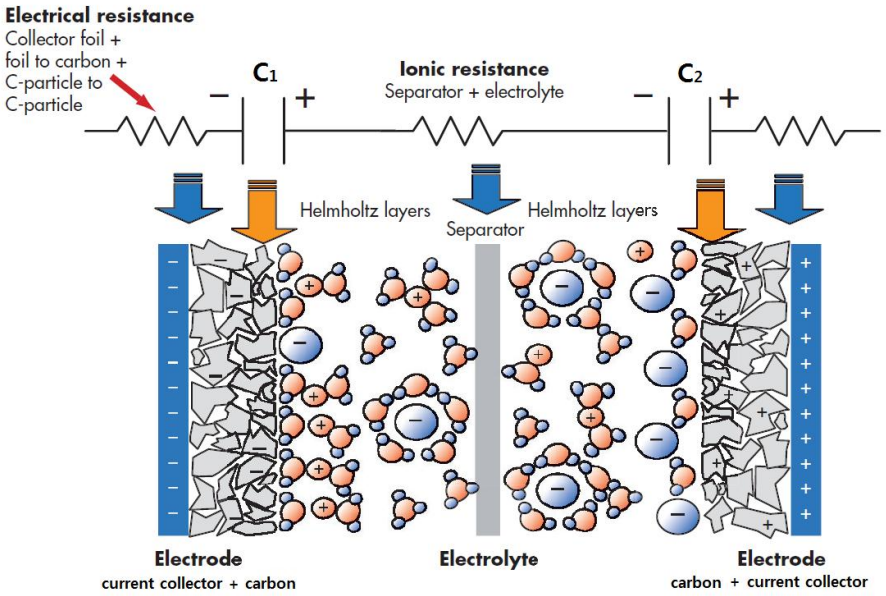


Figure 1.2: An electrochemical capacitor is consisted of two plates and a separator suspended in an electrolyte. The positive plate attracts negative ions in the electrolyte. The negative plate attracts positive ions. This creates what is known as an electrochemical double layer capacitor.[26]

Electrochemical capacitors store energy like batteries but in a different way. EDLCs store electrical charges by ion sorption on the surface of electrodes, physically without chemical reactions, thus the process is highly reversible and the discharge-charge cycle wouldn't degrade the performance theoretically. Also, this is inherently rapid because it simply involves movement of ions to and from electrode surfaces.[20] Each electrode is equivalent to a capacitor with capacity given by the classical formula[1]:

$$C = \frac{\varepsilon S}{d} \qquad (1)$$

where S is the surface area of the electrode/electrolyte interface, ε is the permittivity or dielectric constant, and d is the double layer thickness. As d is within the order of a nanometer, the specific capacity is very high, ~0.1 F/m$^2$.[27]

The basic structure of electrochemical capacitors is the same as electrolytic capacitors or batteries. It has two electrodes immersed in an electrolyte with an ion-permeable separator placed between the electrodes (Fig.1). For a capacitor with similar electrodes, the cell capacitance ($C_{Cell}$) can be calculated as follows:

$$\frac{1}{C_{Cell}} = \frac{1}{C_1} + \frac{1}{C_2} \qquad (2)$$

where $C_1$ and $C_2$ represent the capacitance of two electrodes respectively. Each electrode-electrolyte interface is regarded as a capacitor, therefore one cell can be considered as two capacitors in series.

### 1.2.1. Electric Double Layer

The basic principle of electric double layer lies in capacitive properties of the interface between a solid electronic conductor and a liquid ionic conductor. This was discovered by Helmholtz in 1853. Energy storage is obtained by a space charge created at solid/liquid interface under the electrostatic influence of the applied voltage. This space charge is called electric double-layer, and its thickness is limited to some nanometers, which is dependent on solvent ions.[28]

1) Helmholtz's Model: Helmholtz was the first to inquire into the capacitive phenomenon at the interface between a solid electronic conductor and a liquid ionic conductor. The interface was modeled by surface charges.

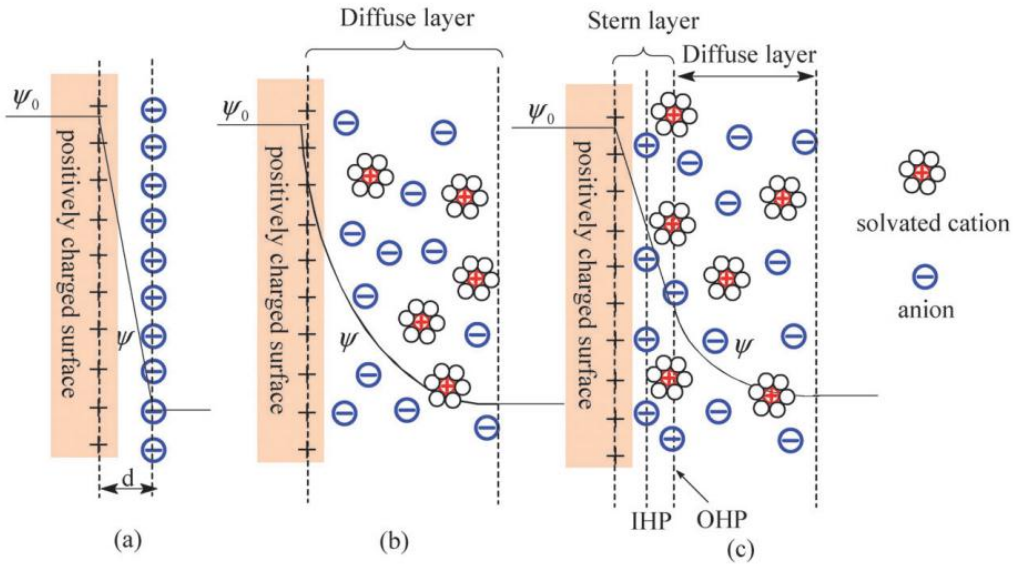


Figure 1.3: Models of the electrical double layer at a positively charged surface: (a) the Helmholtz model, (b) the Gouy–Chapman model and, (c) the Stern model.[29]

The surface capacitance C* here is simply given by:

$$C^* = \frac{\varepsilon}{d} \qquad (3)$$

where ε represents the dielectric permittivity of the solvent, and d represents the thickness of the electric double layer, which is equivalent to the solvent molecular size in this model. This model predicts capacitance larger, by more than an order of magnitude, than experimentally observed, because it assumed that surface charges distribute evenly on the interface from both sides, which is not available on electrolyte side due to poor electrical conductivity. Also this model can't take into account voltage dependence of the capacitance.

2) Gouy and Champman's Model[30, 31]: Gouy introduced random thermal motion to the model to describe the voltage dependence of the capacitance. It led to a space distribution of ionic charges in the electrolyte, which is known today as diffused layer (Figure 1.4)

The mathematical formulation of the Gouy diffused layer was established by Chapman in 1913, which were based on Poisson equation and Boltzmann distribution function.

In this model, the surface capacitance at the interface is given by:

$$C_d^* = z\sqrt{\frac{2qn_0\varepsilon}{u_T}}\sinh\left(\frac{z\Psi_0}{2u_T}\right) \qquad (4)$$

where z is the valence of electrolytic ions, $n_0$ is the concentration of ions at thermodynamic equilibrium, ε is the dielectric permittivity of the electrolyte, q is the electric charge, k is the Boltzmann constant, T is the temperature, and $u_T$ is the thermodynamic potential unity ($u_T = kT/q$).

3) Stern's Model[32]: Stern improved the Gouy and Chapman's model further by introducing dimensions of ions and solvent molecules and also by dividing the space charge in two distinct regions; a compact layer (also known as Stern layer) and a diffused layer.

The capacitance C* of the electric double-layer is therefore represented by a combination of the capacitance $C_S$* of the Stern Layer, and the capacitance $C_d$* of the diffused layer:

$$\frac{1}{C^*} = \frac{1}{C_S^*} + \frac{1}{C_d^*} \qquad (5)$$

Still $C_d^*$ is governed by Gouy and Chapman's formula with surface potential $\Psi_0$ replaced by $\Psi_d$. Therefore, the capacitance of diffused layer contributes significantly to the total capacitance of the electric double-layer at low potential levels and becomes negligible especially in concentrated electrolytes.

### 1.2.2. ELECTROLYTES

Electrochemical capacitors use aqueous or organic electrolytes, which limits the operating voltage to ~1.2 V and ~3 V respectively. When ECs go over this cell voltage, bubbles will form on the electrode surface resulting in decreasing capacitance, which indicates electrolyte decomposition. More importantly, energy stored in ECs is proportional to voltage squared according to the formula[33];

$$E = \frac{1}{2}CV^2 \quad (6)$$

$$P = \frac{V^2}{4R_S} \quad (7)$$

where E is energy, C is specific capacity, V is operating voltage, P is power, and $R_S$ is the internal resistance or equivalent series resistance (ESR) of the supercapacitor.[27]

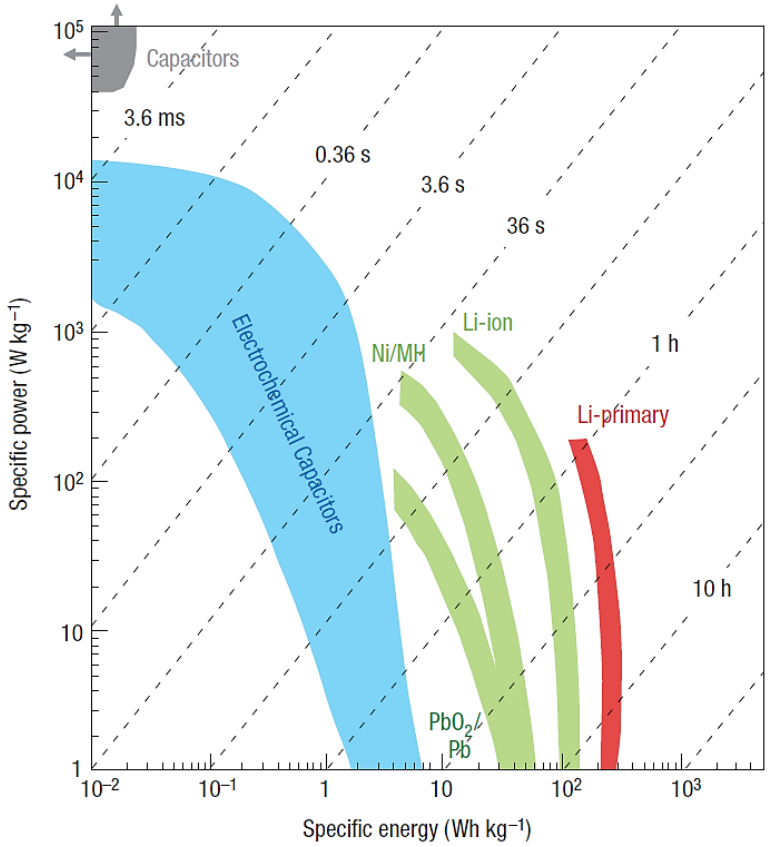


Figure 1.4: Specific power against specific energy, also called a Ragone plot, for various electrical energy storage devices.[33]

That is why organic electrolytes are more widely used than aqueous ones. However there is a tradeoff; aqueous electrolytes with relatively low breakdown voltage have higher ion conductivity but non-aqueous electrolytes have lower ion conductivity. For most bulky devices applications, this doesn't affect its performance. Total energy capacity is more important in most applications. Hence, to increase the energy storage capacity of the EDLCs, ionic liquid electrolytes with higher cell voltage are being studied widely and intensively.[34]

### 1.2.3. ELECTRODES

Since the crude porous carbon was used for the first electrochemical capacitor developed by General Electric back in 1957, carbon has been known a most ideal material for electrochemical capacitors.[22]

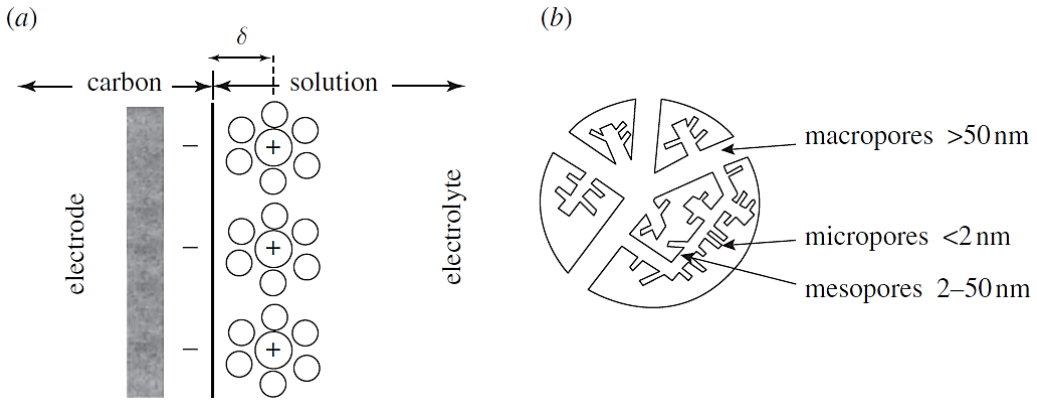


Figure 1.5: (a) Cation adsorption onto the surface of a negatively polarized electrode, charging the double-layer capacitance. (b) Pores created inside a carbon particle (about 10 mm in diameter) to develop a high surface area.[35]

Activated carbon and its close relatives in carbon family such as carbon black, carbon aerogel, carbon fiber, carbon nanotube, graphene and composites of those different carbon forms with/without binding polymers, have been employed. Carbon has unique combination of chemical and physical properties namely: high conductivity, high surface-area, good corrosion resistance, high temperature stability, controlled pore structure, processability and compatibility in composite materials, low specific weight and relatively low cost.[20] However, activated carbons that have a high surface area do not offer pore size tunability required for use of various electrolytes.

Table 1.1 Typical values for electrochemical double-layer capacitance of carbonaceous materials.[1]

| Carbonaceous material | Electrolyte | Capacitance ($\mu F/cm^2$) | Remarks |
|---|---|---|---|
| Activated carbon | 10% NaCl | 19 | Surface-area 1200 $m^2/g$ |
| Carbon black | 1M $H_2SO_4$ | 8 | Surface-area 80-230 $m^2/g$ |
| | 31 wt.% KOH | 10 | |
| Carbon fiber cloth | 0.51M $Et_4NBF_4$ in PC | 6.9 | Surface-area 1630 $m^2/g$ |
| Basal plane | 0.9N NaF | 3 | Highly oriented pyrolytic graphite |
| Edge plane | 0.9N NaF | 50–70 | |
| Graphite powder | 10% NaCl | 35 | Surface-area 4 $m^2/g$ |
| Graphite cloth | 0.168N NaCl | 10.7 | Surface-area 630 $m^2/g$ |
| Glassy carbon | 0.9N NaF | ~13 | Solid |
| Carbon aerogel | 4M KOH | 23 | Surface-area 650 $m^2/g$ |

## 1.3. Micro-Supercapacitors

Micro-supercapacitors for on-chip power sources have become more important as miniaturized electronic devices are being widely used. For portable electronic devices, there are limits in weight, volume, and also cost since you are carrying them in your hand, bag or pockets. Currently Li-ion batteries are the only solution for portable usage in terms of those constraints. Lack of energy density retains supercapacitors from being used as primary power source for electronic devices ranging from mobile phones to electric cars. However for smaller or miniaturized scale, still there are many applications that wide temperature operating, high power providing, and maintenance-free micro-supercapacitors can contribute to better than other conventional battery technologies. For example, micro-supercapacitors can be adopted in microelectromechanical systems, remote and mobile environmental sensors, implantable biosensors, and wearable electronics.[36] While current batteries need replacement periodically because of short lifecycle, micro-supercapacitors are theoretically maintenance-free when operating voltage is within stable window off the breakdown voltage of electrolyte. In case of the remotely-installed sensors for monitoring, if a sensor module that has energy harvesting or generating function with a micro-supercapacitor, once the sensor starts to operate, it will not require maintenance for a decade. The sensors can monitor temperature, pressure, sound, etc. and can be utilized in many areas from industrial monitoring to health care monitoring. The network of this kind of sensors is called a wireless sensor network (WSN). The wireless sensor network is to monitor physical or environmental conditions and to pass the data through the network. Its development was motivated for military applications and now such networks are widely used in consumer and industrial applications.

Commercial supercapacitors are being used in numerous applications and complement a primary energy source like a battery or fuel cell, internal combustion engine which are not capable of providing quick bursts of power repeatedly. However, in micro-scale where the energy and power that micro-supercapacitor can provide is sufficient, it can be used as a primary energy source to power the device. Currently as a micro-scale energy storage, electrolytic capacitors cannot provide sufficient energy density and Li-ion cannot meet the requirement of burst power delivery for many applications such as wireless sensors, biomedical implants, active radiofrequency identification (RFID) tags and embedded micro-sensors. Since micro-supercapacitors have the advantage of wider operating temperature and long cycle life, the need for micro-supercapacitors will be growing rapidly for years to come.

### 1.3.1. Micro-supercapacitors Design

Micro-supercapacitors consist of electrode materials, electrolyte containing ions to store electrical energy by double layer mechanism, current collector, and separator in some cases. These components are identical to any common ‘bulky’ supercapacitors. The electrical performance of micro-supercapacitors is dependent not only on intrinsic properties of these components but also on the design of micro-supercapacitors.[36]

The early generation of micro-supercapacitors had planar 2D structure with thin film electrodes and solid electrolyte stacked together which is similar construction to conventional supercapacitors. This simple stacked structure gives a good ease in terms of production however the stack design also make it difficult to increase the energy density by using thicker electrodes, because thicker electrodes have ion and electron transport

limited, which deteriorate power delivery of micro-supercapacitors. Another approach to construct a micro-supercapacitor is microfabricated interdigitated electrodes, which utilizes mature microfabrication techniques from the semiconductor industry. [37]

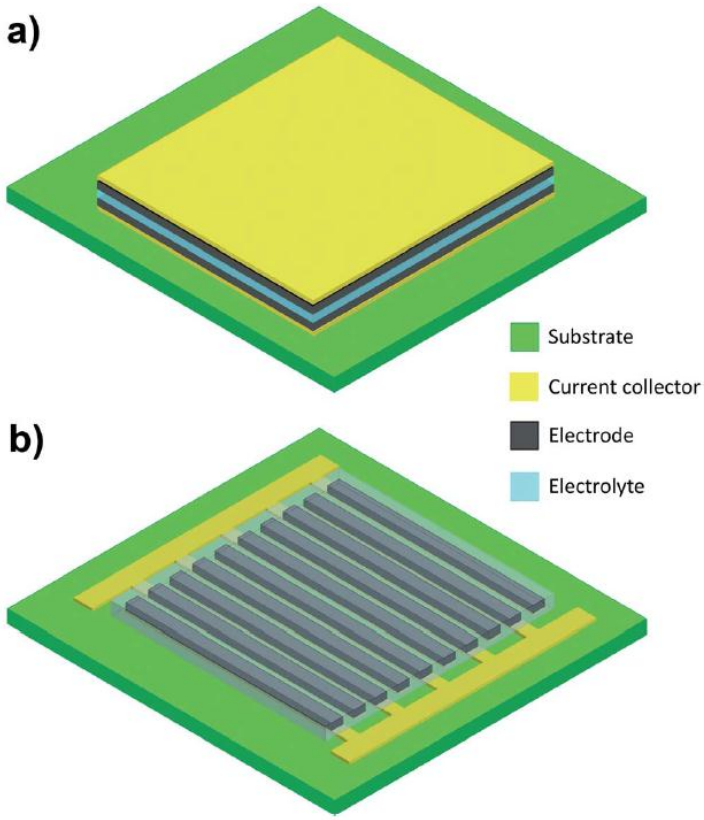


Figure 1.6: Schematic diagrams of on-chip micro-supercapacitors with (a) conventional 2D stacked structure and (b) in-plane interdigital electrode design.[36]

### 1.3.2. Fabrication and Electrode Materials

There are numerous methods for fabrication of film-structured electrode materials. Physical vapor deposition (PVD), chemical vapor deposition (CVD), electrochemical deposition, electrophoretic deposition, inkjet printing, layer-by-layer depositions are deposition techniques that have been widely used for diverse electrode materials. Fabrication techniques are strongly dependent on inherent feature of the electrode or electrolyte materials. If you have active materials to glue on substrates, you need to consider deposition methods utilizing electrostatic force or a small amount of binder to hold the material together on substrates. If you are to grow carbon materials such as carbon nanotubes (CNTs), graphene, etc., CVD might be your first consideration because you have a lot more freedom to design synthesis process for depositing the electrode materials of your choice.

One of the first generation micro-supercapacitors using Ruthenium oxide electrodes was reported in 2001. Direct current reactive sputtering was used for deposition of Ruthenium oxide thin film electrode at 400°C. LiPON electrolyte film was deposited by reactive sputtering on top of bottom Ruthenium oxide electrode at room temperature. The resulting stacked films showed typical double layer capacitor's characteristics and rather a bit higher IR drop and faster capacity decrease, which was explained by large ion size and its slow mobility.[38]

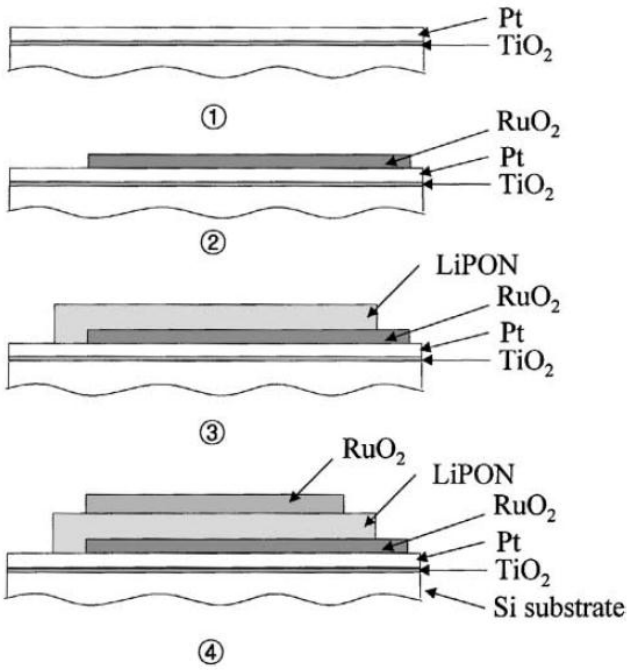


Figure 1.7: Fabrication of a micro-supercapacitor using Ruthenium Oxide films.[38]

Since the stacked Ruthenium oxide thin film supercapacitor was reported, many different fabrication methods have been tried to synthesize various electrode materials for different architectures in order to improve the energy density and power delivery of micro-supercapacitors.

In the early days of micro-supercapacitors, mostly oxide materials and conducting polymers were used via sputtering, atomic layer deposition, and electrodeposition. Then carbon-based stacked micro-supercapacitor was reported in 2006 by H.J. In using unique 'origami' method (Fig 1.9). The carbon film electrode was made with 99 wt% of Super P carbon black and 1 wt% of polyvinylidene fluoride binder in N-Methyl-2-pyrrolidone.[39] Another stack micro-supercapacitor using carbon microbeads with a PVDF polymer binder, was reported by C.C. Ho et al.[40] Both carbon-based micro-supercapacitors

showed double layer capacitive behavior and low specific capacitance due to the low surface area carbon materials. However it helped to provide proof of concept for carbon-based stacked micro-supercapacitors.

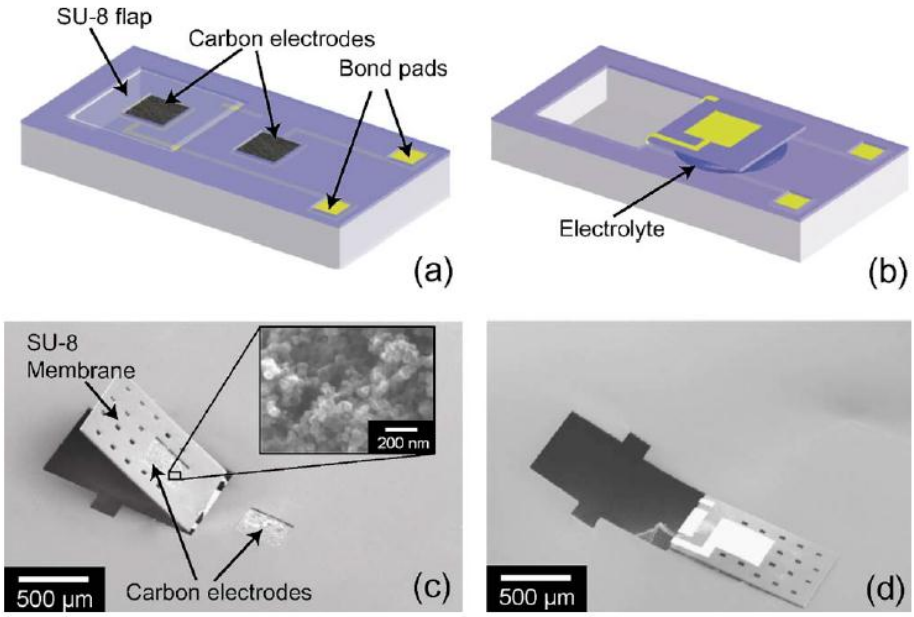


Figure 1.8: Schematic drawings of the origami supercapacitor before (a) and after folding (b). SEM images of the supercapacitor with carbon electrodes (C) and (D).[39]

Chemical vapor deposition (CVD) is one of the most frequently used deposition method. Combining sources gases at elevated temperature leads to form active electrode materials on substrates, ranging from carbon nanotubes to grapheme. CVD can be used at as low as room temperature depending on materials, hence wide range of substrate materials can be chosen.

Vertically aligned carbon nanotubes (VA-CNTs) electrodes grown by CVD was reported and showed good capacitive performance with high charging rate.[41] Not only CNTs, Graphene could be grown by CVD as well. CVD-grown pristine graphene film electrodes were stacked as a cell and this in-plane graphene micro-supercapacitor showed a specific capacitance of 80 $\mu F/cm^2$ (Fig 1.10).[42]

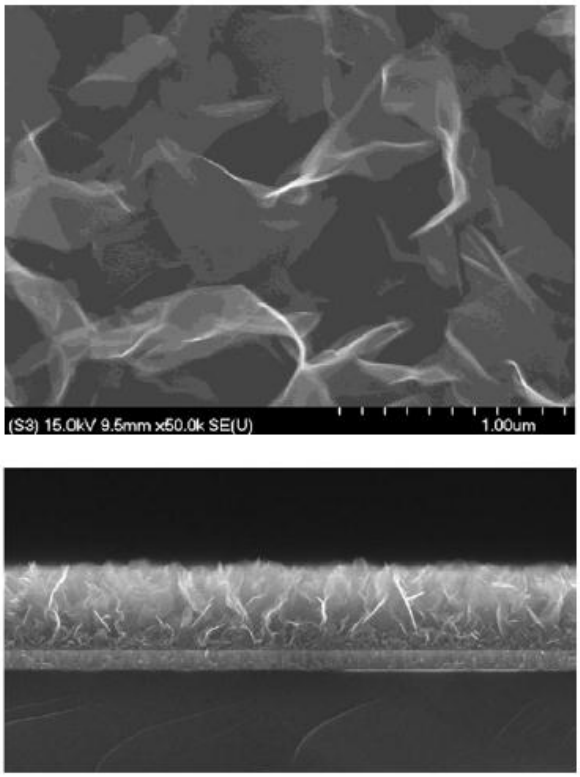


Figure 1.9: Plain and cross-section views of vertical oriented graphene grown with hydrogen and acetylene gas on a silicon substrate.[43]

As shown in Figure 1.9, J. Miller et al. reported 'vertically oriented graphene nanosheets' grown directly on metal current collector which showed ultra-high power

performance and minimized ionic and electronic resistance. Thanks to graphene nanosheets having edge planes exposed to electrolyte, it showed RC time-constants of less than 200 μs which is great improvement compared to 1s of typical EDLCs.[43, 44]

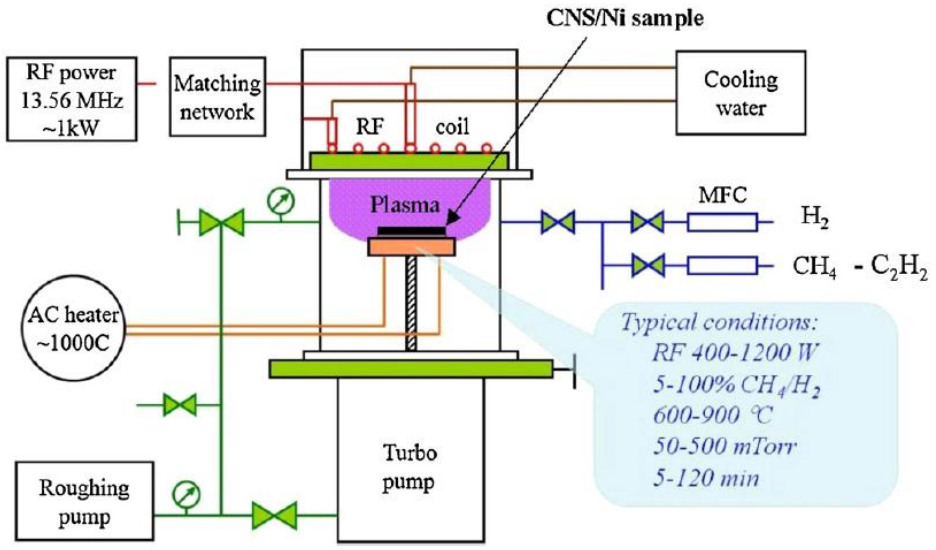


Figure 1.10: Schematic of plasma-enhanced chemical vapor deposition apparatus used to synthesize the vertically oriented graphene nanosheet EDLC electrodes.[43]

Although the open pore structure of CVD-grown carbon nanotubes and graphene-based electrodes delivered very high power, these micro-supercapacitors were not able to provide high energy density due to the limitation on the amount of loaded or grown active electrode materials per unit area or volume.[36]

Layer-by-Layer (LBL) deposition has been used to prepare thin film electrodes, mostly for carbon nanotube electrodes. LBL is one of the solutions for binder-free, carbon-based nanostructured electrodes and provides higher density electrodes which

results in higher energy density. Another advantage of LBL technique is that materials of your interests can be mixed together in a stable electrostatic assembly. In 2011, S.W. Lee et al. reported binder-free multiwall carbon nanotube film electrodes for micro-batteries and micro-supercapacitors, which showed relatively higher capacitance than VA-CNT based micro-supercapacitors mainly because of higher density electrode prepared by LBL.[45]

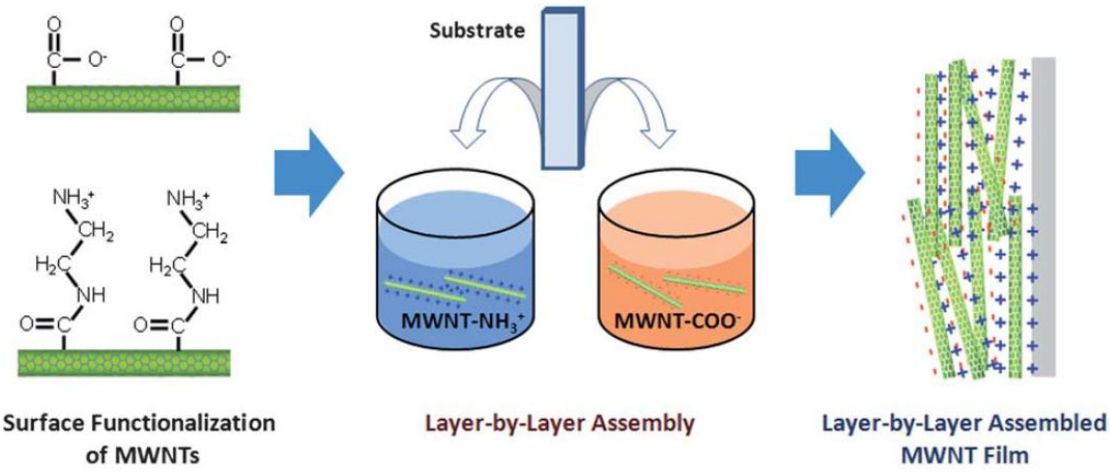


Figure 1.11: Schematic of layer-by-layer assembly of functionalized MWNTs.[45]

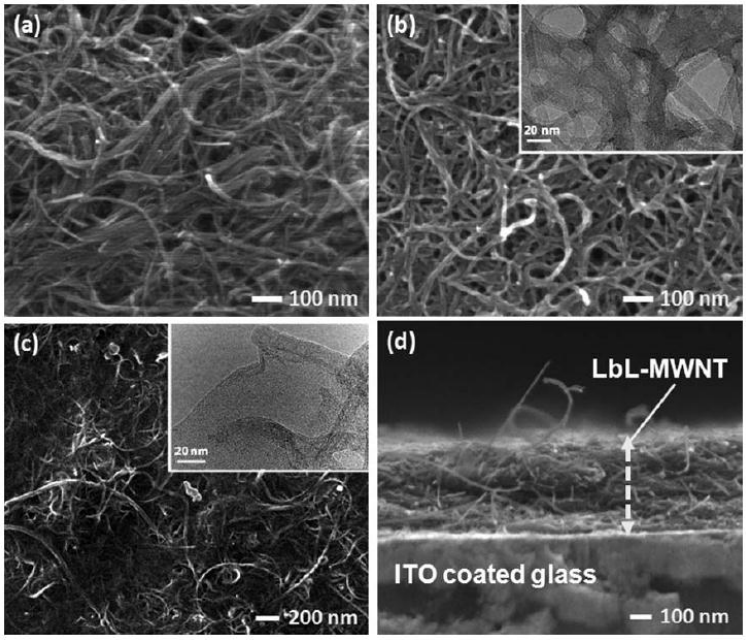


Figure 1.12: SEM images of LBL electrode: (a) 20 wt% PVDF - 80 wt% pristine MWNT, (b) LBL-MWNT, (c) LBL-MWNT/graphene, and (d) Cross-section of LBL-MWNT.[45]

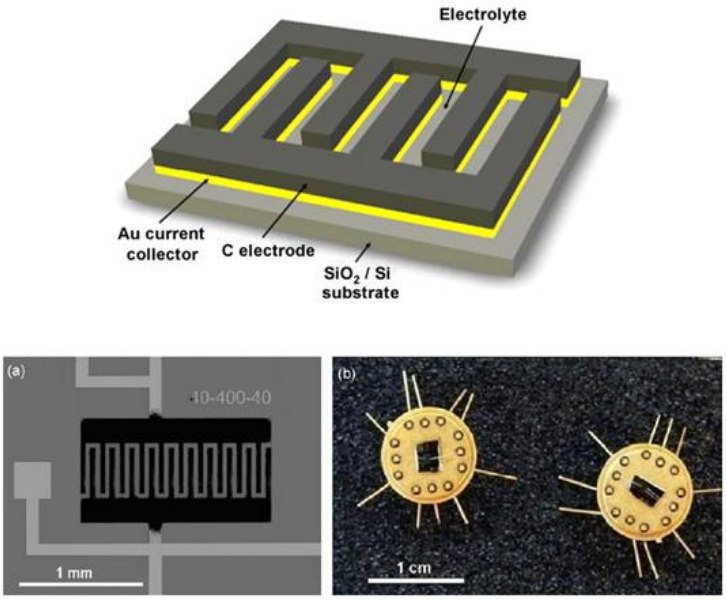


Figure 1.13: Schematic drawing and image of inkjet-printed micro-supercapacitors.

Another way of producing carbon-electrode without binder is Ink-jet printing. David Pech et al. fabricated carbon-based micro-supercapacitors with inkjet printing. Patterned current collector was prepared by typical semiconductor process; photolithography and etch and carbon ink was printed on top of the pre-patterned current collector by inkjet printing as shown in Figure 1.13.[46]

By the same group, a micro-supercapacitor produced by electrophoretic deposition of nanostructured carbon onions was reported with a volumetric power density of 1 $kWcm^{-3}$. Since carbon onions have a smaller specific surface area of ~500 $m^2/g$, compared to activated carbon's 1500 – 2200 $m^2/g$, naturally it has not as high energy density as activated-carbon based micro-supercapacitors. However, the power density of carbon onion based micro-supercapacitor was at high as electrolytic capacitors as shown in the Ragone plot (Fig. 1.16).[47]

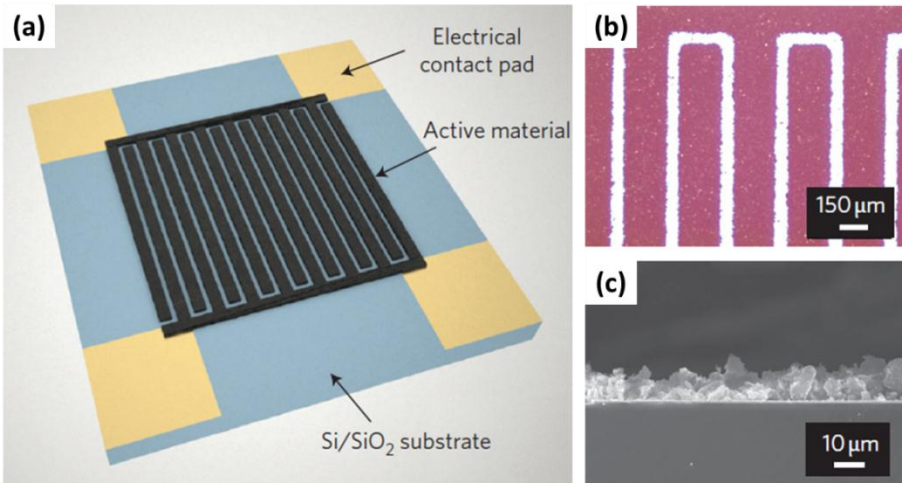


Figure 1.14: Interdigital micro-supercapacitor with OLC electrodes. (a) Schematic of the micro-supercapacitor (25 mm2) made of 16 interdigital finger electrodes, (b) Optical image of the interdigital fingers with 100 µm spacing, (c) SEM cross-sectional image of the carbon onion electrode.[47]

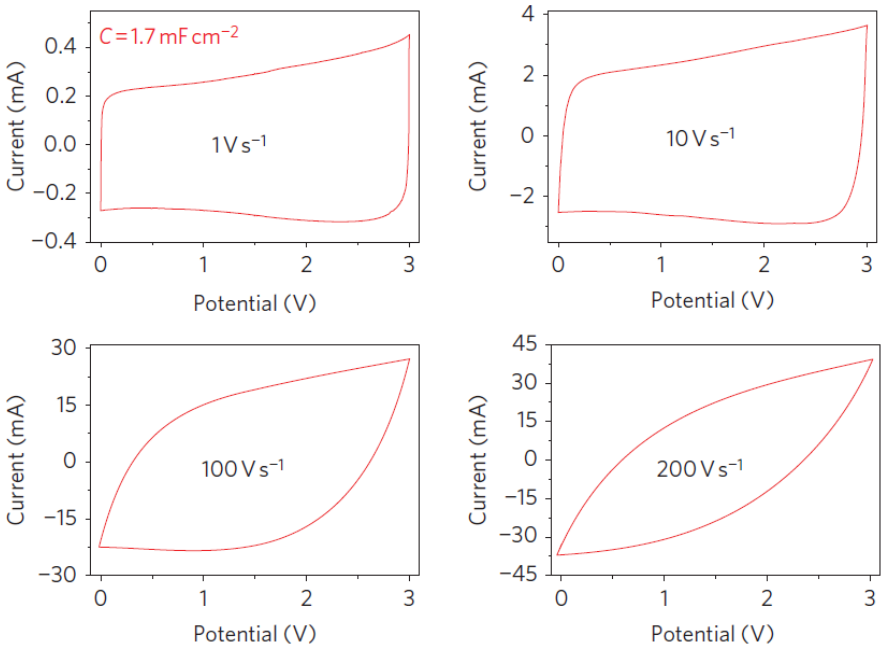


Figure 1.15: CVs with different scan rates in a 1 M $Et_4NBF_4$/anhydrous propylene carbonate on a 16-interdigital micro-supercapacitor with a 7-mm-thick OLC electrode.[47]

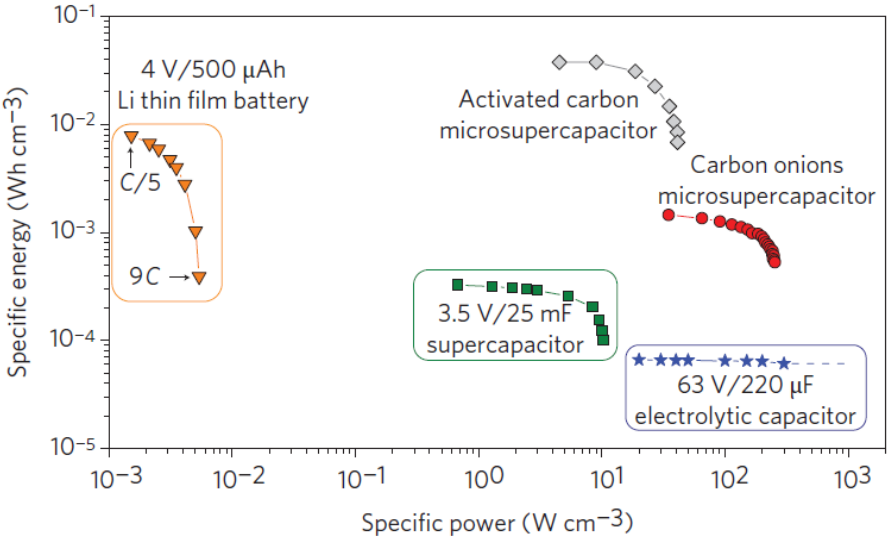


Figure 1.16: Ragone plot of typical electrolytic capacitors, supercapacitors and batteries with the micro-devices.[47]

Electrophoretic and electrochemical deposition techniques have been used to fabricate thin film electrodes of various materials such as carbon nanotubes, graphene, activated carbon, carbon onions, transition metal oxides and conducting polymers.[46-52]

In reality, for development of on-chip micro-supercapacitors, most likely Silicon wafers would be your choice of substrate. Then, PVD and CVD might be only viable solution among other fabrication techniques, because they are mature technologies and are fully compatible with semiconductor processes, most of all, mass-production proven. Building electrodes on substrates with nanostructured carbon particles such as CNT or graphene has lot of potential issues for semiconductor production process. Because semiconductor manufacturing process is prone to particle-related failures. Therefore, synthesizing a smooth, continuous nanoporous carbon films directly on Silicon substrates using semiconductor compatible processes are vital to development of micro-supercapacitors.

## 1.4. Carbide-Derived Carbon (CDC)

CDC used to have multiple different names over the years. Once it was called “mineral carbons”, then “nanoporous carbons (NPC). Carbide-Derived Carbons (CDC) encompass a large group of structurally varying carbon materials ranging from disordered to highly ordered carbon allotropes. The carbon structure resulted from removal of the metal atoms from various metal carbides rely on treatment method (halogenations, hydrothermal method, vacuum decomposition, and so on), applied temperature and choice of carbide precursor.[53]

The excellent absorptivity of carbide-derived carbon was recognized already in 1960's.[54] But the unique nanoporous structure of CDC with the narrow pore size distribution and pore size tunability was confirmed lately[55, 56] which has been boosting the research on CDC materials and its application as electrode materials over years.

CDC can be synthesized via several physical and chemical processes. Halogenation (or chlorination) is one of the well-known methods that have been used over several decades, transforming carbide precursors to carbon materials. Many different methods can be used to produce CDC; halogenation, hydrothermal process, thermal decomposition in vacuum, etc.

### 1.4.1. CDC Synthesis - Halogenation

There are several methods that can be used to produce CDC. The common ground in those different methods is that carbon is formed by extraction of metal atoms. By this way, carbon layer grows from the surface of carbide toward inside, while the initial shape and volume of the carbide precursor is largely preserved. Nanoporous CDC is produced by extracting metals from carbide precursors at high temperature. Halogenation, a gas etching method with halogen gas is a most useful and capable technique to tune pore structure. In general, chlorine has been widely used for CDC synthesis:

$$MC + \frac{x}{2}Cl_2 \rightarrow MCl_x + C \qquad (8)$$

Chlorination of silicon carbide was patented by Otis Hutchins in 1918, which was first report of CDC production in records.[57] Heated silicon carbide was exposed to chlorine gas to form silicon tetrachloride and carbon. This process was altered for $SiCl_4$

mass-production after several decades. CDC was nothing more than a byproduct of $SiCl_4$ synthesis until 1950's.

The carbon formation via selective halogen gas etching is possible for many binary carbide materials. Fluorination of $Al_4C_3$, $B_4C$, $CaC_2$, $Cr_3C_2$, $Fe_3C$, SiC, $ThC_2$, TiC, $UC_2$, WC and HfC were reported.[58-61] Fluorination of TiC with pure fluorine gas was reported by N. Batisse et al. in 2011. Their study showed low yield of nanoporous carbon with average pore size of 0.59 nm at lower temperature range from 130 to 300 °C.[60]

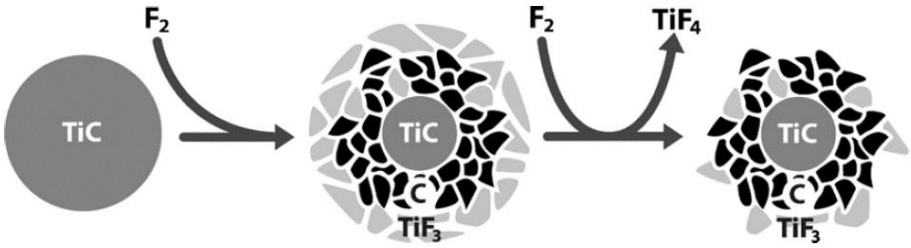


Figure 1.17: Fluorination mechanism of titanium carbide.[60]

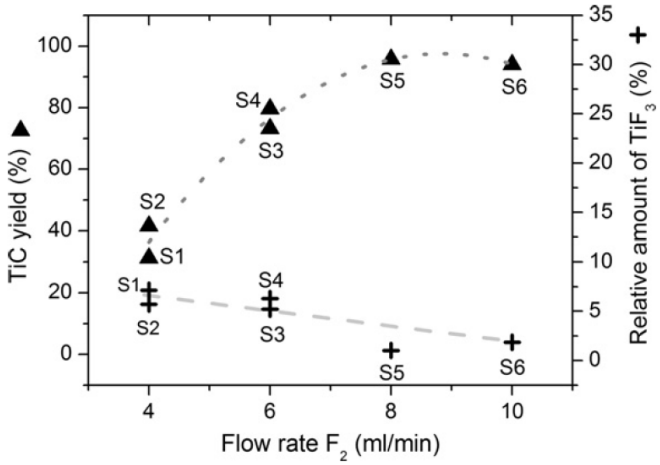


Figure 1.18: Evolution of TiC degradation and $TiF_3$ formation (relative amount of $TiF_3$ residual versus theoretical) as a function of the different fluorination flows.[60]

Many different kinds and forms of carbide precursors have been tested for halogenations: single crystals, sintered ceramics, hot-pressed, whiskers, powders and thin films.[17, 62-64] These fundamental studies on CDC formation have greatly improved our understanding of CDC synthesis.

Chlorination is the most stable, controllable and high yield process for CDC synthesis. A number of thermodynamic analysis has been performed for chlorination of SiC, $Ti_3AlC_2$, $Ti_2AlC$, TiC and ZrC.[53, 65-68] Thermodynamic simulation cannot determine the kinetics of CDC formation but can provide important information; what reactions will be dominant as a function of reaction temperature and the amount of gas/solid materials. With the help of thermodynamic calculations, optimal process window for CDC formation can be selected with the desired halogen gas.

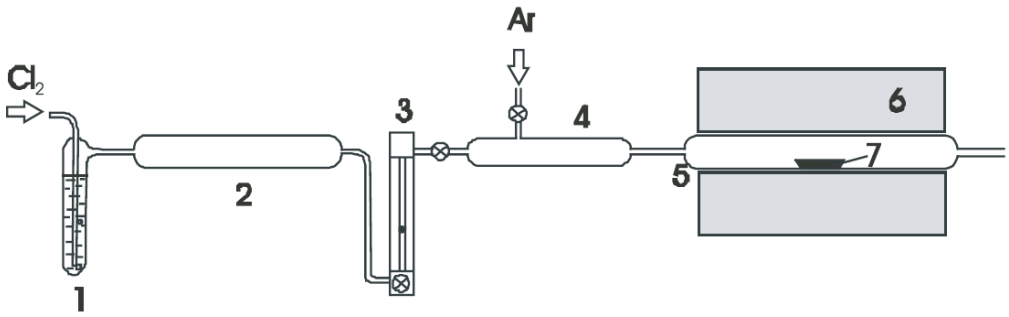


Figure 1.19: Experimental setup for chlorination (1) sulfuric acid, (2) desiccant, (3) flowmeter, (4) mixing column, (5) fused silica reaction tube, (6) tube furnace and (7) carbide precursor material.[69]

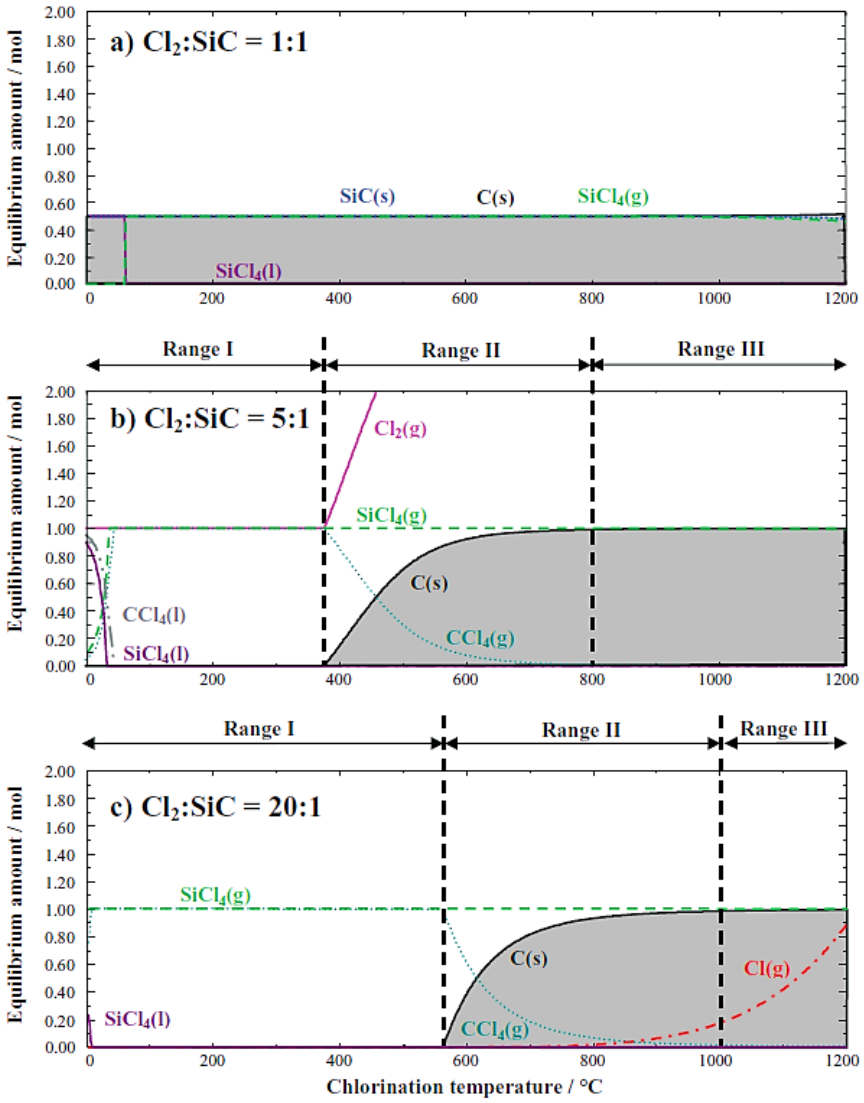


Figure 1.20: Thermodynamic calculations for the chlorination of SiC with different carbide to chlorine ratios. Chlorine to carbide ratio of 1:1 (a), 5:1 (b), and 20:1 (c).[53]

### 1.4.2. CDC Synthesis - Vacuum Decomposition

Thermal decomposition of carbide in vacuum or inert gas atmosphere is another way of CDC synthesis. CDC is formed by result of incongruent melting of carbide and evaporation of the carbide-forming elements, as the melting point of carbon exceeds that

of most metals.[53, 70] Most studies have been focused on vacuum decomposition of silicon carbide thanks to the abundant supply and probably its publicity in the electronics. In late 1940s, first reported study on decomposition of SiC found that dense graphitic carbon formed after heating to 2000 °C.[71] Early observations on vacuum decomposition of silicon carbide showed formation of turbostratic carbon and graphitic carbon with respect to the underlying SiC lattice, where the carbon layers are ordered either parallel or perpendicular to the SiC c-axis.

Badami et al. reported that the number of carbon atoms in a layer of SiC is smaller than what is required to form a continuous graphite layer, which means a single graphene layer formation requires ~3 SiC bilayers.[72] Structural rearrangement is very important aspect of vacuum decomposition and need higher temperature for formation of carbon with more graphitic or ordered structure. It was reported that 800°C is the lower limit of carbon formation by vacuum decomposition.[73]

In 1997, Kusunoki et al. reported carbon nanotube formation by vacuum decomposition of silicon carbide.[74] This CNT formation is very unique because there is no metal catalyst involved during CNT nucleation and growth.[75-79] Kusunoki found that lowest temperature for CNT film formation is 1250-1300°C.[76] A model for CNT formation proposed by Kusunoki suggested that residual oxygen drives CNT formation.[80] Later by Z. G. Cambaz et al. it was also shown that CNT can form on both Si-face and C-face by adding $CO_2$ gas during vacuum anneal.[81] This give us more idea about gas transport, which plays very important role in CNT forest formation and growth. The presence of CO or $CO_2$, helped CNT to grow because they are additional source of carbon for CNT to grow. Also Cambaz reported that by surface modification both CNT and graphite can be formed on both Si- and C-face of SiC crystal.[81]

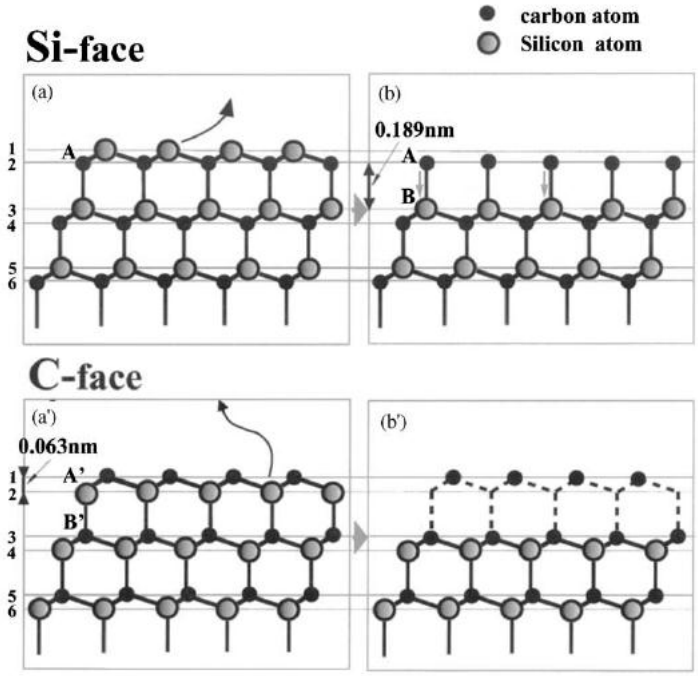


Figure 1.21: Decomposition mechanisms - selective evaporation of Si atoms.[79]

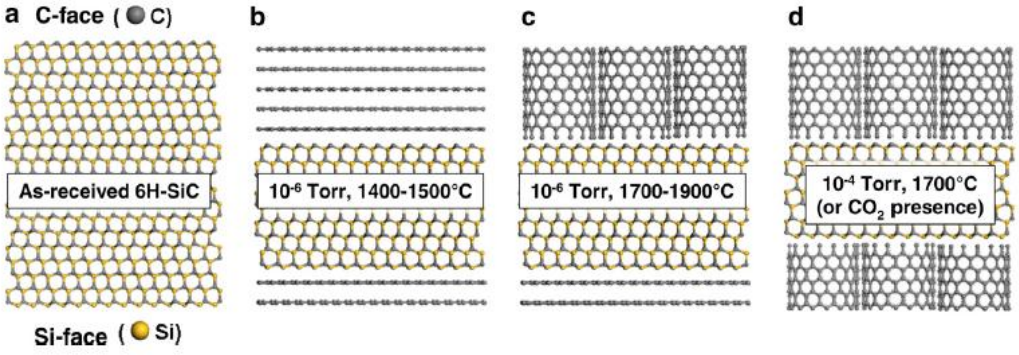


Figure 1.22: Models of the atomic structure of (a) SiC crystal, (b) graphite growing on both faces at moderate temperatures, and (c) CNTs growing on the C-face at high temperatures. (d) Oxygen-assisted CNT formation on both faces of SiC.[81]

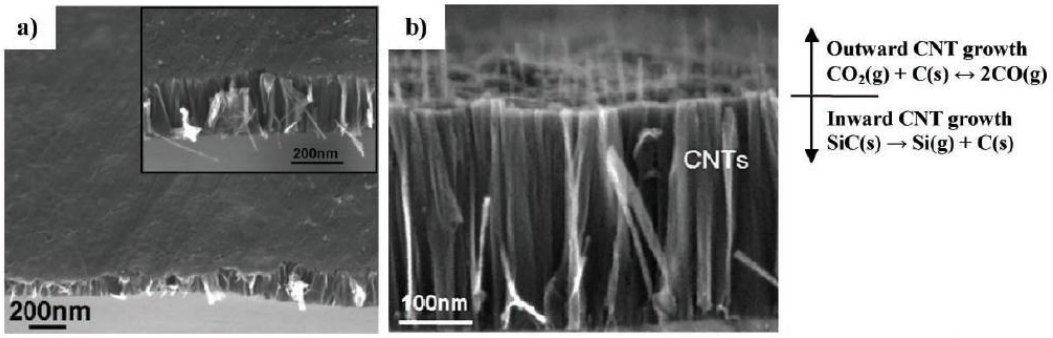


Figure 1.23: SEM images of different carbon nanostructures obtained from vacuum decomposition of 6H-SiC for the C-face in high vacuum (a) Si-face in low vacuum (b).[53]

### 1.4.3. Microstructure and Porosity

High porosity and high specific surface area is characteristic of CDC materials obtained by halogenation.[82] The bulk porosity of CDC is mostly determined by the structure of carbide precursor. This is schematically illustrated in Figure 1.24 for $Ti_3SiC_2$ and 3C-SiC. It shows that differences in the distribution of carbon atoms in the carbide lattice lead to a major change in the resulting CDC structure.[53]

While the porosity of CDC stays mostly unchanged over a wide range of halogenation temperatures, the pore size distribution (PSD) is a function of the temperature. As first shown by Boehm in 1975 on CDC synthesized from TaC and SiC[83], and later for most carbide precursors,[82] the resulting carbons have Type I isotherms, which is evidence of microporosity with pore sizes less than 2 nm and relatively high surface areas up to 2000 m2/g.[68, 69, 84] The pore size of CDC can be tailored by selection of carbide precursors with different spatial distributions of carbon atoms in the initial carbide lattice, changing the microstructural ordering in the CDC by varying the synthesis temperature, and post-treatment in a variety of oxidizing atmospheres

(activation).[55, 85] Therefore, both microporous and mesoporous carbons with different pore shapes can be produced.[14]

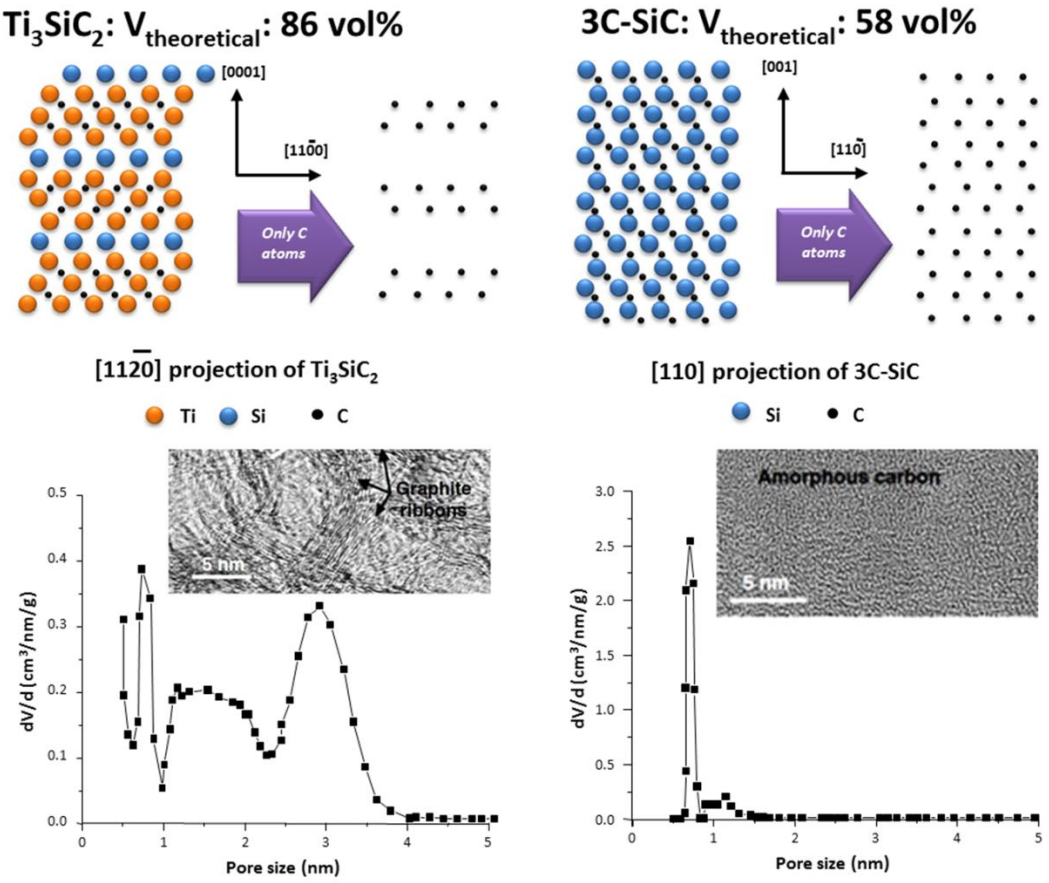


Figure 1.24: Schematic of the atomic structure of $Ti_3SiC_2$ and 3C-SiC and the corresponding CDC structures after chlorination. The ternary carbide shows a broader pore size distribution than the binary carbide. Also, for the same chlorination temperature (1200 °C) the resulting carbon structure can be very different – while SiC-CDC still consists of predominantly amorphous carbon, $Ti_3SiC_2$-CDC shows significant graphitization at the same temperature.[53, 62, 82]

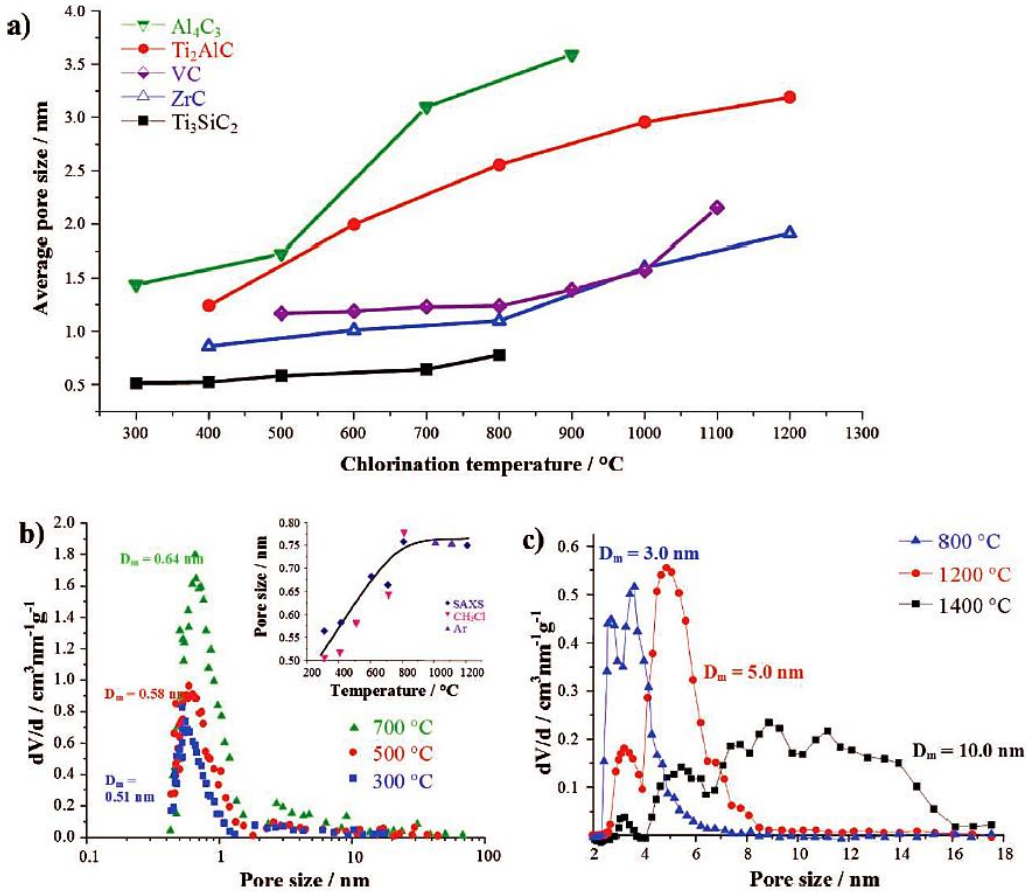


Figure 1.25: Average pore sizes for various binary and ternary carbides.[55, 66, 68, 86, 87]

Mesoporous CDC produced from polymer-derived materials, and ordered mesoporous carbon produced by template method showed a type IV adsorption isotherm with a characteristic hysteresis loop due to condensation in the mesopores.[88, 89]

Generally, pore size and PSD of CDC materials are templated by the carbide precursor structure at low temperatures. At higher temperatures, pore size is increased due to self-organization and higher carbon mobility.[90] For many carbide materials, it was found a direct correlation between the halogenation temperature and the resulting pore size. (Figure 1.25)

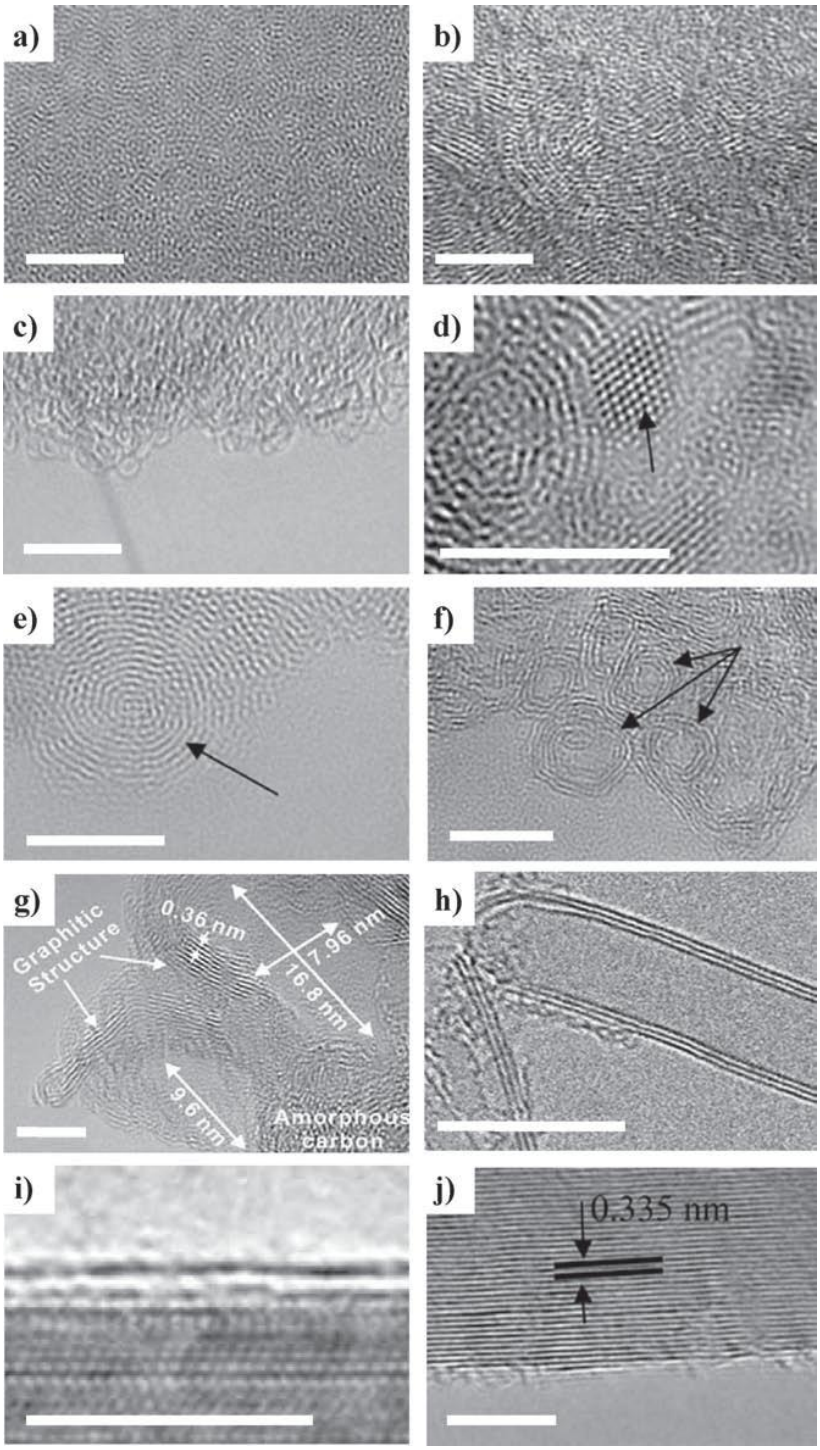


Figure 1.26: Transmission electron microscopy images of various CDC structures as obtained from chlorination of carbide (a-g, j) and vacuum decomposition of SiC (h-i).[53]

The structure of CDC also depends on precursor material and halogenation temperatures as pore size, pore size distribution and specific surface area of CDC do. Figure 1.27 shows the structural change of CDC made by chlorination of TiC at different temperatures as an example. Although largely amorphous structure is dominant at lower temperature produced CDCs, there are many other carbon nanostructures observed; such as carbon onions, nanodiamond, nanotubes, barrel-like structures and even fullerene-like structures.[53]

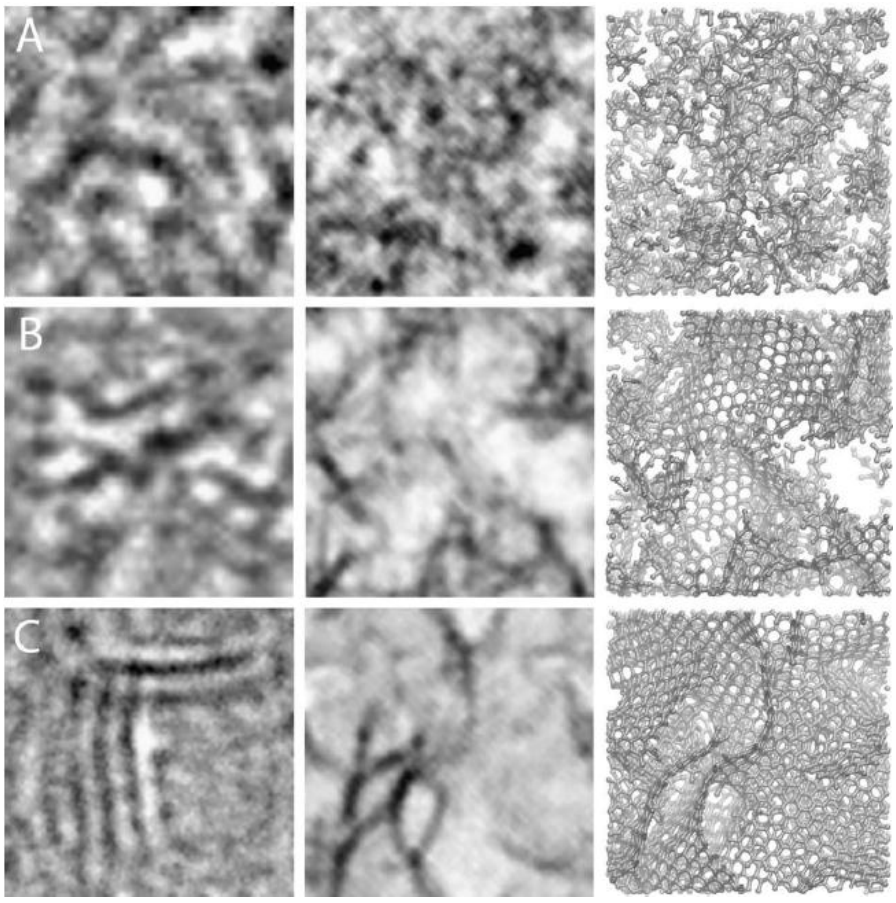


Figure 1.27: Comparison of experimental HRTEM images (left column), simulated HRTEM images (center column) and snapshots of the model structures (right column).[91]

### 1.4.4. CDC Electrode for EDLCs

As supercapacitor electrodes, various kinds of carbide precursors have been studied such as TiC[17, 56, 84, 92-97], SiC[56, 95, 98], $Ti_2AlC$[56, 92], $B_4C$[63, 92], $Al_4C_3$[56, 99], $Mo_2C$[56, 100], and VC[101] over years. CDC from various carbide precursors differ significantly in total pore volume, pore size distribution and carbon nanostructure which greatly affect on capacitance of the various CDC.[95] The CDC from $Al_4C_3$ showed higher gravimetric capacitance, 110 F/g in tetraethylammonium tetrafluoroborate ($NEt_4BF_4$) in acetonitrile electrolyte[99] and 135 F/g of SiC-CDC in the same organic electrolyte.[98] The capacitance of TiC-CDC electrodes in $NEt_4BF_4$ in acetonitrile was 140 F/g,[102] which is better than 75 F/g $B_4C$-CDC electrodes.[56] Also capacitance for mesoporous CDC from $Mo_2C$ in 1M $(C_2H_5)3CH_3NBF_4$ electrolyte in acetonitrile was 142 F/g,[94] while VC-CDC showed 133 F/g in the same electrolyte.[101]

Different synthesis temperatures and different precursors are the most critical factors affecting capacitance of CDC used for electrodes in supercapacitors. It's been reported that generally the gravimetric/volumetric capacitance increases with larger pore size as the specific surface area and pore size increase with higher chlorination temperatures.[15] However Chmiola et al. observed that there is an abnormal increase in capacitance as pore size decreases less than 1 nm and later more detailed study on the correlation between pore size and capacitance corroborated this capacitance increase when the pore size approaches that of the desolvated ion.[102, 103] Therefore, having a high total surface area, pore sizes tuned to the electrolyte ion size and ensuring that the pore volume is accessible to ions without facing transportation limitations is the key for achieving high capacitance.

Usually, in order to prepare CDC electrodes, a binder such as polytetraflouroethylene (PTFE) or polyvinylidene fluoride (PVDF) is mixed with CDC powder and the mixture is formed into a several hundred micrometer thick film.[104, 105] In general, CDC based supercapacitors (143 F/g in organic electrolytes, 250 F/g in aqueous electrolytes) show higher capacitance than carbon nanotube-based ones (20 – 100 F/g).[92]

## 2. Objectives

Contrary to the fact that nanoporous carbon materials are mostly used for conventional 'bulky' supercapacitors, not much work has been done for thin film deposition of nanostructured carbons mainly due to difficulties of making continuous smooth films out of nanoporous carbon materials.

The objective of this work is to synthesize smooth, continuous nanostructured carbon films on silicon substrates, to improve the fundamental understanding of CDC films and to develop CDC film-based on-chip micro-supercapacitors. My work focuses on synthesizing nanoporous CDC films and developing micro-supercapacitor based on CDC films by using microfabrication techniques.

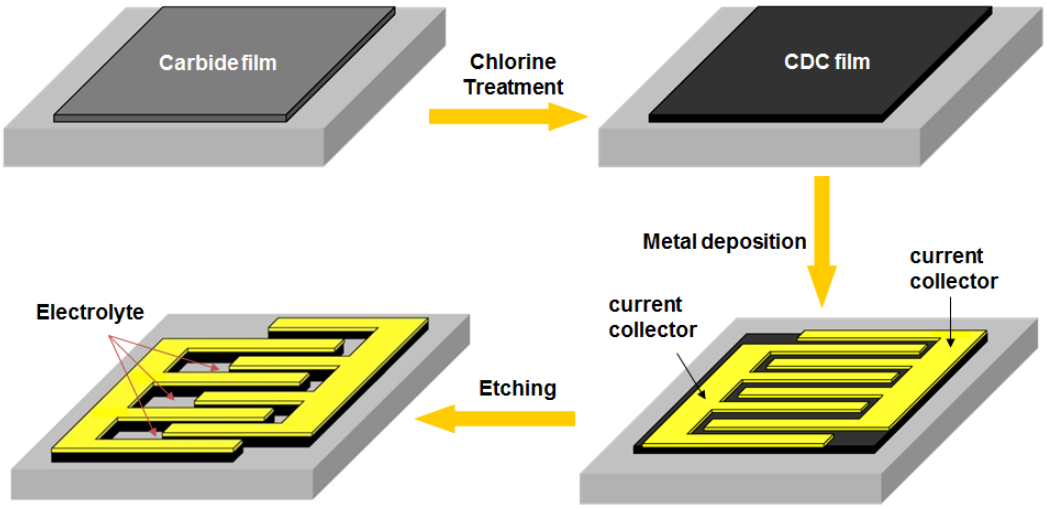


Figure 2.1: Schematic of the CDC synthesis and on-chip micro-supercapacitor fabrication.[17, 106]

# 3. Experimental

## 3.1. Materials

### 3.1.1. CDC Precursor Carbides

To produce CDC films, carbide crystal wafers and carbide films grown on Si wafers were used as precursors.

#### 3.1.1.1. SiC wafers

SiC crystal wafers (polytype 4H, diameter 76.2 mm, thickness 350 μm, Si-face standard polished EPI-ready, C-face optical polished, MPD < 30/cm$^2$) were purchased from SiCrystal and cut to size (10 mm x 10 mm x 0.35 mm) using a diamond cutter.

#### 3.1.1.2. Carbides Films grown on substrates

SiC films were deposited on Silicon wafers by sputtering in Ar atmosphere using SiC target in LPN, France. 500 W was set to run sputtering with an overall pressure of 1 Pa and substrates were not heated during SiC deposition.

Figure 3.1: Magnetron sputtering chamber (Rowan University, New Jersey)

TiC films were deposited by magnetron sputtering at Rowan University, New Jersey. For reactive growth of TiC films, a Ti target and Acetylene ($C_2H_2$) gas were used and the Ti target was run at 200 W at an overall pressure of 30 mTorr. The gases were mixed in a manifold with an Argon flow rate of 40 sccm and a $C_2H_2$ flow rate of 2.5 sccm. For non-reactive deposition, Ti and C targets were used with an Ar flow rate of 40 sccm. The substrates were heated to 700 ~ 900 °C to produce textured TiC in the (111) orientation. The reactive deposition rate was approximately 25 nm/min on Si wafer (resistivity 1-100 Ohm cm with 200 nm wet thermal oxide), glassy carbon (SIGRADUR, G plate, one side diamond polished, Ra < 10 nm), Sapphire ((0001) oriented, epi-polished) and highly ordered pyrolytic graphite (HOPG, monochromator grade).

### 3.1.2. CDC Synthesis

CDC films were synthesized by two different techniques; chlorine gas etching (Chlorination) and vacuum decomposition at elevated temperatures, depending on what carbide precursors were used. SiC-CDC films were produced by vacuum decomposition of SiC wafers at the temperature higher than 1500 °C. High temperature chlorine gas etching of SiC, TiC films grown on substrates resulted in synthesis of uniform, SiC-CDC, TiC-CDC films with good adhesion to the substrates.

#### 3.1.2.1. Chlorine Gas Etching

To synthesize CDC films, Carbide film precursors were placed in a quartz tube and treated with chlorine gas inside a tube furnace at temperatures ranging from 250 °C to

600 °C in order to extract non-carbon elements from carbides. The experimental setup used is shown in Figure 3.2.


Figure 3.2: Experimental set up for chlorination.

Before heating, to remove the air from the quartz tube, Ar gas (Airgas, UHP grade) purging should be performed with a flow rate higher than 30 $cm^3$/min for at least for 6 h before heating over 200 °C to prevent carbide films from oxidation during chlorination. To avoid any backflow of air into the quartz tube, a bubbler with sulfuric acid was attached to the quartz tube. When Ar purging is finished, the furnace was heated to the desired temperature under Ar atmosphere. Chlorine gas was introduced into the quartz tube at a flow rate of 10 - 15 $cm^3$/min for 10 to 30 minutes, when the desired temperature (250 °C ~ 600 °C) was reached. After the chlorination, samples were cooled down to room temperature under Ar atmosphere.

3.1.2.2. Vacuum Decomposition

Vacuum decomposition was conducted on SiC crystal wafers by using a vacuum furnace (up to $10^{-6}$ Torr, Solar Atmosphere). Carbide wafers were placed in the flat bottom of a graphite crucible and the graphite crucible was placed at the center of the vacuum furnace. Once the vacuum had reached to high vacuum level (~$10^{-6}$ Torr), the furnace started heating to high temperature up to 2000 °C. The ramping rate was 10 °C/min.


Figure 3.3: Vacuum furnace with a chamber 7.5" in diameter and 14.5" in depth (donated by Solar Atmosphere). Hot zone constructed with energy efficient graphite insulation allows a maximum temperature of 2200 °C.

3.1.3. Electrolytes

Water, acetonitrile and propylene carbonate (anhydrous 99.8%, Fisher Scientific) were used as solvents. Water was deionized using Millipore Elix 5 system (> 18 MΩ-cm). Sulfuric acid (98%, Sigma Aldrich) and tetraethylammonium tetrafluoroborate ($NEt_4BF_4$,

Acros Organics) were used as salts dissolved in water, acetonitrile (AC), and propylene carbonate (PC), respectively. Organic electrolyte preparation was conducted inside the glovebox in dry Ar atmosphere.

## 3.2. Characterization

### 3.2.1. Structural Characterization

X-ray diffraction (XRD) was performed using Siemens D500 and Rigaku SmartLab diffractometers with $Cu_{K\alpha}$ radiation ($\lambda$ = 1.54Å). XRD patterns were collected using step scans, with a step size of 0.01°(2θ) and a count time of 2 seconds per step.

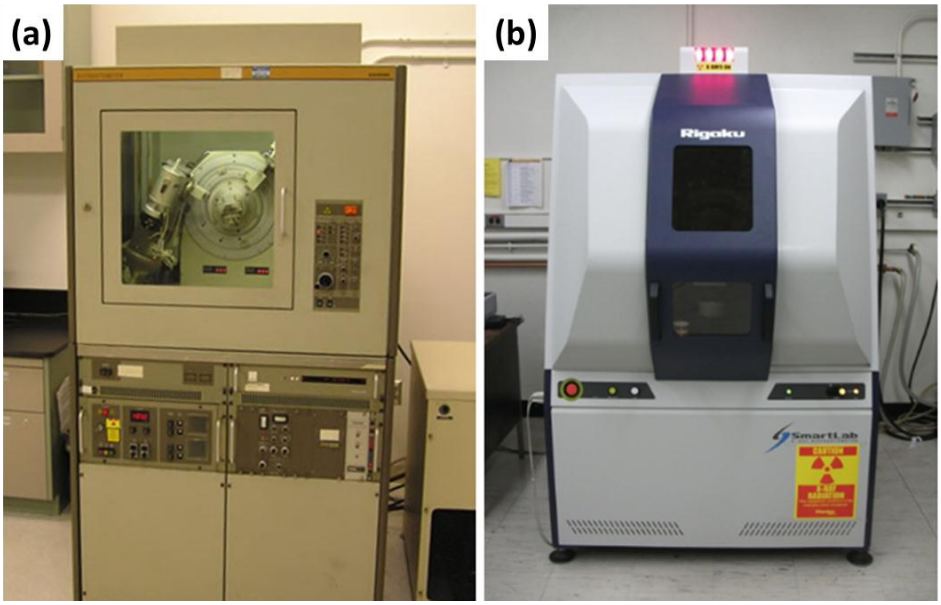


Figure 3.4: X-ray diffractometer: (a) Siemens D500 and (b) Rigaku SmartLab.

Raman spectroscopy was carried using a RM1000 system (Renishaw) with Ar ion laser (514.5nm) at 20x magnification (~2μm spot size) and 5~50% power. Raman spectra were analyzed by using two bands: the D band and the G band of graphite fitted to Lorentzian functions and normalized to the intensity of the G-band peak at 1582 $cm^{-1}$.


Figure 3.5: Renishaw Laser Raman Microscope RM1000.

Scanning electron microscopy (SEM) was conducted using Zeiss Supra 50VP with EDS (Oxford). SEM images were taken before and after chlorination to observe the morphological change, micro-cracking, delamination and to measure the thickness. The resolution of SEM was not enough to visualize the micro-porosity of the CDC films, but allowed visualization of cracks, roughness, and micro-grains as well as surface morphology of carbide or CDC films.

Transmission electron microscopy (TEM) samples were prepared two ways: 1) dispersing the material in ethanol and placing the solution over a copper grid with a lacey carbon film, 2) preparing a sample (25 μm x 5 μm x ~100 nm) using focused ion beam (FIB). TEM study was performed using the JEOL 2010F microscope at 200 kV.

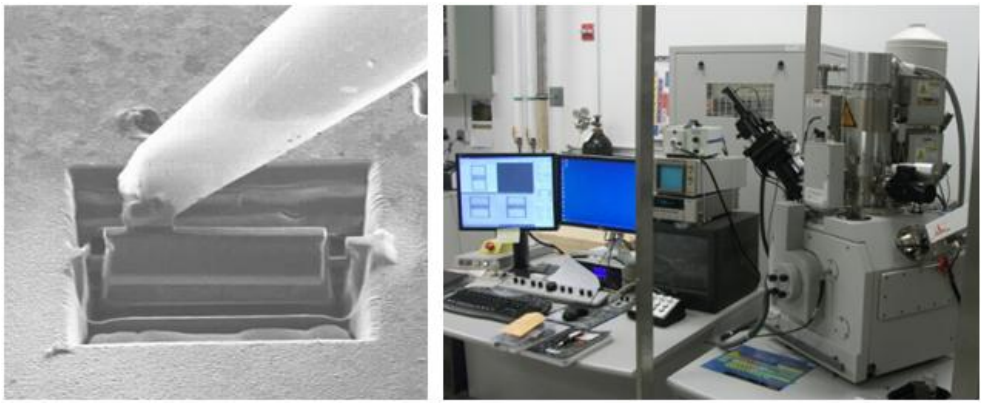

Figure 3.6: A TEM sample prepared by Focused Ion Beam (FIB).

### 3.2.2. Electrochemical Characterization Techniques

A potentiostat/galvanostat (VMP3, 16-channel, Bio-Logic) with a low current option and impedance boards was used to perform electrochemical tests on cells. Each channel has a potential range from -10 V to +10 V, input impedance of $10^{14}$ Ω, and maximum 400 mA current rating, with 76 fA maximum advertised current resolution for the low current option in 1 nA range. The impedance boards have a maximum frequency range of 10 μHz – 1 MHz.

Three techniques were used for electrochemical characterization: cyclic voltammetry (CV), galvanostatic cycling (GC), and electrochemical impedance spectroscopy (EIS). The software, EC-Lab was used to control the potentiostat and record the data.

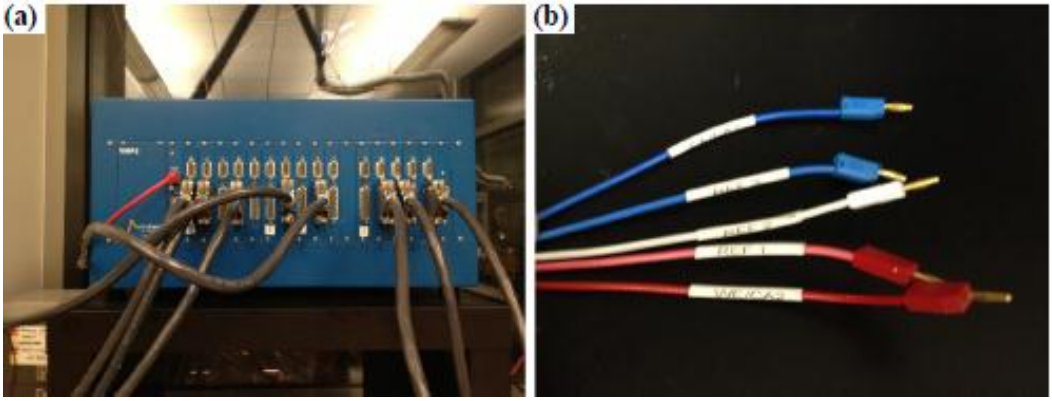


Figure 3.7: (a) VMP3 potentiostat/galvanostat. (b) wires for one channel; the reference lead (white), working lead (red), counter lead (blue) and current and voltage sense leads.

### 3.2.2.1. Cyclic Voltammetry

Cyclic voltammetry (CV), the most widely used technique for acquiring qualitative information about electrochemical reactions, is potentiodynamic measurement mode where the instrument provides and measures the time-dependent current required to maintain a constant rate of potential change (or scan rate) between two potential limits.

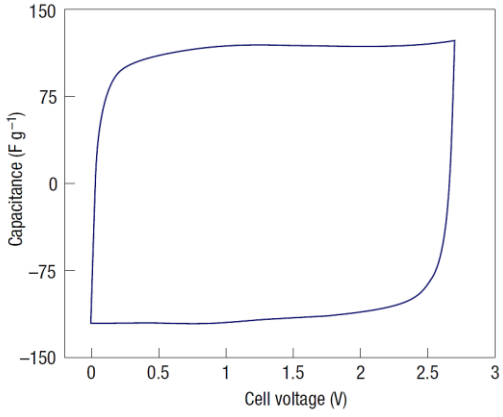


Figure 3.8: Cyclic voltammetry of a two-electrode laboratory EDLC cell in 1.5 M tetraethylammonium tetrafluoroborate $NEt_4^+$, $BF_4^-$ in acetonitrile-based electrolyte.[33]

#### 3.2.2.2. Galvanostatic Cycling

During galvanostatic cycling (GC), current is kept constant until the device reaches a set potential limit. Then the current is reversed, and the cycle is repeated. The resulting instantaneous potential is plotted as function of time. GC is one of the most common techniques to test electrochemical cells due to its simplicity.

#### 3.2.2.3. Electrochemical Impedance Spectroscopy

Electrochemical impedance spectroscopy (EIS) is a steady state technique where a sinusoidal voltage punctuation of small amplitude (typically ± 5 mV) and frequency ($\omega = 2\pi f$) is superimposed to a bias voltage while measuring the current. EIS data is obtained by scanning different frequencies, in general, from 50 kHz to 10 mHz. The voltage applied varies according to equation below.

$$\mathrm{V} = \mathrm{V}_0 + \Delta V \ \sin(\omega t) \tag{9}$$

where $V_0$ is the initial steady state potential of the electrochemical cell (V), $\Delta V$ is amplitude of the signal.

The response of the applied potential is a sinusoidal current, with amplitude of $\Delta I$ and a shifted angle $\varphi$ of phase indicated in equation below.

$$\mathrm{I(t)} = I_0 + \ \Delta I \ \sin(\omega t - \varphi) \tag{10}$$

where $I_0$ is the initial steady state current of the electrochemical cell (A).

With a mathematical transformation, the potential and current can be written as follows.

$$\mathrm{V}(\omega) = V_m \exp(j\omega t) \tag{11}$$

$$\mathrm{I}(\omega) = I_m \exp[j(\omega t - \varphi)] \tag{12}$$

The complex impedance is defined by the ratio of complex potential to complex current. It consists of the real part, corresponding to the resistance and an imaginary part, corresponding to the capacitance.

$$Z_{\omega} = \frac{V(\omega)}{I(\omega)} = \frac{V_m}{I_m}\exp(-j\varphi) \qquad (13)$$

A Nyquist plot can be constructed by plotting the value of the real part of the impedance on the x-axis and the negative of the imaginary part of the impedance on the y-axis. The simple RC circuit models were not able to simulate the real EDLCs with nanoporous electrodes. Therefore, the equivalent circuit model, called as 'Transmission Line Model', was proposed by De Levie in 1963.[107] From De Levie's model, the porous carbon electrodes could be represented by series of RC components as shown in Figure 3.9. The electrode (Figure 3.9b) has uniform cylindrical-shaped pores. Upon potential polarization, adsorption of electrolyte ions takes place at the outer surface of the electrodes. The transport of electrolyte ions from bulk electrolyte to the surface of the electrode produces a resistance that is defined as equivalent series resistance (ESR).

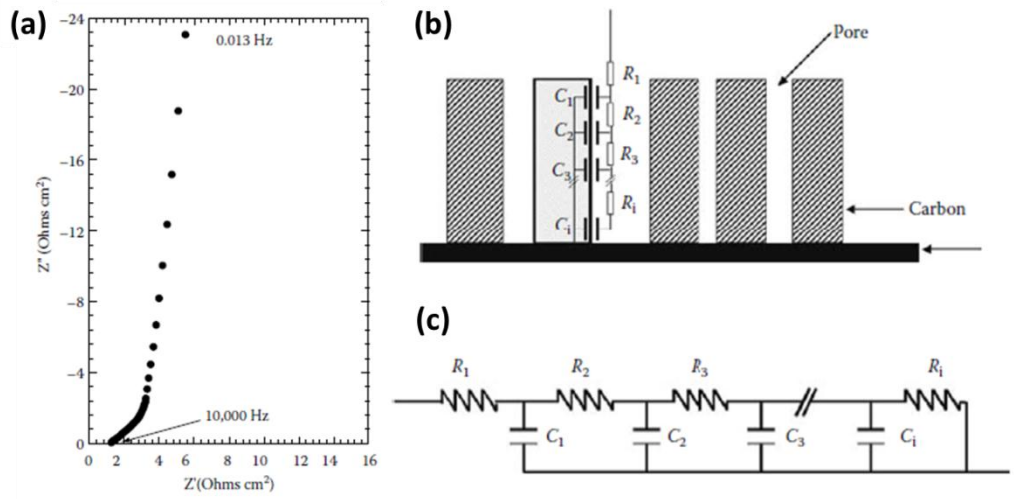


Figure 3.9: (a) Example of Nyquist plot of supercapacitors with activated carbon as electrodes in organic electrolyte. (b) a schematic plot of Transmission Line Model proposed by De Levie and, (c) its equivalent circuit.[108]

As electrolyte ions diffuse into the pores, double layer capacitance $C_1$, $C_2$, $C_3$, …, $C_i$ would be charged with a series of resistance $R_1$, $R_2$, $R_3$, …, $R_i$ (Figure 3.9b). At high frequency, the ions can only reach the outer surface of the electrode with the real resistance of ESR. However, for lower frequency range, where ions have enough time to be able to reach into the pores, ions experience higher resistance which is shown in Figure 3.9a.

A supercapacitor could also be simulated as a combination of a resistor and a capacitor as function of frequency *f* in series: the real part of impedance is the impedance of the resistor R and the imaginary part is the impedance of the ideal supercapacitor $1/(jC\omega)$. Therefore the complex impedance of the combined circuit can be written as an equation below:

$$\mathrm{Z} = \mathrm{R}(\omega) + \frac{1}{j\mathrm{C}(\omega)\omega} = \frac{1}{j\mathrm{C}_{\mathrm{complex}}\omega} = Re(Z) - j\mathrm{Im}(\mathrm{Z}) \quad (14)$$

$$\mathrm{C}_{\mathrm{complex}} = \frac{1}{\omega(j\mathrm{Re}(\mathrm{Z}) - \mathrm{Im}(\mathrm{Z}))} = \frac{j\mathrm{Re}(\mathrm{Z}) - \mathrm{Im}(\mathrm{Z})}{2\pi f(\mathrm{Re}^2(\mathrm{Z}) + \mathrm{Im}^2(\mathrm{Z}))} \quad (15)$$

$$\mathrm{C}_{\mathrm{complex}} = j\mathrm{C}'' + \mathrm{C}' = j\frac{\mathrm{Re}(\mathrm{Z})}{2\pi f(\mathrm{Re}^2(\mathrm{Z}) + \mathrm{Im}^2(\mathrm{Z}))} + \frac{-\mathrm{Im}(\mathrm{Z})}{2\pi f(\mathrm{Re}^2(\mathrm{Z}) + \mathrm{Im}^2(\mathrm{Z}))} \quad (16)$$

Where C' is the supercapacitor capacitance, C" is loss.

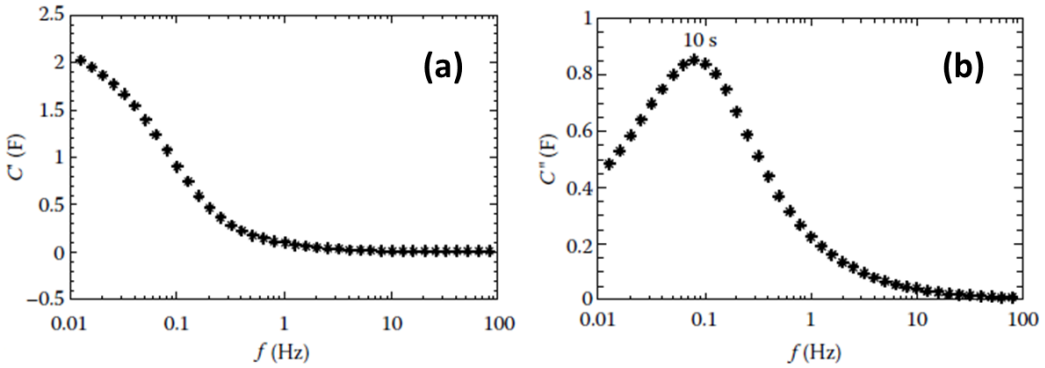


Figure 3.10: (a) Change of the real part of the capacitance (C') vs. frequency. (b) Change of the imaginary part of the capacitance (C") vs. frequency.

The capacitance of a supercapacitor (C') is defined by the plateau at low frequency. From the graph of imaginary part of complex capacitance (C") vs. frequency *f* (Figure 3.10b), time constant τ can be determined as $1/f_{max}$ where the $f_{max}$ is the frequency where C" reaches the maximum value. When the time constant of a supercapacitor is small, the supercapacitor can be fully discharged quicker, which means higher power delivery.

### 3.2.3. Conductivity Measurements

Conductivity was measured on CDC films using 4-point probe that have separate current driving probes and infinite impedance voltage measuring probes. Ideally it allows elimination of contact resistance between the metal electrodes and CDC films. If the sample size is semi-infinite compared to the probe spacing, s, in both diameter and thickness, the resistivity can be obtained by:

$$\sigma = 2\pi s \frac{V}{I} \tag{17}$$

where V is the measured voltage and I is the applied current. If the sample size is too small so it cannot be considered as semi-infinite, correction factors need to be introduced.

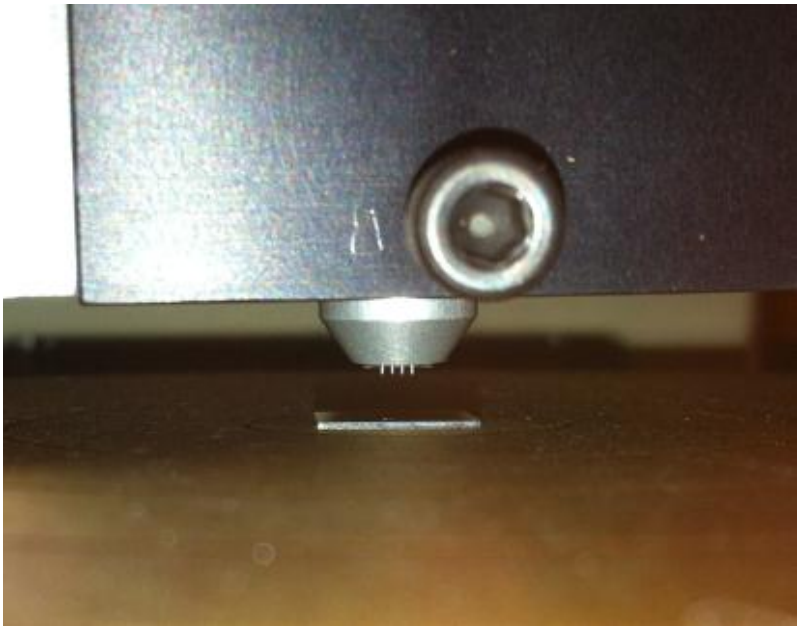

Figure 3.11: 4-point probe measurement on CDC films.

# 4. RESULTS AND DISCUSSION

## 4.1. Development of CDC films

Two different approaches were experimented to synthesize nanoporous carbide-derived carbon films; vacuum decomposition of SiC, silicon carbide and halogenation of TiC, titanium carbide films.

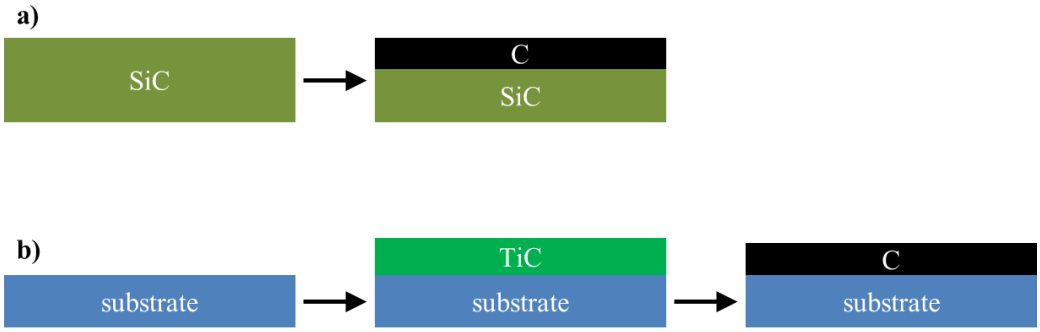


Figure 4.1: Carbide-derived carbon synthesis methods; a) vacuum decomposition of SiC, b) halogenation of TiC.

SiC decomposition requires high energy and vacuum process to break Si-C bonding for CDC film synthesis. Also this process is limited for high crystalline SiC only, which endure the high temperature and vacuum. On the other hand, halogenation of carbide can be processed relatively lower temperature to that of SiC vacuum decomposition. Carbide film is grown by film deposition method and etched by halogenation gas to remove metal element from the carbide film, which will result in porous carbon nanostructured films.

## 4.2. Development of CDC films by Vacuum Decomposition

Since the discovery of carbon nanotubes (CNTs), the synthesis of high quality CNTs using various methods such as arc discharge, laser vaporization, pyrolysis, and chemical vapor deposition, have been focused on.[109-112] The outstanding structural, electrical and mechanical properties of CNTs have generated considerable interest in their application such as field emission sources for display, scanning probes, nanotransistors, supercapacitors or rectifiers. Kusunoki et al. have reported densely-packed and aligned CNTs formed vertically on a 6H-SiC(0001) surface by annealing the substrate at 1700 °C in high vacuum.[74, 77, 79, 113, 114] So-called 'surface decomposition' process let CNTs grow without the help of any catalytic reaction of metals or gases. SiC surface decomposition has been known as the only way of non-catalytic CNT formation, by which well-aligned CNTs grow on SiC (0001) wafers.

Using a vacuum furnace, CDC was synthesized by decomposition of SiC single crystalline wafers. SiC crystal substrate was cut into small pieces by around 1 cm by 1 cm and put into the vacuum furnace. The chamber was pumped down until it reached higher vacuum than $10^{-5}$ torr. Once $10^{-5}$ torr was reached and maintained, heating started with a ramping rate of 10 °C/min. Dwell time at decomposition temperature varied from couple of hours to longer than 10 h. Temperature and dwell time was varied to see the CDC films growth rate and trend with different temperature and dwelling time.

CDC films were successfully synthesized at varied temperatures between 1500 °C and 1900 °C. Structure and morphology was examined by SEM, TEM and Raman spectroscopy. From SEM and TEM images, it appears to be mixed structure of vertically grown multi-layered carbon sheets and multi-wall carbon nanotubes.

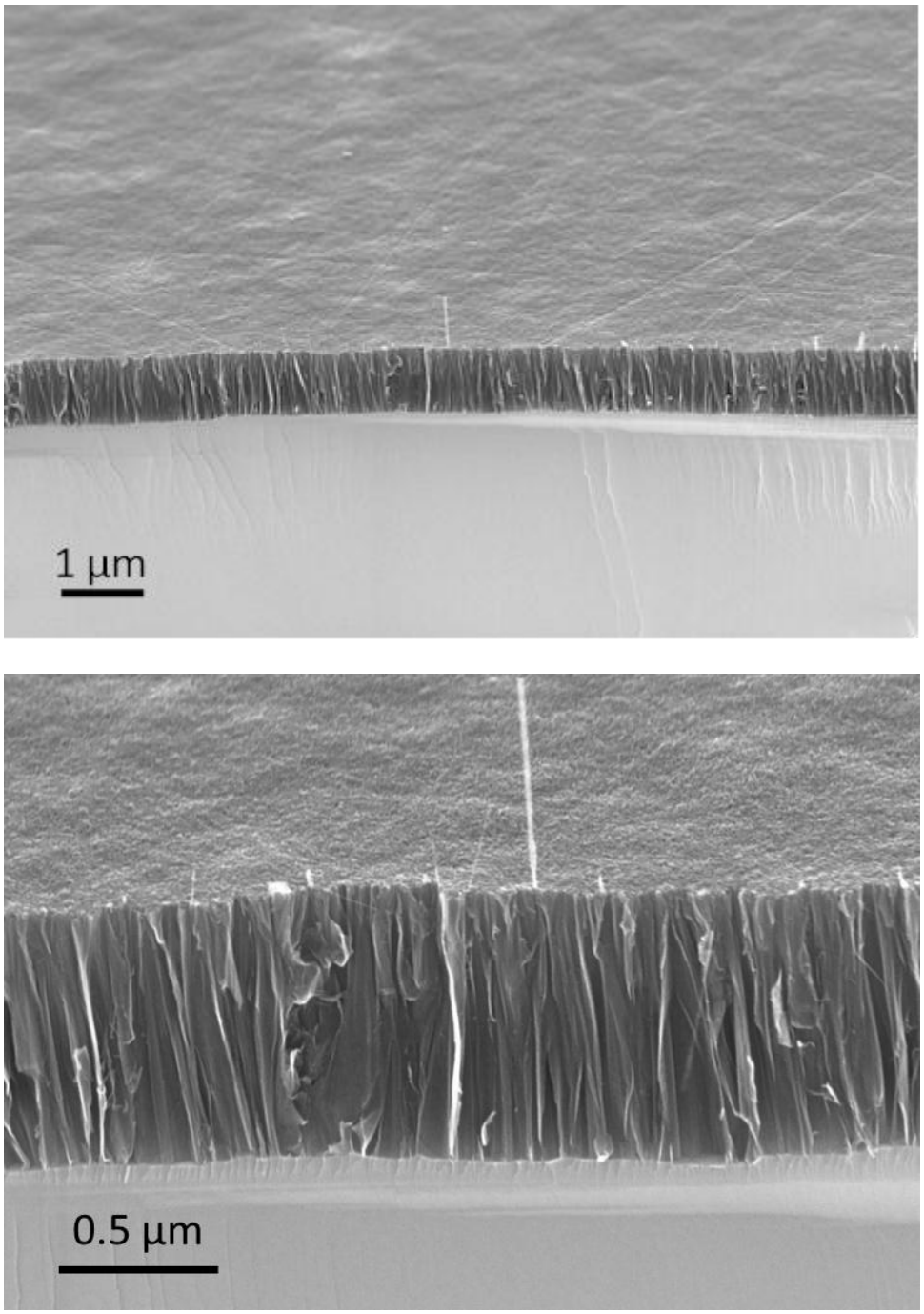


Figure 4.2: SEM micrographs of SiC-CDC films grown by vacuum annealing at 1800 °C

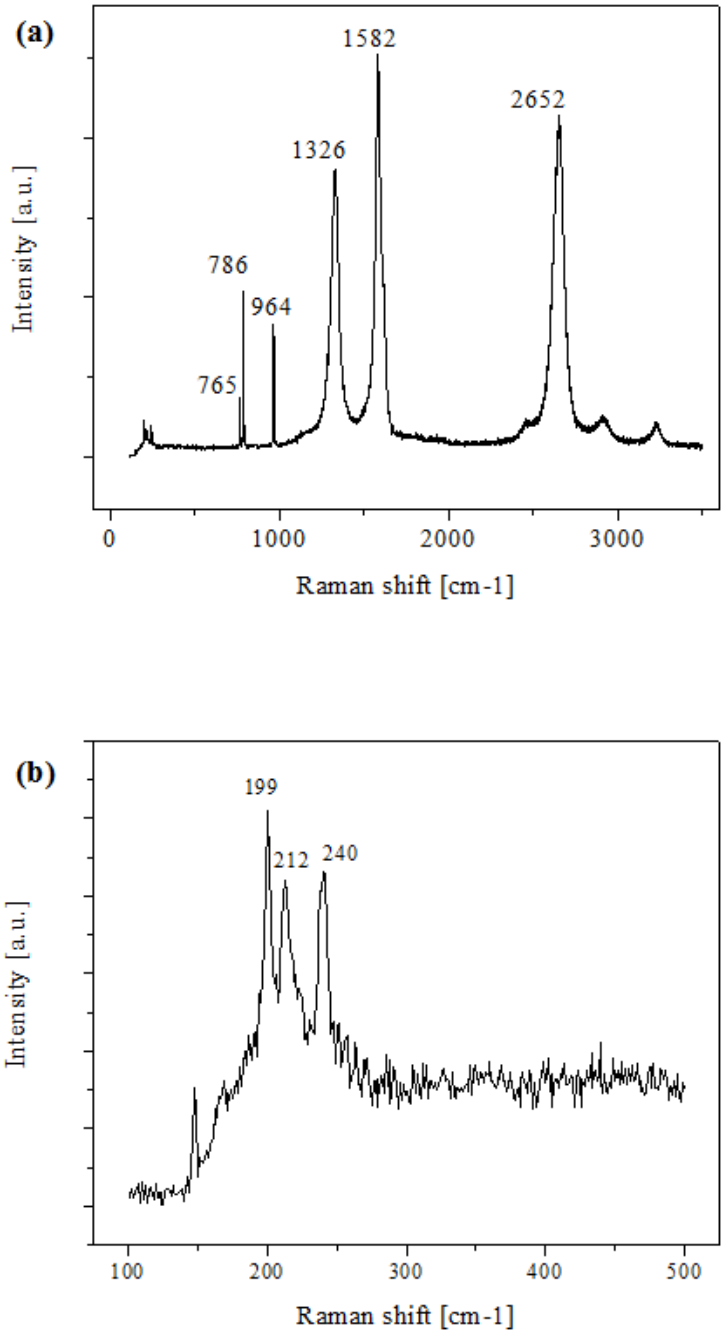


Figure 4.3: (a) Raman spectrum of CDC films on SiC synthesized at 1700 °C 4 h and, (b) RBM modes of MWCNTs.

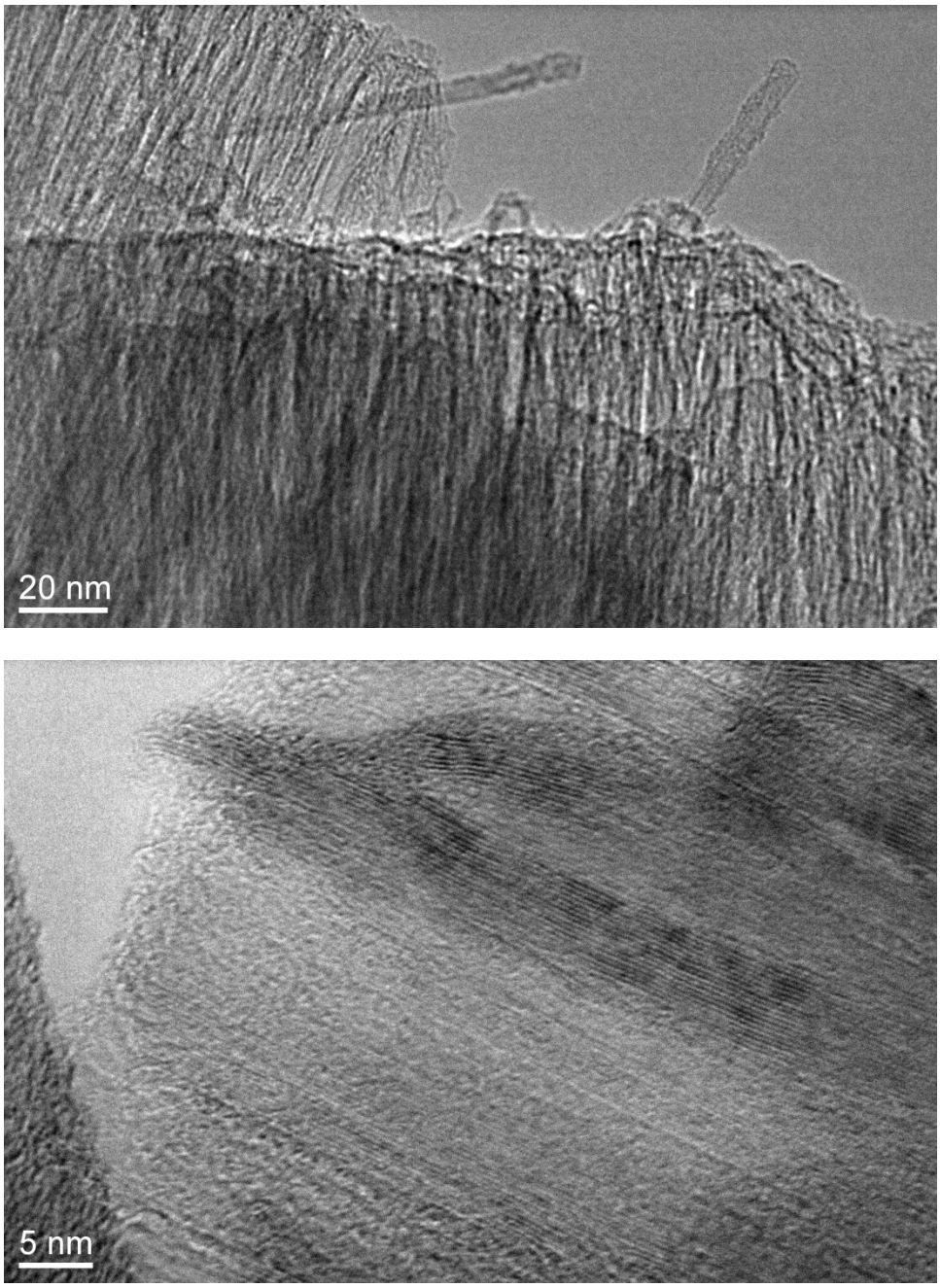


Figure 4.4: TEM micrographs of SiC-CDC film synthesized at 1675 °C

Fig. 4.2 and Fig. 4.3 show that CDC film synthesized by vacuum anneal of SiC single crystal wafer is composed of vertically-grown carbon sheets and multi wall carbon nanotubes. Also the sharp peak of carbon bands (1326 $cm^{-1}$, 1582 $cm^{-1}$, 2652 $cm^{-1}$) in Raman spectra indicates that the carbon film is highly ordered. RBM modes of MWCNTs were observed from all of CDC films synthesized between 1500 and 1800 °C. Since RBM peak positions are not consistent among samples from different synthesis temperature as well as within same sample, the diameter of MWCNTs varies over the CDC films. It is because of the nature of SiC decomposition process and SiC wafer's surface condition. Kusonoki et al. used density-functional molecular dynamics study to explain the growth mechanisms for carbon nanostructure formation on SiC.[115] It was predicted that at lower temperature, due to low carbon surface diffusion, more CNTs tend to grow on SiC instead of carbon sheets or graphene.

Table 4.1: SiC-CDC thickness and growth rate on different vacuum annealing temperature ranging from 1500 °C to 1800 °C.

| Temperature (°C) | Thickness (nm) | Time (h) | Growth rate (nm/h) |
|---|---|---|---|
| 1500 | 100 | 4 | 25.0 |
| 1550 | 115 | 4 | 28.8 |
| 1600 | 200 | 4 | 50.0 |
| 1650 | 245 | 4 | 61.3 |
| 1675 | 367 | 4 | 91.8 |
| 1700 | 465 | 4 | 116.3 |
| 1750 | 570 | 4 | 142.5 |
| 1800 | 650 | 4 | 162.5 |

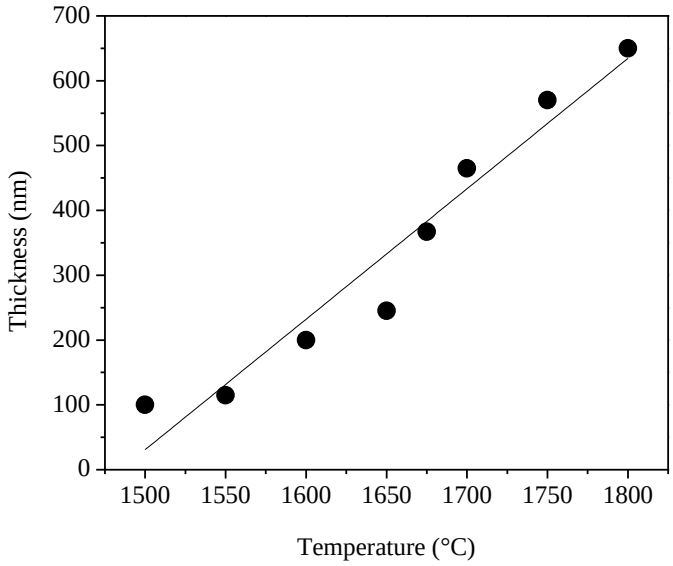


Figure 4.5: Thickness of SiC-CDC grown for 4 h at different vacuum anneal temperature ranging from 1500 °C to 1800 °C.

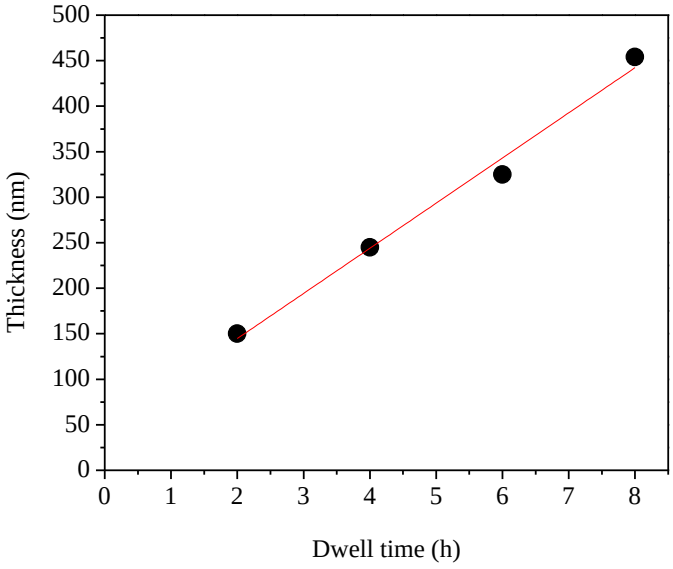


Figure 4.6: SiC-CDC thickness versus dwell time at 1650 °C.

Vacuum decomposition of SiC is a slow process. In general, the higher the process temperature is, the faster the process becomes. CDC film growth rate by SiC vacuum anneal was calculated using thickness measured by SEM as shown in Table 4.1; 25 nm/h for 1500 °C, the lowest temperature and 162.5 nm/h for 1800°C, the highest in the table. SiC-CDC film growth rate increases linearly with vacuum anneal temperature. In addition, as shown in Fig.4.6, SiC-CDC film thickness is proportional to dwell time at chosen anneal temperature. It means that there is no material transport issue for SiC decomposition process in high vacuum such as $< 10^{-5}$ torr.

In spite of successful synthesis of SiC-CDC by vacuum decomposition, the strong adhesion between CDC film and SiC wafer kept the experiments from moving further toward electrochemical characterization of SiC-CDC films. Epoxy was applied to the top of SiC-CDC film to transfer but didn't work to take CDC film off the SiC substrate. Some metal layers such as Ti, Cr and Au were also tried by deposition on top of SiC-CDC film on SiC to see if CDC film can be transferred. But only metal layers were peeled off without any trace of CDC film onto it. Since SiC-CDC film has stable chemical bonding with SiC crystalline substrate, it was not possible to make further progress with electrochemical cell to test those CDC films on non-conducting wafer.

## 4.3. Development of CDC films by Chlorination

One of the most common carbide materials, titanium carbide, TiC was selected as a source material for CDC film synthesis, since TiC powder material has been studied for decades by many researchers and well documented. It is well-known that nanoporous

carbon material synthesized from TiC powder has mostly micropores, size of which matches well with organic electrolyte that is commonly used for supercapacitors.[17, 67, 84] More importantly TiC can be grown as a film via either chemical vapor deposition (CVD) or physical vapor deposition (PVD) techniques.[116] For crystalline carbide film growth, PVD or sputtering was chosen over CVD because CVD technique requires more thermal energy – at least above 1000 °C – to grow crystalline carbide films than PVD does. The process temperature needs to be kept as low as possible to prevent substrate materials from reacting during the deposition process.

### 4.3.1. Composition and Structure of TiC and TiC-CDC films

For TiC films grown on sapphire substrate ($Al_2O_3$), thickness and composition were analyzed by WDXRF and XRD analysis showed the crystal structure of each TiC films.

Table 4.2: Thickness and composition of TiC films analyzed by WDXRF.

| | thickness (nm) | Titanium (at%) | Carbon (at%) |
|---|---|---|---|
| TiC-98 | 451 | 77.9 | 22.1 |
| TiC-99 | 391 | 39.7 | 60.3 |
| TiC-100 | 471 | 43.0 | 57.1 |
| TiC-101 | 380 | 42.0 | 58.0 |
| TiC-102 | 378 | 47.4 | 52.6 |
| TiC-103 | 242 | 41.5 | 58.5 |
| TiC-104 | 223 | 41.3 | 58.7 |

Wide range of TiC compositions was tried and most of them had continuous films after deposition. But it was found that excessively Ti-rich or C-rich films are not suitable for CDC film synthesis. During the chlorination process Ti atoms are removed from the TiC film as $TiCl_4$ in gas phase and carbon atoms should maintain a structure to form a CDC film. However for Ti-rich or C-rich films, the portion of thermodynamically stable Ti-C bond in the film is smaller than in films with composition close to Ti:C = 50:50 stoichiometry. As a result, during chlorination it was seen that Ti-rich or C-rich films tend to be etched more by chlorine gas and remaining CDC films failed to form a solid structure, and instead tend to have more cracks or non-conformal structures. More importantly, as a means to control the pore size of CDC films, it would be ideal for the starting carbide material to have uniform atomic structure. In order to take most advantage of porosity of TiC-CDC films for micro-supercapacitors, Ti:C ratio was kept close to 50:50.

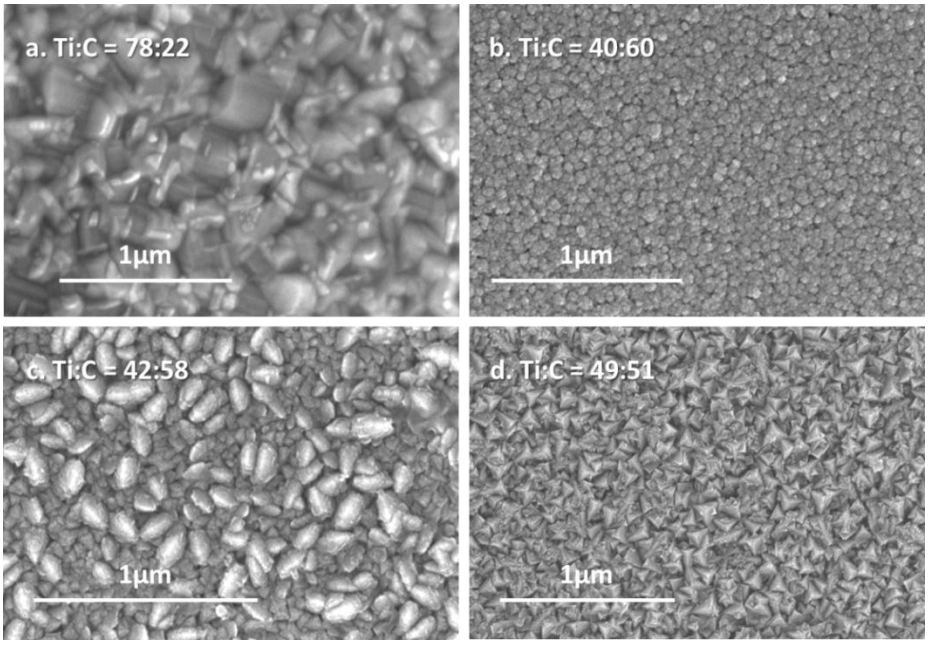


Figure 4.7: Morphology of TiC films with different Ti:C ratios.

In crystalline structural perspective, TiC cubic structure would be best starting material since carbon structure left after chlorination is of most interest for electrode material. For Ti-rich film, excessive titanium atoms result in cubic and hexagonal phase of titanium as well as TiC cubic structure. These cubic or hexagonal titanium phases causes issues during chlorination because there will be no carbon film growth where Ti phase was dominant due to local carbon deficiency, which leads to voids and micro-cracks and eventually discontinuity in CDC film.

For C-rich films, Ti metal phase was not observed but broad carbon peak was detected, which was mainly because of excessive carbon without bonding to any adjacent titanium atoms to participate in TiC lattice.

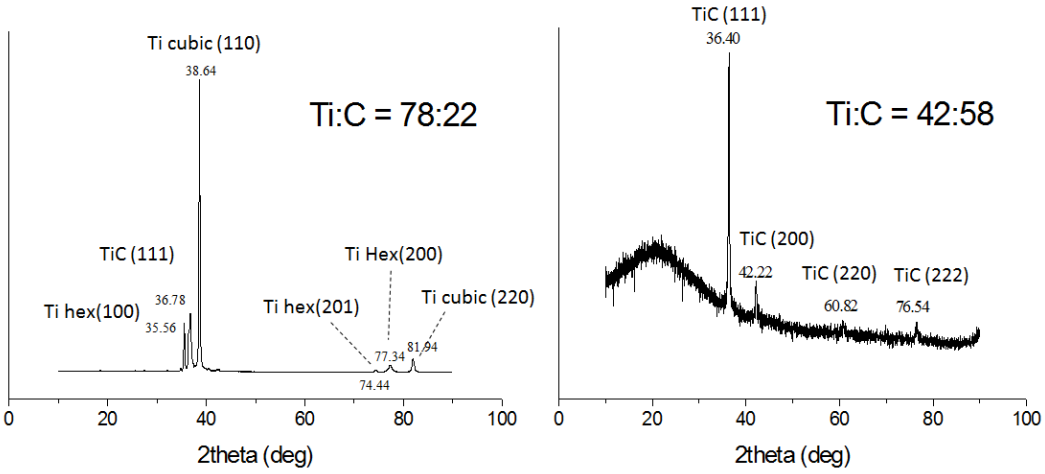


Figure 4.8: X-ray diffraction results: (a) Ti-rich film on $Al_2O_3$ has mostly Ti and small amount of TiC structure, (b) in C-rich film on $Al_2O_3$, no Ti cubic structure is seen and amorphous carbon's broad background confirms excess free carbon in the film.

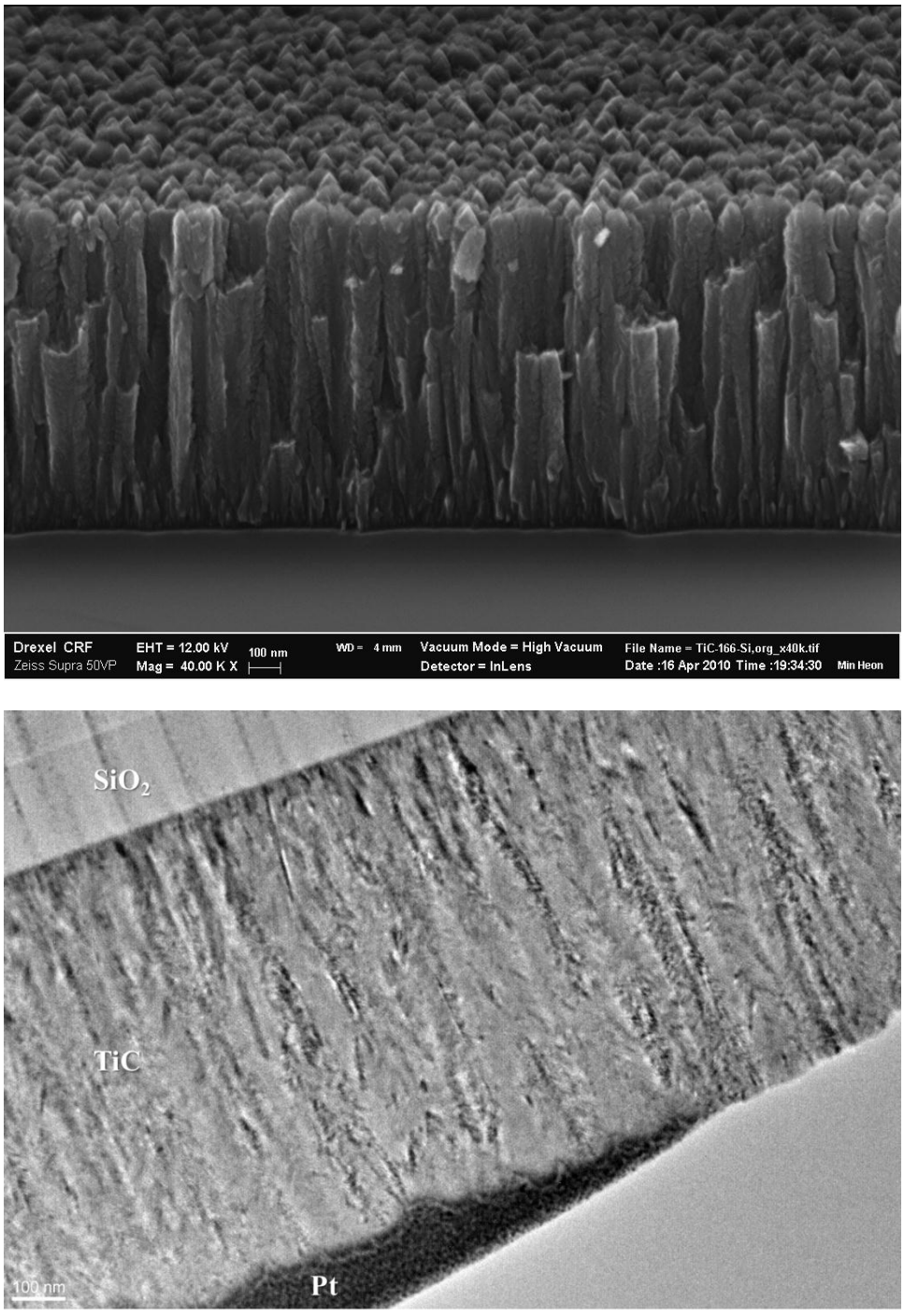


Figure 4.9: SEM and TEM micrograph of TiC film grown on $SiO_2$ wafer.

| Ring | Radius (1/nm) | **1/Radius (nm)** | Hough Sum | Profile Peak |
|---|---|---|---|---|
| 1 | 4.018 | **0.249** | 65878 | 76 |
| 2 | 4.621 | **0.216** | 116396 | 100 |
| 3 | 6.52 | **0.153** | 88717 | 50 |
| 4 | 7.624 | **0.131** | 23102 | 22 |
| 5 | 8.029 | **0.125** | 26626 | 21 |
| 6 | 9.291 | **0.108** | 16247 | 13 |
| 7 | 9.983 | **0.1** | 12259 | 11 |
| 8 | 10.31 | **0.097** | 20692 | 14 |
| 9 | 11.267 | **0.089** | 15006 | 10 |
| 10 | 11.446 | **0.087** | 16807 | 10 |
| 11 | 12.135 | **0.082** | 8148 | 7 |

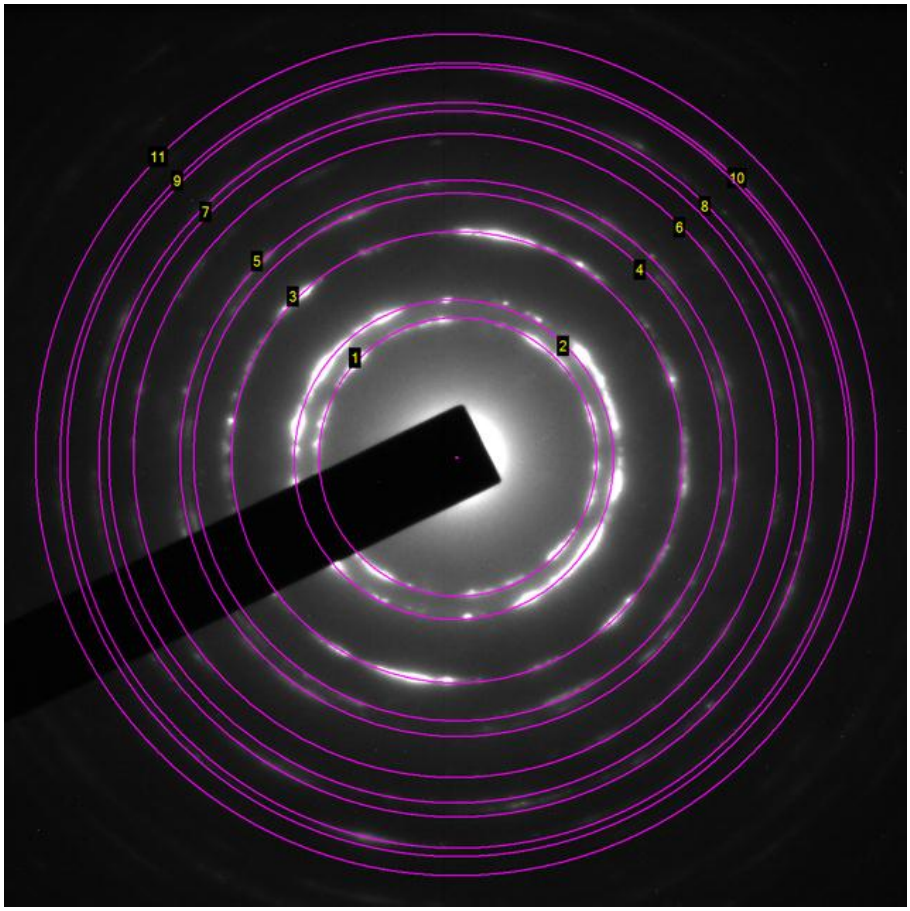


Figure 4.10: Analysis of electron diffraction rings of TiC film in TEM; diffraction pattern confirms textured-TiC has a cubic structure.

A TiC film (Ti 56.6 at%, C 43.4 at% by WDXRF) deposited on silicon oxide wafer was characterized by SEM and TEM. As shown in Fig 4.9, the TiC film had well-developed texture of polycrystalline structure which was confirmed as face centered cubic crystal structure by diffraction pattern in TEM. This TiC film was etched by chlorine gas at 300°C for 5 minutes then was observed by TEM. No electron diffraction ring was seen from the TiC-CDC film indicating this CDC film has amorphous structure. Also there is macro slit pores found between columnar structures of TiC-CDC. This is caused by the volume shrinkage that was generated when TiC film transforms to CDC film. It is because larger Ti atoms (molecular single bond covalent radius 136 pm at CN=4) are removed from TiC film, even though C atoms (molecular single bond covalent radius 75 pm at CN=4) manage to maintain the shape of the film and columnar morphology of the film.

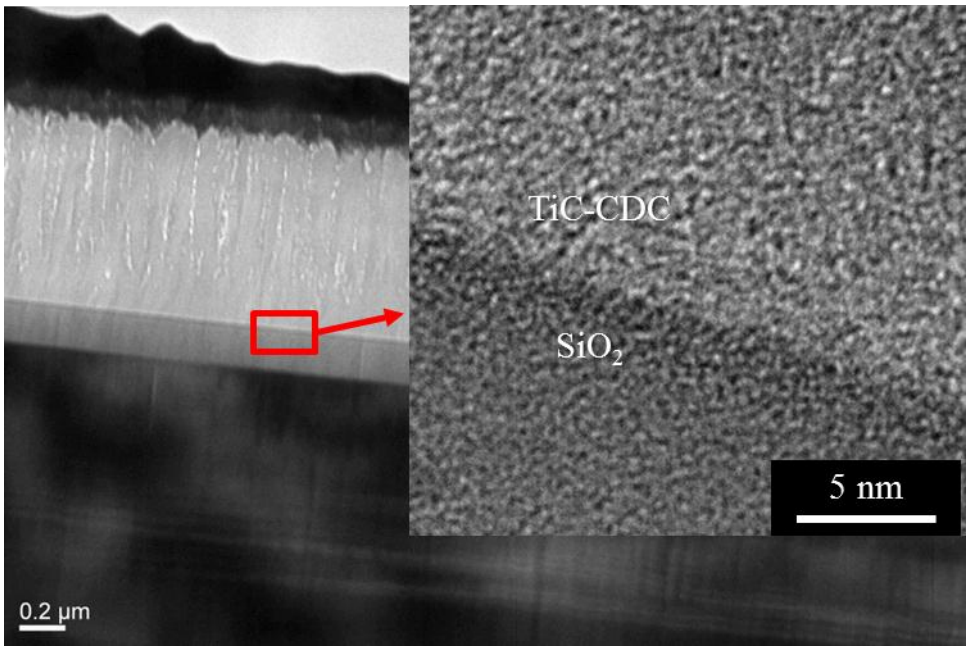


Figure 4.11: TEM micrograph of TiC-CDC film on $SiO_2$ wafer.

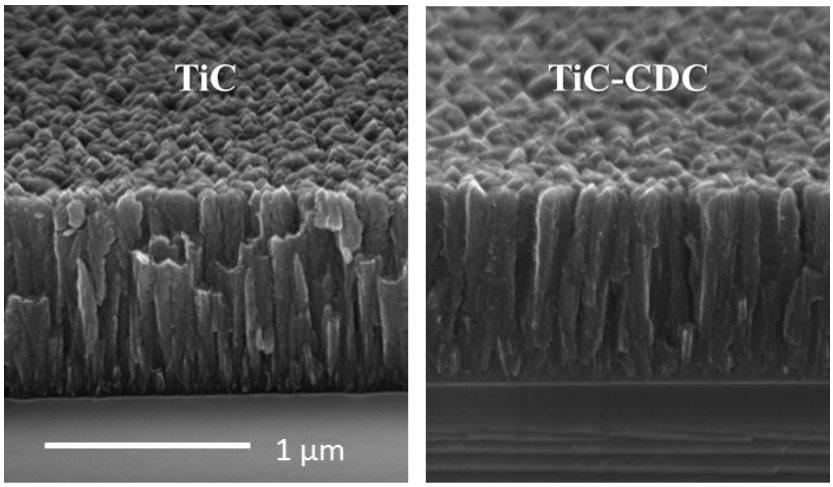


Figure 4.12: SEM micrographs of TiC and TiC-CDC films.

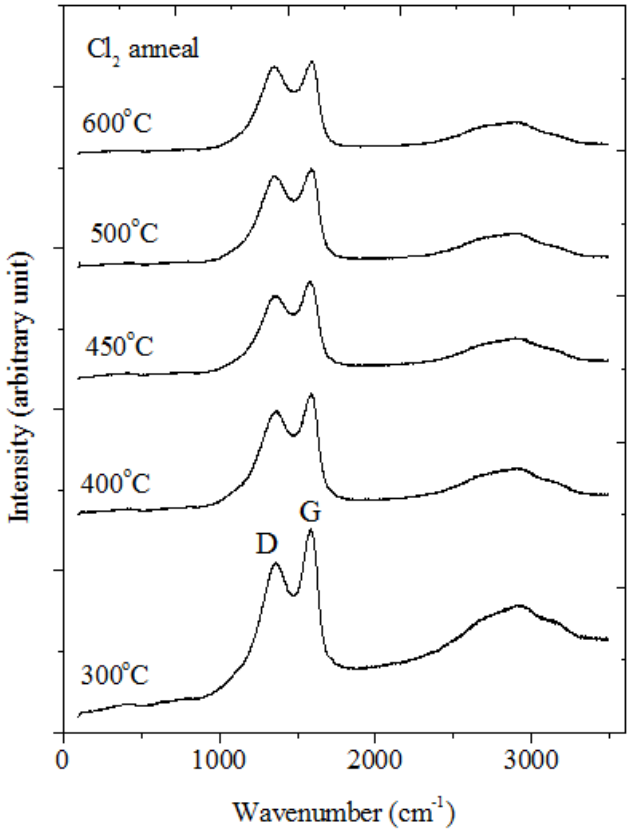


Figure 4.13: Raman spectrum of TiC-CDC films synthesized at different temperatures.

TiC film grown on $SiO_2$ wafer successfully transformed to TiC-CDC film with the film shape and morphology maintained as seen in fig.4.12. Raman spectra also show that just like TiC-CDC powder, TiC-CDC films have disordered carbon structure based on the broad peak of D-band and G-band. As the chlorine etching temperature increases, intensity of D-band become larger compared to that of G-band, which is in good agreement with the study on TiC-CDC powder.[84]

### 4.3.2. TiC and TiC-CDC films on various substrates

Textured TiC films were able to grow on different substrate materials; HOPG (Highly Ordered Pyrolytic Graphite), Glassy Carbon, $Al_2O_3$, and $SiO_2$ wafer. It should be noted that substrate materials must not be damaged under chlorine atmosphere.

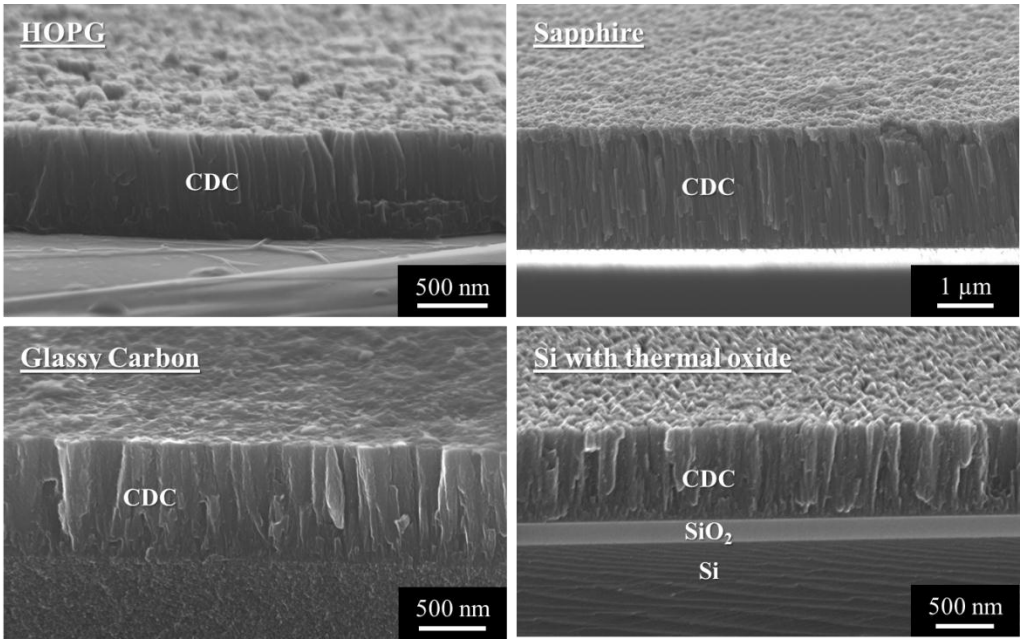


Figure 4.14: TiC films on HOPG, Sapphire, Glassy Carbon, and Silicon Oxide wafer.

Primarily, the film synthesis is intended for achieving continuous nanoporous carbon films on Si wafer for microfabrication but since carbon thin film on non-conductive substrate is very complicated to test electrochemically without damaging the synthesized carbon film, we utilized conductive substrates such as HOPG and glassy carbon.

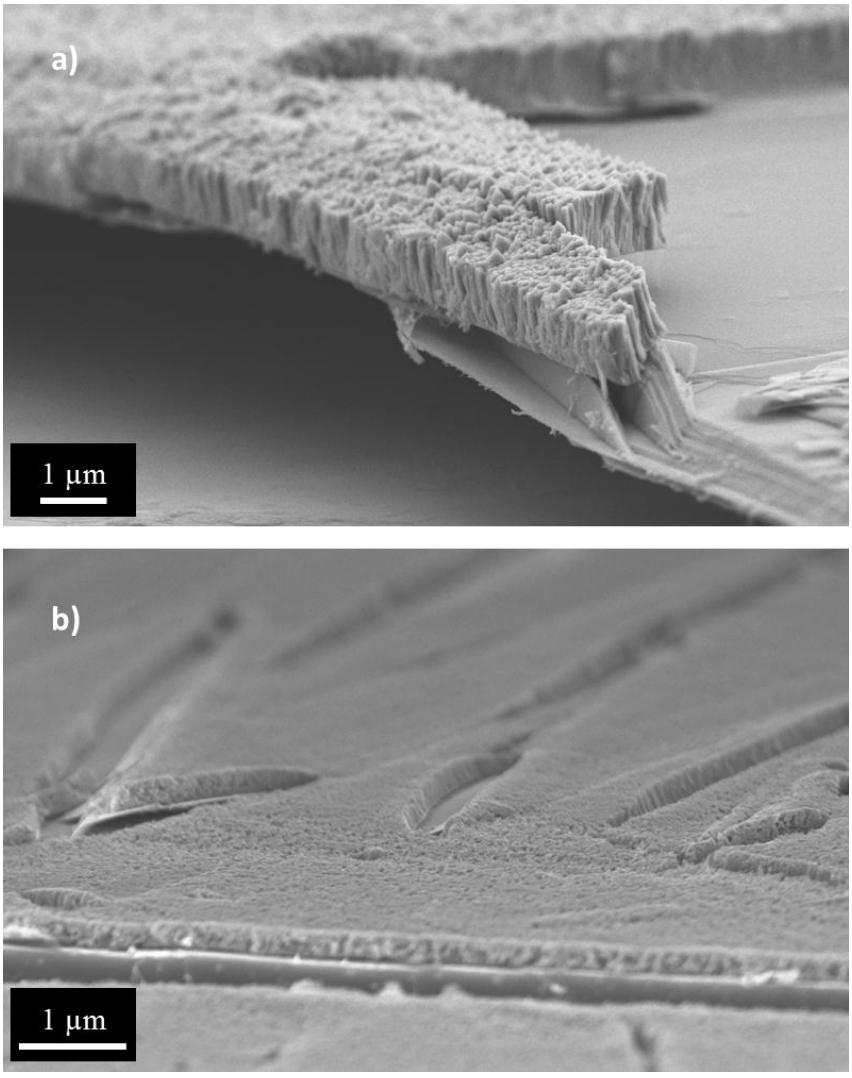


Figure 4.15: a) Textured TiC film, b) TiC-CDC film on HOPG.

It was found that HOPG's intrinsic feature lamellar structure doesn't provide a good adhesion to carbide films. Additionally HOPG's graphite layers tend to deform easily to accommodate the stress of the film before and after chlorine etching.

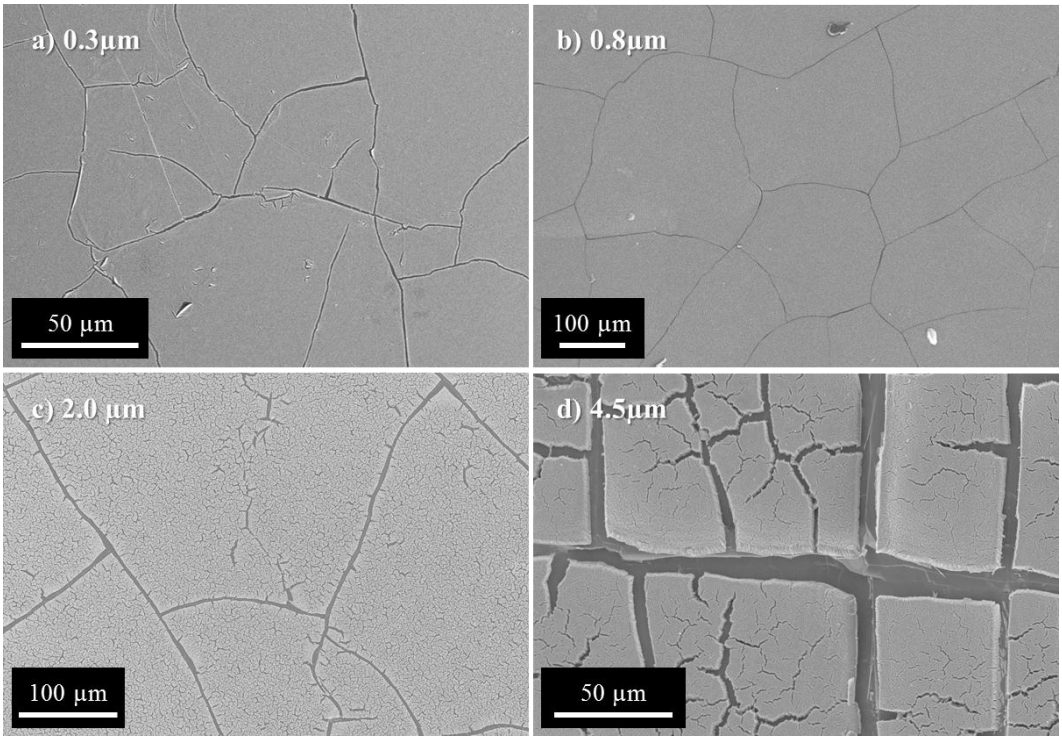


Figure 4.16: SEM micrographs of TiC-CDC films on HOPG, synthesized at 500°C.

TiC-CDC film on HOPG showed high density of cracks after chlorination. As shown in Figure 4.15 and 4.16, more crack formed in thicker films due to internal stress build-up by removal of Ti atoms during chlorination. Not only HOPG but also silicon oxide wafer were tested to see how micro-cracking evolves along substrate materials. The trend was similar; as TiC films become thicker, more micro-cracking occurred in TiC-CDC after chlorine etching process between 300~600 °C.

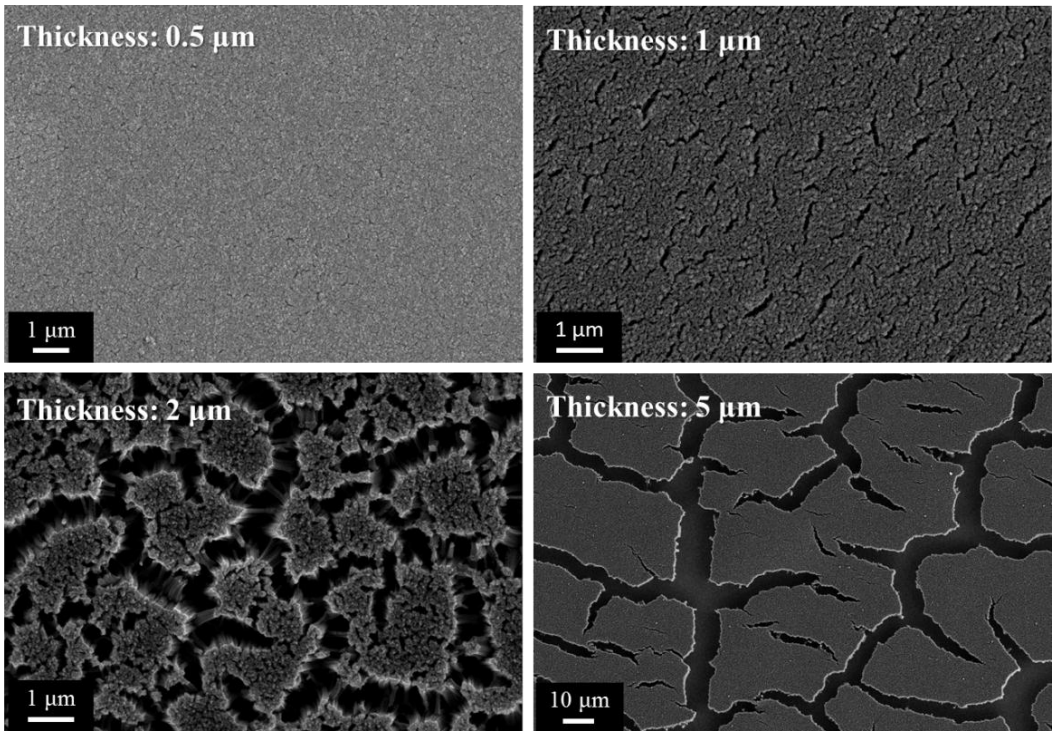


Figure 4.17: TiC-CDC films on silicon oxide wafer, chlorinated at 500 °C for 15 minutes.

### 4.3.3. Chlorine Gas Etching to Synthesize TiC-CDC films

Stress-free textured TiC film would be ideal for microcrack-free TiC-CDC film synthesis. Other than deposited TiC film, chlorine etching process is critical to TiC-CDC conversion. From the Raman spectra (Fig. 4.13) and TEM micrographs on TiC-CDC synthesized at different temperature, it indicates that chlorine etching temperature between 300 °C and 600 °C does not affect the amorphous carbon structure of TiC-CDC films much. However how long TiC film is etched by chlorine does affect the TiC-CDC, because chlorine reacts not only with titanium but also with carbon. Once titanium is removed while film shape is retained, then carbon is also etched away during the process.

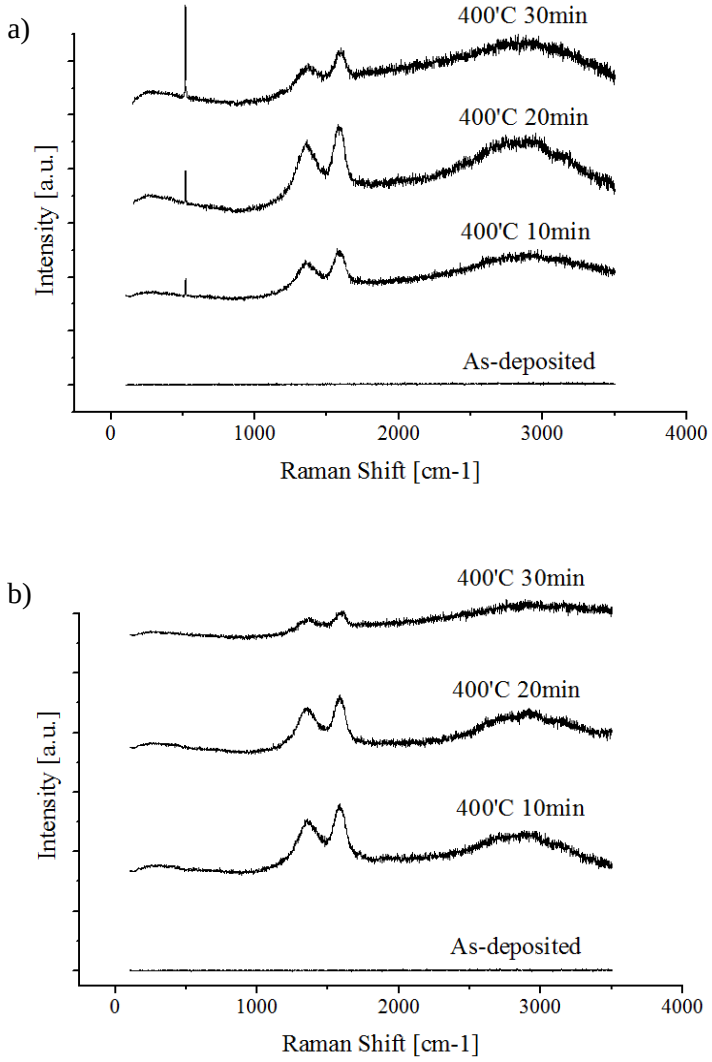


Figure 4.18: Effect of chlorine etching time to synthesize TiC-CDC film on a) silicon oxide wafer and, b) sapphire wafer.

Thermodynamic simulation is not able to predict the kinetics of TiC to TiC-CDC conversion by gas etching except for the stable phase at certain temperatures. Therefore by repeated experiments on different etching process time, TiC-CDC film was observed under SEM microscope and measured by Raman spectroscopy after chlorine etching.

Between 300 °C and 600 °C range, it was concluded that chlorine etching process time needs to be less than 10 minutes to minimize carbon loss in our experimental setup. At 600 °C, even 3 minutes of etching appeared to be fine for full conversion of TiC to TiC-CDC film. It should be noted that TiC film itself need to be considered for the etching process time because lower crystallinity TiC film tend to be etched more easily, so requires shorter etching time to synthesize TiC-CDC.

### 4.3.4. Electrical Conductivity of TiC-CDC Films

For one of essential properties as electrodes, electrical resistivity was measured by using 4-point probe (Jandel Engineering Four Point Probes, UK) and compared between TiC-CDC films synthesized via different processes including chlorine gas etching, hydrogenation (20 min) and vacuum anneal (RTA).

Table 4.3: Resistivity of TiC-CDC films synthesized at various conditions.

| Synthesis condition | Current (mA) | Voltage (mV) | Resistivity (μohm·cm) |
|---|---|---|---|
| TiC grown on silicon oxide | 10 | 0.023 | 0.7 |
| 600 °C for 1 min | 10 | 5.15 | 226.5 |
| 500 °C for 5 min | 10 | 10.19 | 448.1 |
| 450 °C for 10 min | 10 | 4.452 | 195.8 |
| 450 °C for 5 min | 10 | 8.065 | 354.6 |
| 450 °C for 5 min ($H_2$) | 10 | 16.41 | 721.6 |
| 400 °C for 5 min | 10 | 9.31 | 409.4 |
| 400 °C for 5 min ($H_2$) | 10 | 49.37 | 2174.4 |
| 400 °C for 5 min ($H_2$) RTA at 1000 °C for 1 min | 10 | 1.33 | 54.4 |
| 300 °C for 5 min | 10 | 33.53 | 1476.8 |
| 300 °C for 5 min RTA at 1000 °C for 1 min | 10 | 1.15 | 49.8 |
| 300 °C for 5 min ($H_2$) | 10 | 55.47 | 2443.1 |
| 300 °C for 5 min ($H_2$) RTA at 1000 °C for 1 min | 10 | 0.819 | 33.5 |

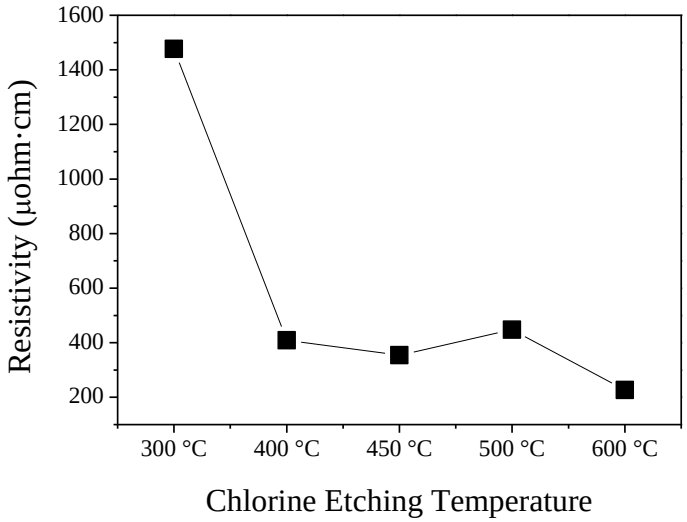


Figure 4.19: Resistivity of TiC-CDC films synthesized at different temperature.

TiC-CDC's electrical resistivity is much lower when compared to graphite carbon (3500 μohm·cm) over the all chlorine etching temperatures between 300 and 600 °C. When comparing CDC films from different chlorine etching temperature, CDC film chlorine-etched at 300 °C has highest resistivity. Then resistivity is similar for 400 °C – 500 °C, and lowest for 600 °C. Interestingly resistivity increases after hydrogen treatment which is to clean up the residual byproduct mostly. Chlorine etching is followed by hydrogen treatment continuously for some films. Largely there might be two reasons for resistivity increase in hydrogen-treated CDC films. First, titanium chloride and other byproducts are playing a role in electrical conductivity by bridging the pores and columnar structures of carbon films. Second, hydrogen treatment was processed at the same elevated temperature as chlorine etching. Longer stay at high temperature leads more thermal-induced issues like micro-cracking and even peeling.

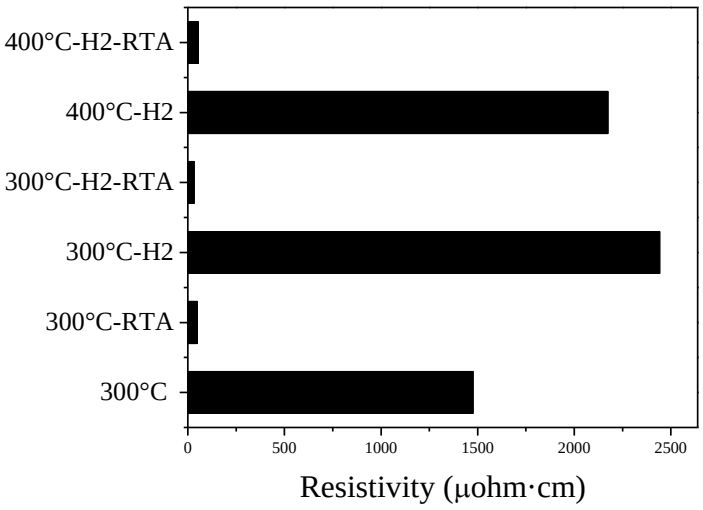


Figure 4.20: Resistivity of TiC-CDC films before and after treatment; H2 stands for hydrogen treatment that is a continuous process after chlorine etching, RTA for rapid thermal annealing which is one of common vacuum thermal treatment process for Si wafers.

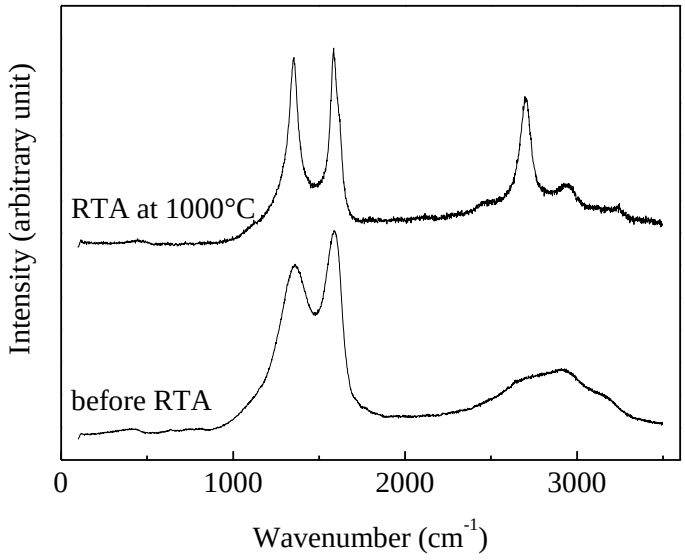


Figure 4.21: Raman spectra of TiC-CDC films synthesized at 300 °C ($Cl_2$-$H_2$).

Rapid thermal annealing made TiC-CDC film's resistivity increase by two orders of magnitude, which can be explained by carbon structural change observed in Raman spectra (Figure 4.21). D-band and G-band width become much narrower and sharper after RTA, meaning carbon structure is more organized in atomic structure. However due to the rapid heating and cooling, micro-cracks developed further as shown in Figure 4.22.

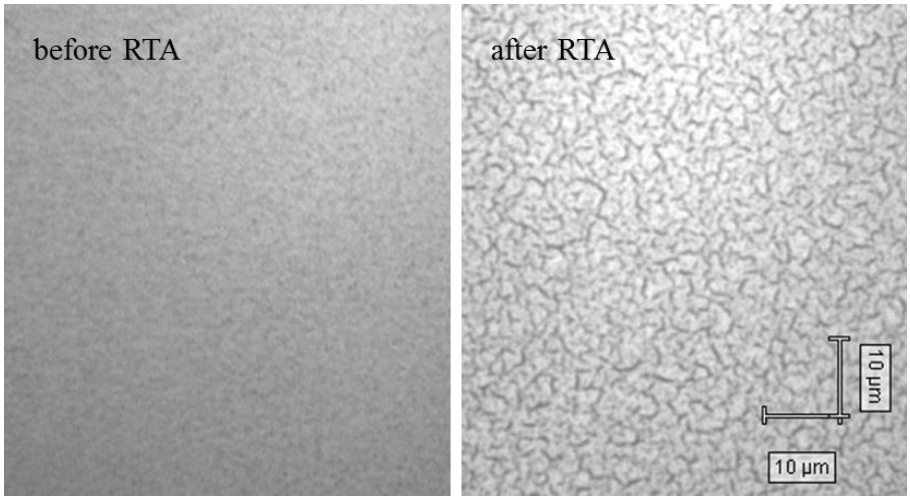


Figure 4.22: Optical microscope images of TiC-CDC film before and after RTA treatment at 1000 °C for 5 minutes. TiC-CDC film was synthesized at 300 °C by chlorine etching for 5 minutes and hydrogen treatment for 20 minutes.

Microcracks should be restrained by controlling ramping and cooling time. Since state-of-the-art RTA tools utilize 'flash' anneal in milliseconds, thermal treatment profile for CDC films can be tuned to improve resistivity without increasing in-plane defects such as microcracks.

### 4.3.5. Electrochemical properties of TiC-CDC Films

Electrochemical characterization was carried out with TiC-CDC films on glassy carbon substrate in a 2-electrode setup. Electrochemical cell was composed of two 15 mm-diameter stainless steel rods with the carbon film on glassy carbon substrate and activated carbon electrode in-between, separated by a PTFE separator (Scheme 1). 1.5 M tetraethylammonium tetrafluoroborate ($TEABF_4$) in acetonitrile was used as an electrolyte. More than 20 mg of activated carbon electrode with 5 wt% of PTFE was used as the counter electrode, so that it could be regarded as a quasi-reference (constant-potential) electrode. Cyclic voltammetry, impedance spectroscopy and galvanostatic cycling were conducted using a Biologic VMP3 potentiostat on the 2-electrode cells.

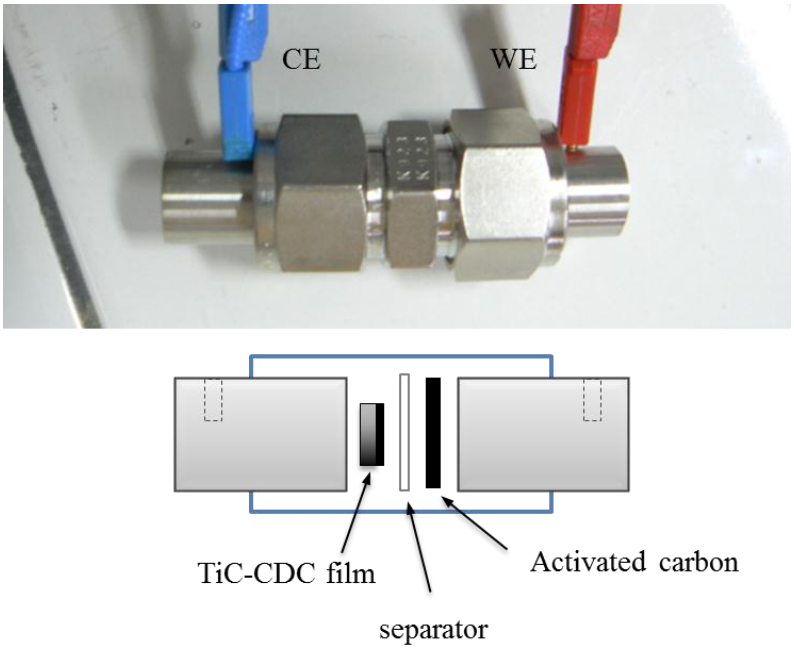


Figure 4.23: 2-electrode cell for electrochemical characterization.

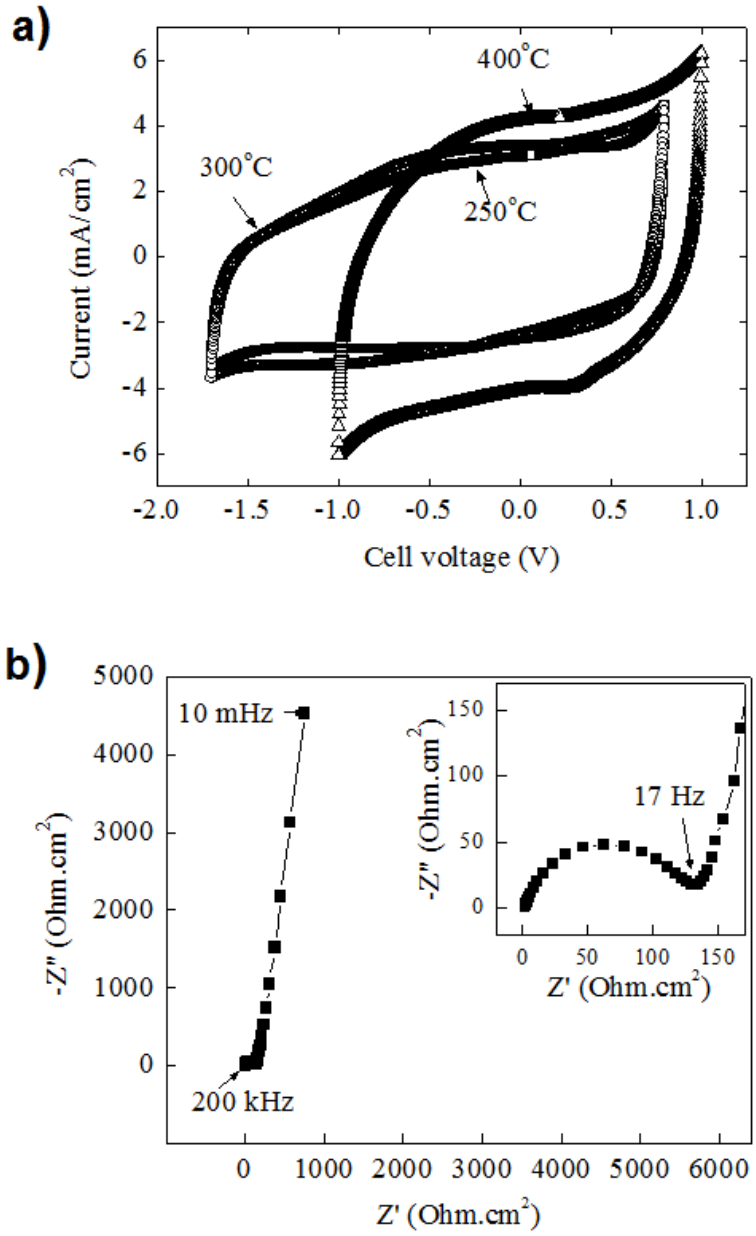


Figure 4.24: a) Cyclic voltammetry of TiC-CDC films synthesized at 250, 300, and 400 °C, respectively, b) Nyquist impedance plot of TiC-CDC films synthesized at 300 °C.

Cyclic voltammetry and electrochemical impedance spectroscopy results in Fig. 4.24 a and b respectively, indicates that TiC-CDC films show an capacitive behavior typical

for an electric double layer capacitor. TiC-CDC film synthesized at 400 °C showed volumetric capacitance 188 $Fcm^{-3}$ at 20 $mVs^{-1}$ scan rate. It is comparably higher than activated carbon's 100 $F/cm^3$.

TiC-CDC films' capacitance decreases as the chlorine gas etching temperature decreases, which is caused by pore size change. The average pore size of TiC-CDC film becomes closer to the electrolyte's ion size. This is in agreement with the published result on the capacitive behavior of TiC-CDC powder.[103] It was shown that when the average pore size is too small for cations or anions to diffuse into, then distortion on CV was observed, resulting in capacitance decrease.[117] In Fig. 4.24, it can be seen that at negative potential, larger TEA ions have difficulties to enter small pores of CDC films. No distortion was observed for smaller $BF_4$ ions, which suggests the pores even at the lowest synthesis temperature were close to 0.6 – 0.7 nm that is larger than $BF_4$ ions.

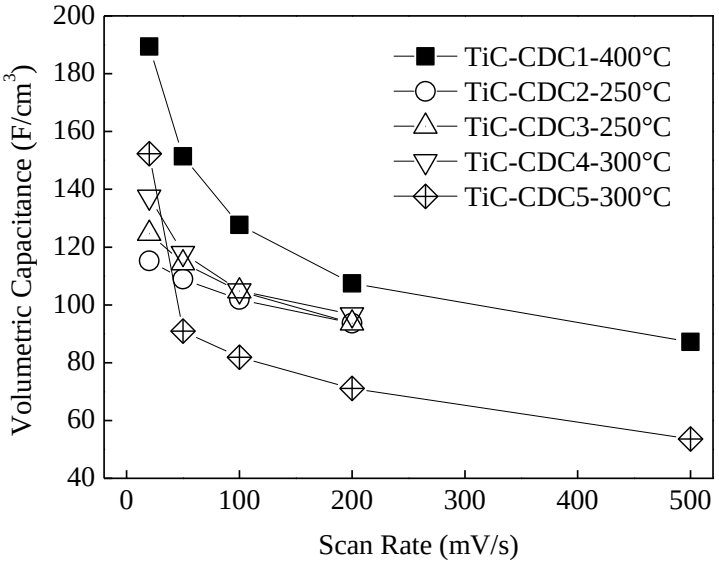


Figure 4.25: Volumetric Capacitance vs. scan rate for TiC-CDC films synthesized at 250, 300, and 400 °C.

Galvanostatic cycling test was conducted using TiC-CDC film synthesized at 300 °C. It maintained 97% of initial capacitance over 1000 cycles.

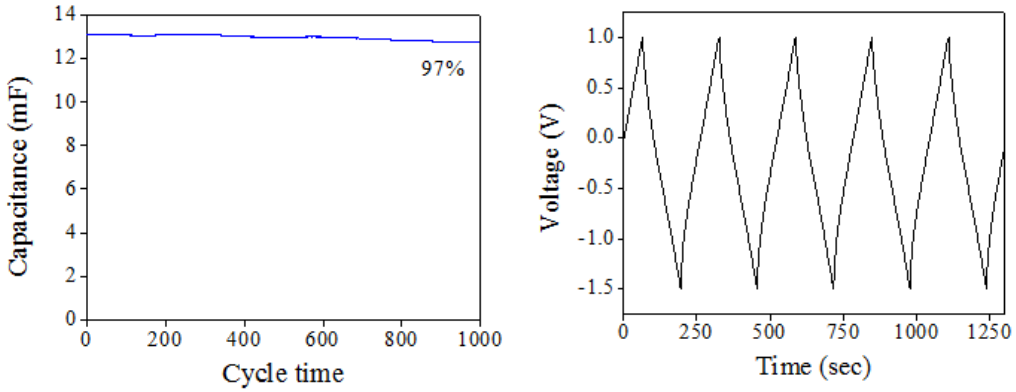


Figure 4.26: Galvanostatic cycling charge/discharge of TiC-CDC films on glassy carbon.

### 4.3.6. Patterning TiC-CDC Films

Focused ion beam (FIB), Laser micro-machining (using Excimer laser; KrF and ArF), and reactive ion etching (RIE) processes were tested and developed for fabrication of interdigitated electrodes on CDC films. The feasibility of this process for patterning and fabrication of micro-devices on a chip was investigated. It was found that conventional photolithography and Reactive Ion Etching (RIE) using $SF_6$ as etching gas is a more facile way of patterning CDC films on substrates.

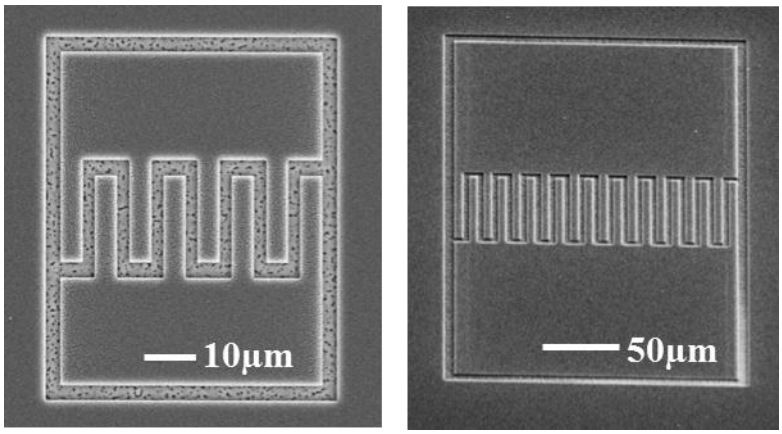


Figure 4.27: Patterned TiC-CDC films on silicon oxide wafer by FIB.

FIB can produce a precise micron scale pattern by gallium ion milling. High energy Ga ion bombards the CDC surface to remove carbon. Using secondary electron and secondary ion imaging, whole milling process is monitored. However ion milling is a very slow process, a size of 150 × 300 $\mu m^2$, 2 μm-deep interdigitated electrodes pattern takes more than 2 h.

Secondly laser ablation technique using KrF (248 nm), ArF (193 nm) pulsed excimer lasers were used for micromachining of electrode patterns. It is very fast process due to the simple mechanism of burning materials in the air with a high energy pulse laser. For direct machining, minimum laser spot size is ~10 μm. Therefore for precise patterning with sharp edges on CDC films, it requires to use mask and projection optics. Pulse laser was tested on Au-deposited TiC-CDC films on silicon oxide wafers and it was found that even minimum number of laser pulses were more than enough to pattern the CDC films and after ablation, roughness is very high at pattern edges.

Lastly, reactive ion etch was tested. It accompanied with lithographic microfabrication process which is a conventional Si fabrication technique. It was shown

that carbon films could be patterned well by RIE using oxygen plasma. Therefore, patterning thin film electrodes was carried out by RIE.

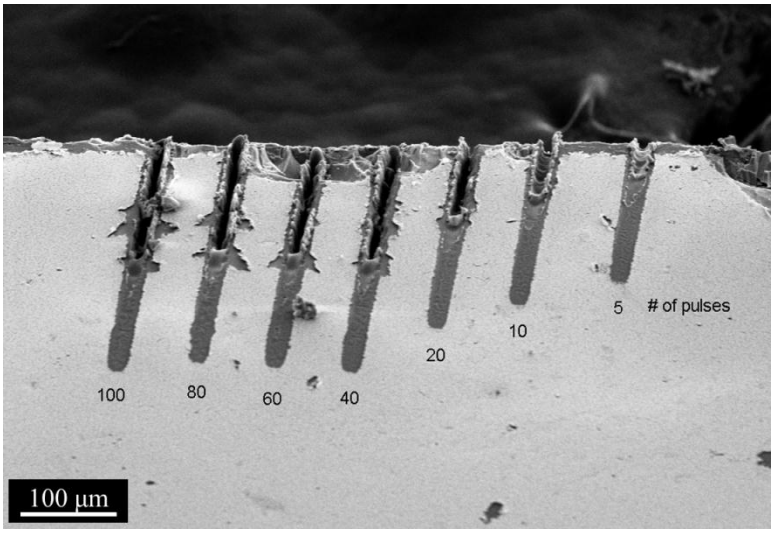


Figure 4.28: Laser ablation tests on Au-coated TiC-CDC films.

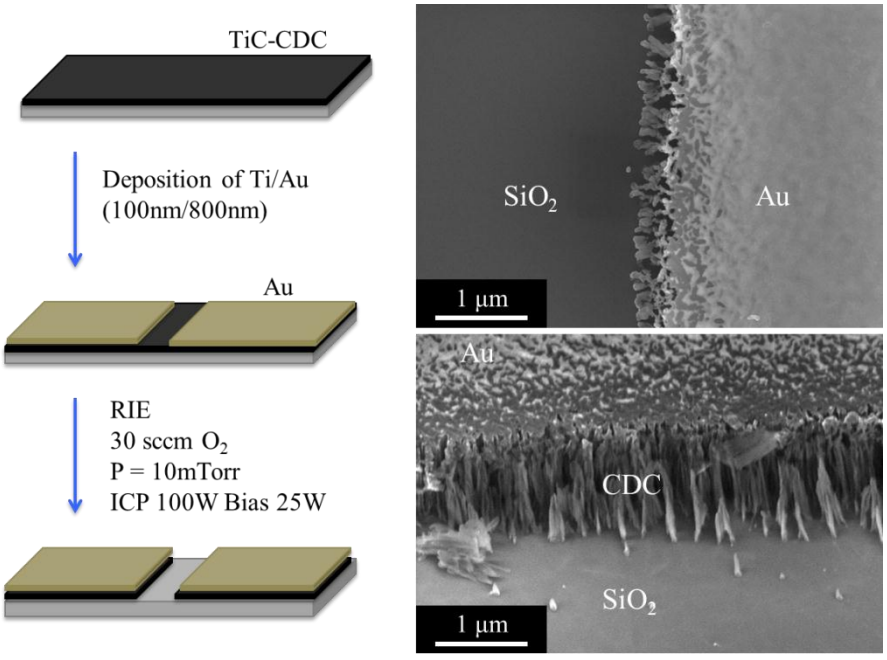


Figure 4.29: Reactive Ion Etching on TiC-CDC films with Ti 100 nm/Au 800 nm.

## 4.4. In Situ AFM Study on CDC Films

### 4.4.1. In Situ AFM technique

For supercapacitors, balancing between high energy density, high power handling ability, and a very long cycle lifetime requires a fundamental understanding of the mechanisms of electrochemical energy storage. This includes factors that limit capacitance, rate handling, and chemical, mechanical stability which are beyond the scope of classical electrochemical measurements. During the charge and discharge of EDLCs, there is significant expansion and contraction caused by ion movement into and out of pores in the electrode material. This strain development in EDLCs has been studied by couple of research groups.[118-120] For ideal supercapacitors, the strain level was expected to be smaller than that of Li-ion batteries due to the absence of ion intercalation. However, recent studies have found that during the charge and discharge of EDLCs, carbon electrodes show significant expansion and contraction.[118, 119, 121]

By using electrochemical dilatometry, the Kötz group has systematically studied the height change of various carbon electrodes such as activated carbon, carbon black and carbon cloth in tetraethylammonium-tetrafluoroborate [$TEABF_4$] in acetonitrile and propylene carbonate.[121] It was found that reversible electrode expansion was on the order of 1% for activated carbon electrodes and ascribed it to insertion and intercalation processes. Fully reversible expansion on the order of 2 % in TEA-$BF_4$ in acetonitrile was reported for microporous CDC powder-based electrodes.[119]

Electrochemical dilatometry offers a convenient way to measure bias-induced strain during an electrochemical experiment such as cyclic voltammetry.[122] In general, the accuracy of a displacement transducer of electrochemical dilatometry has been reported

to be on the order of 60 nm.[119] This might have been sufficient for measurement of macroscopic expansion, however it is not applicable for strain studies on the textured or patterned electrode material of micro-supercapacitors.

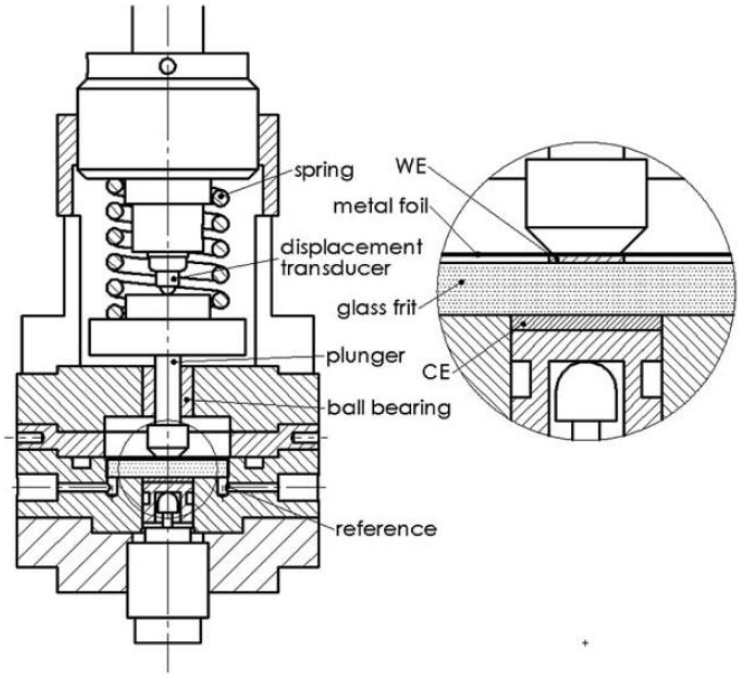


Figure 4.30: Cross-sectional view of the dilatometer. The working electrode (WE) is positioned on top of a glass frit that is fixed in position. Any height change of the WE is transmitted through a metal foil (serving also as an electrolyte sealing) and a moveable plunger to a displacement transducer. A constant load can be applied by spring.[121]

To overcome the limitation of electrochemical dilatometry, in situ atomic force microscopy (AFM) was employed to study the expansion of CDC films during EDLC operation cycles. This method has already been successfully used to investigated Li-ion battery electrodes.[123] However, its applicability to investigating EDLC electrode materials with a much smaller dimensional changes during operation has not been

demonstrated yet. Along the z-direction, this in situ AFM technique provides a deformation/strain resolution of roughly 10's to 100's of picometers in static AFM mode which is 2-3 orders of magnitude higher than electrochemical dilatometry.[124] The lateral resolution is determined by the tip radius and is typically around 20 – 30 nm which enables high spatial resolution. In situ AFM methods, in other words 'strain spectroscopy', provide the way of investigating the electrochemical expansion of EDLC electrodes on the order of individual structural elements in nanoscale. The understanding of electrode swelling with regard to device failure is especially important as EDLCs device designs becomes more sophisticated depending on applications and other components of EDLC systems. With the unique combination of electrochemical information and the expansion behavior of electrodes, it can provide more fundamental insight to the relationship between structure and functions and understanding of charge/discharge processes, compared to conventional electrochemical dilatometry.

### 4.4.2. In Situ AFM study on TiC-CDC films

A commercial in situ electrochemical AFM cell from Asylum Research was used for the experiment. The cell has a planar design to enable AFM access to the working electrode from the top. A CDC film synthesized by chlorination of TiC thin film at 450 °C for 10 minutes was used for experiment. A carbon cloth (Panex 30 carbon cloth, Zoltek Inc., USA) with the total surface area larger than the working electrode was used as an oversized counter electrode. A room temperature ionic liquid (RTIL) electrolyte (1-butyl-3methyl-imidazolium bis(trifluoromethanesulfonyl)imide (Bmim[$Tf_2N$]) with 1M Li[$Tf_2N$] was used to prevent electrolyte evaporation during testing. Electrochemical characterization was conducted by a Bio-Logic SP-200 potentiostat/galvanostat in the 2-

electrode setup without reference electrode. For EIS, internal frequency response analyzer with a single sine amplitude of 10 mV over 10 mHz to 100 kHz range. Surface displacement was measured by keeping the AFM tip in contact with the top of CDC film with a constant contact force at a fixed location during charge and discharge.

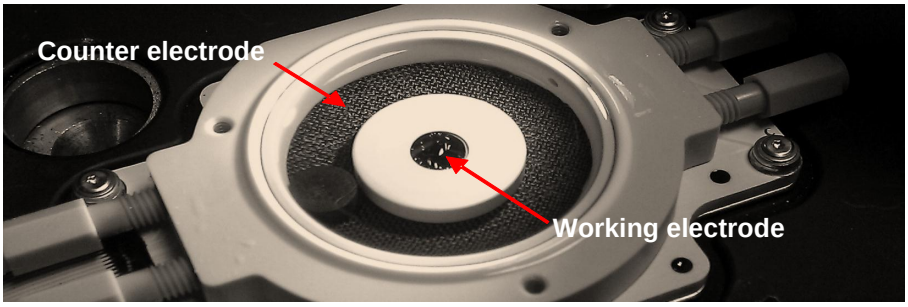


Figure 4.31: Photograph of the in situ electrochemical AFM cell.[124]

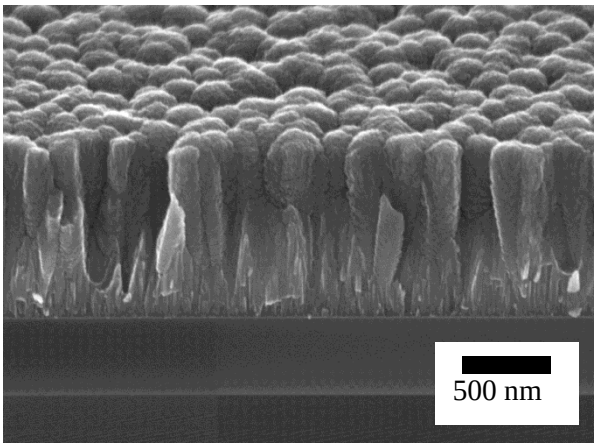


Figure 4.32: SEM micrograph of a TiC-CDC film.

On the TiC-CDC film, the lateral grain morphology was semi-spherical with an average grain size of 200-300 nm with RMS roughness of about 20 nm which is in good agreement with the AFM result in Fig. 4.33 (a). Also it was noted that the axial texture of the columnar grains of CDC extends along the entire height of the film.

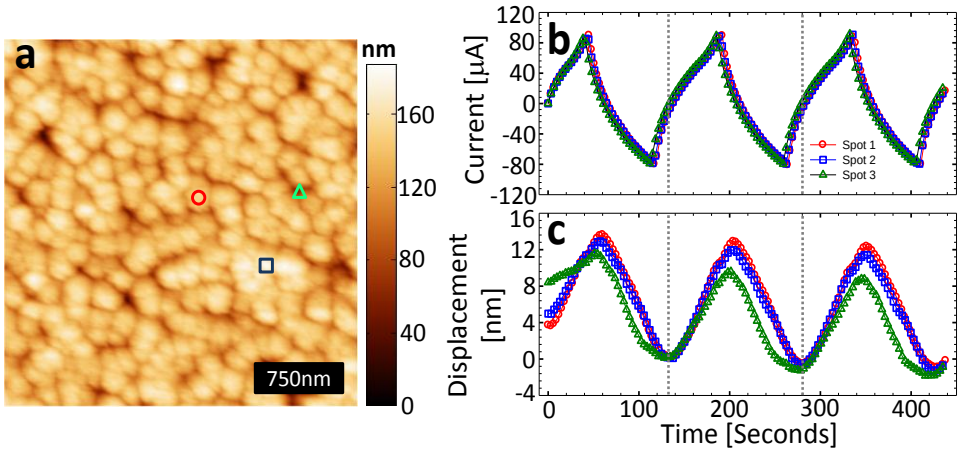


Figure 4.33: (a) AFM topography (3 μm × 3 μm) of the CDC surface in RTIL, the marks indicate the surface locations that correspond to the charge/discharge/strain cycles in (b) and (c), (b) cyclic voltammogram at 50 mV/s with a voltage range from -1.5 V to 2.15 V for each of the three different locations in (a) and, (c) strain response measured during the cyclic voltammetry tests.[124]

The AFM topography of the TiC-CDC film measured in RTIL is shown above. Note the topography is a convolution of the tip shape and the actual sample topography. Fig. 4.33 (b), (c) shows the surface height change for three different locations on the TiC-CDC film surface during charge and discharge.

It was noted that: (1) the displacement in the CDC film at 50 mV/s is on the order of 15 nm over the course of the cycle, which is a factor of four smaller than the resolution limit of the typical Electrochemical Dilatometry transducer and would not be observable

by ordinary Electrochemical Dilatometry tools, (2) there is a phase lag between the charge and discharge current and the strain response, and (3) Subtle variations in strain are observed as a function of spatial location, indicating that strain response exhibits spatial variability.

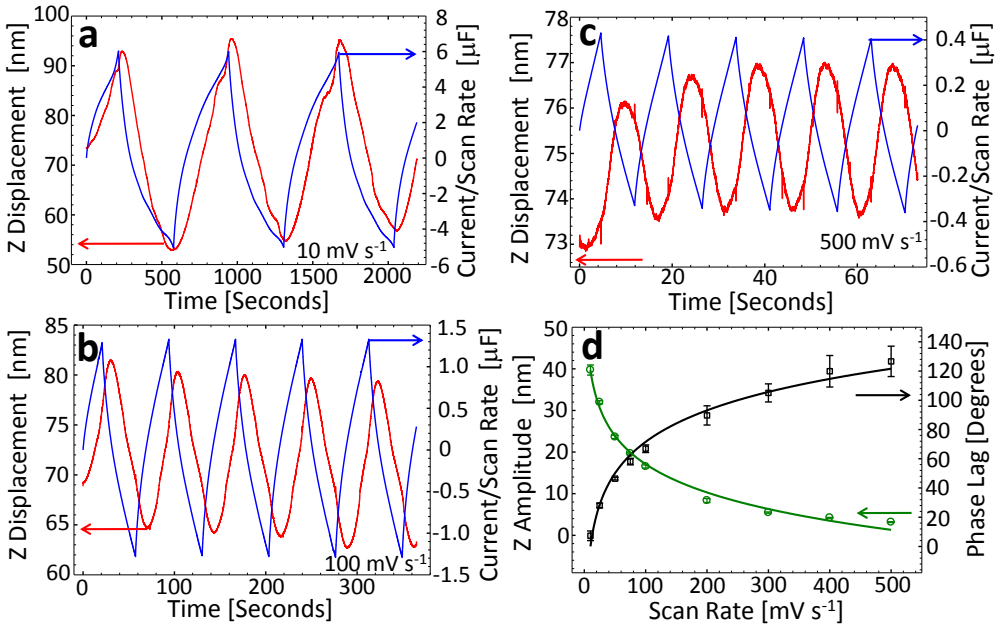


Figure 4.34: Cyclic voltammograms and sample surface displacement curves for scan rates of (a) 10 mV/s, (b) 100 mV/s, (c) 500 mV/s and (d) a graph of displacement as a function of scan rate.[124]

The height change of a fixed spot was measured using different scan rate from 50 mV/s to 500 mV/s. Significant displacement is observed over all the scan rates, however the magnitude of the strain decreases with increasing scan rate. This behavior is similar to the reduced capacitance at higher scan rates which is likely the result of incomplete charging of the capacitor. Also, a phase lag becomes larger as scan rates goes higher.

The displacement-time curves at slow scan rates (~10 mV/s and below) show some fine structure. It was found that this is the result of the lateral sample expansion which is more pronounced at slow charging rates and was found to be reproducible. Interestingly, the strain response and phase lag experience an inversely proportional relationship where slow scan rates result in large strain and very little phase lag, while fast scan rates produce little strain but large phase shift. The phase lag between the current and the displacement suggests that there are two different mechanisms involved in capacitance and the volume changes.

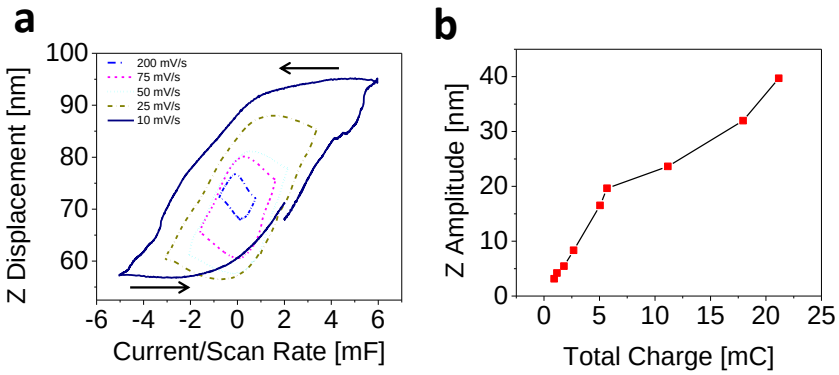


Figure 4.35: (a) Displacement versus cell capacity (current/scan rate) at various scan rates and (b) correlation between the total charge and the maximum surface displacement.

It was observed that a monotonically increasing dependence between the maximum displacement and the charge from the plot in Fig. 4.35. This suggests that the displacement response scales accordingly with the degree of charging of the capacitor which implies that the processes responsible for inducing strain and storing a charge are highly correlated.

To explain the observed behavior, two charge-induced strain mechanisms were discussed. First is pore swelling, which was described by Hantel et al. and second is ion insertion into the pores of CDC films.[119] For the ion insertion, theoretically it can be achieved either by RTIL ions or the added Li-ions in the RTIL. However, TiC-CDC film produced at 450 °C is mostly amorphous without graphitic structure.[85] Since there was no redox materials in the cell but the nanoporous CDC film used as a working electrode, the pore filling effect is expected to be the dominant process.

These experimental findings are in accordance with works reported recently on the ion transport dynamics in porous EDLC electrodes.[125-128] It is expected that the comparison of experimental result based on nanoscale in situ electrochemical AFM with predictive modeling will allow us to understand better about ion transport and diffusion within the electric double layer and into the pores of the carbon electrodes.

## 4.5. Micro-Supercapacitors using TiC-CDC film electrodes

It was demonstrated that continuous CDC films can be synthesized on a variety of substrates and performs well as a EDLC electrode material in sandwich configurations. However micro power supply applications such as the one for MEMS system require micro-supercapacitors integrated as an on-chip planar interdigitated electrode configuration without polymer separator or binders.

By utilizing TiC-CDC films, micro-supercapacitors with interdigitated configuration were fabricated using conventional micro-fabrication techniques: sputtering of TiC films, photolithography and reactive ion etching (RIE) of TiC to create an interdigitated pattern,

chlorination of TiC to transform the carbide into highly porous TiC-CDC, which is the active material of the micro-supercapacitor, and metallic current collectors (Ti/Au or Al) deposition through a corresponding patterned shadow mask

### 4.5.1. Fabrication of Micro-Supercapacitor

TiC films were deposited on Si wafers with 500 nm thermal $SiO_2$ layer by reactive DC magnetron sputtering where titanium target and acetylene ($C_2H_2$) gas were used. On TiC film, photoresist film was coated and the interdigitated electrodes was patterned onto the photoresist film using photolithography. Then by Reactive Ion Etching (RIE) using $SF_6$ as etching gas, the interdigitated electrode pattern was transferred to TiC film. Afterwards, the electrode-patterned TiC films were etched by chlorine gas at 450 °C to convert it to TiC-CDC films.

The Ti/Au current collectors, with thickness of 100 nm/400 nm respectively, were evaporated onto the pattern through a designed shadow mask with narrower electrode fingers, to allow for electrolyte percolation during electrochemical characterization. The deposited current collectors were annealed at 250 °C for 20 minutes under vacuum in order to improve the metal conductivity and release the mechanical stress between the Ti/Au and the TiC-CDC layers. Other samples with a different current collector (Al of 400 nm thickness) were implemented in similar devices using the procedures described above except annealing.

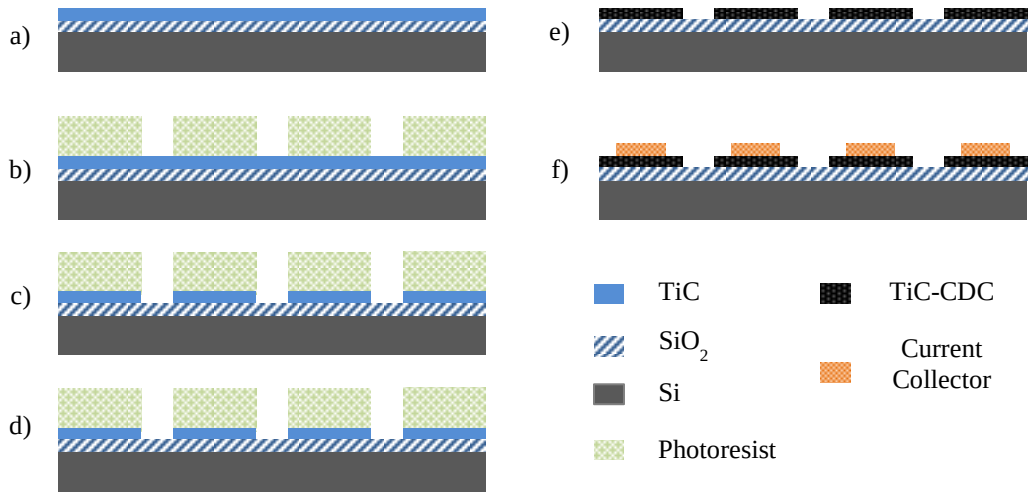


Figure 4.36: Schematic illustration of the fabrication process for micro-supercapacitors: a) As-received Si/$SiO_2$/TiC wafer; b) Photolithography; c) Reactive Ion Etching (RIE); d) Removal of photoresist by acetone and chromosulfuric acid; e) Chlorination; f) Current collector deposition.[37]

The electrode design of the micro-supercapacitor is 2x4 interdigitated fingers with a finger length of 6.35 mm, a finger width of 0.8 mm and 0.15 mm spacing between fingers, which makes a footprint area of 8.1 x 6.4 $mm^2$. The surface area of a single patterned electrode is 0.26 $cm^2$, and 6.2 mm long current collectors were evaporated through a hard mask with a width of 0.5 mm. The area of current collector deposited onto a single electrode was 0.16 $cm^2$, which is smaller than the electrode footprint of 0.26 $cm^2$.

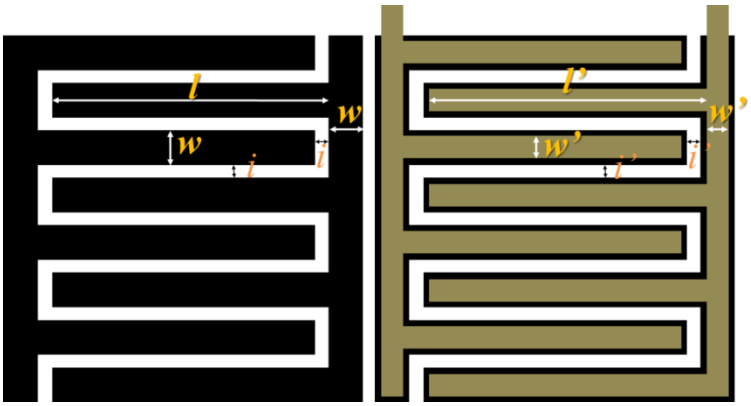


Figure 4.37: a) The design of the interdigitated electrode pattern of TiC-CDC; b) The design of the hard mask used for metal current collectors.[37]

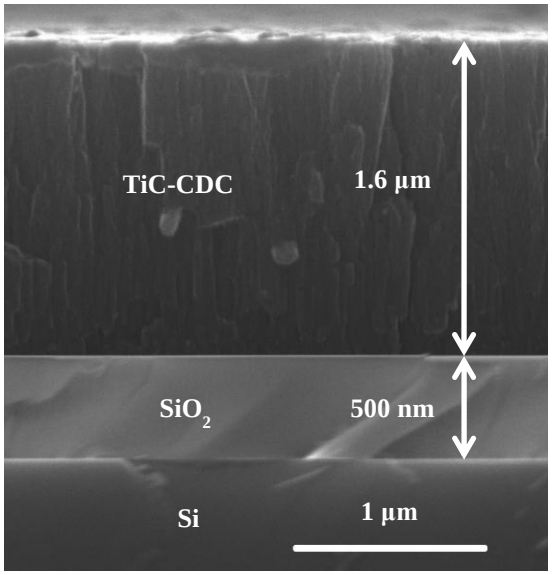


Figure 4.38: The cross-section of TiC-CDC film based micro-supercapacitor electrode.

The thickness of the TiC-CDC film was 1.6 µm measured by SEM cross-section. The TiC-CDC films adhered well to the Si substrate and had conformal columnar structure of textured TiC film maintained even though no Ti content left in the film.

### 4.5.2. Electrochemical Characterization

Electrochemical characterization of the TiC-CDC film based micro-supercapacitors was conducted at University Paul Sabatier in Toulouse, France. The TiC-CDC film based micro-supercapacitors were wired with a connector and immersed into the 1M $NEt_4BF_4$ in propylene carbonate (PC) in Ar atmosphere within a glove box where the $H_2O$ and $O_2$ level was lower than 0.1 ppm. Cyclic voltammetry (CV) and Electrochemical Impedance Spectroscopy (EIS) were performed using Bio-Logic VMP2 potentiostat.

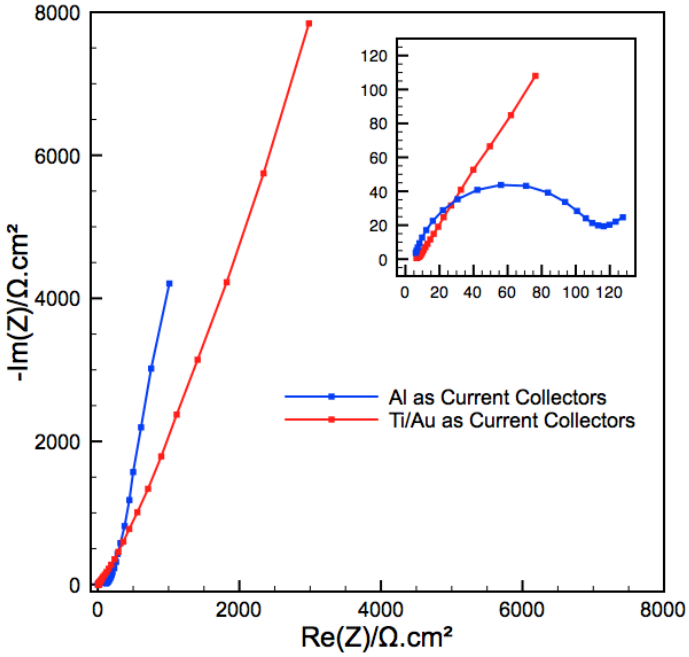


Figure 4.39: Nyquist plot of the TiC-CDC film based micro-supercapacitor with, (a) Ti/Au current collectors and, (b) Al current collectors in 1M $NEt_4BF_4$ in PC.[37]

The Nyquist plot of the micro-supercapacitor with Ti/Au current collector shows a capacitive characteristic without redox reaction.[129] It doesn't show a curvature at the middle frequency range, which means a good contact at the interface between Ti/Au current collector and CDC electrodes.[130] However, the slope of the plot deviated from 90 degree of pure double layer behavior shows that possible redox reaction of impurities. The Nyquist plot of the micro-supercapacitor with Al current collector shows steeper curve at low frequencies indicating better capacitive behavior compared to the micro-supercapacitor with Ti/Au current collector, but also shows a loop at high frequencies which is due to higher contact resistance at the interface between Al and CDC film electrodes. It was resulted from the oxidation of Al during current collector deposition process.[131]

The equivalent series resistance (ESR) of the TiC-CDC film based micro-supercapacitors is 6.6 $\Omega cm^2$ for Ti/Au current collector and 6.0 $\Omega cm^2$ for Al current collector. Because of the device size being very small, the measured ESR was as high as 23 - 25 Ω. The ESR is comparable to the one from the micro-supercapacitors made by electrophoretic deposition, ~3 $\Omega cm^2$.[47]

The cyclic voltammetry was conducted at various scan rates with the TiC-CDC films based micro-supercapacitors immersed in 1 M $NEt_4BF_4$ in PC electrolyte. The CV at scan rate of 100 mV/s shows a rectangular shape of typical capacitive behavior over the 2V window with a little bit of distortion at high voltage due to redox reaction by impurities which was observed by EIS. The micro-supercapacitor has a capacitance of 0.74 mF at the scan rate of 100 mV/s, or a specific capacitance of 1.4 $mF/cm^2$.

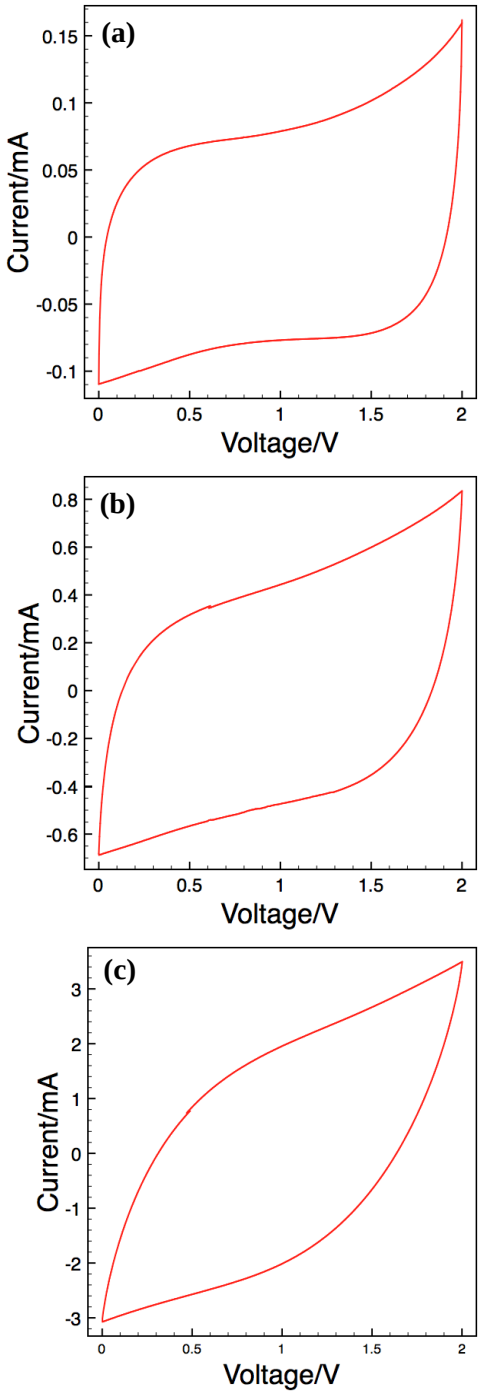


Figure 4.40: Cyclic voltammograms of the TiC-CDC film based micro-supercapacitor with Ti/Au current collectors in 1M $NEt_4BF_4$ in PC at scan rates of (a) 100 mV/s, (b) 1 V/s and (c) 10 V/s.[37]

More importantly, the micro-supercapacitor demonstrated capacitive characteristic even at a scan rate of 10 V/s, which is exceptionally high as micro-supercapacitors. The high scan rate operation of the device suggests that the electric charge storage is governed by ion sorption at the surface of CDC film electrodes, not by ion transport from the electrolyte to the surface of electrodes.

From a device point of view, the fabricated TiC-CDC film based micro-supercapacitor showed maximum specific energy of 3.0 $mJ/cm^2$ and maximum specific power of 84 $mW/cm^2$, which are comparable among the carbon-based micro-supercapacitors reported.[132, 133]

This study proved that CDC film process can be incorporated into the conventional microfabrication processes to produce on-chip micro-supercapacitors, which is the biggest advantage of utilizing CDC film electrodes. To enhance the energy density and power delivery, there are many factors to be considered and optimized, such as matching CDC film's average pore size to the electrolyte ion size, how to avoid impurity intrusion throughout the fabrication process, more importantly the pattern design and dimensions of interdigitated CDC film electrodes, the different layered structure (for example, CDC film electrodes on top of current collector) and so on.

# 5. CONCLUSIONS AND FUTURE WORK

Nanoporous continuous carbide-derived carbon films were synthesized by chlorine gas etching of sputtered TiC films on various substrates in the temperature range from 250 °C to 600 °C, and by vacuum decomposition of SiC single crystal wafers in the temperature range from 1500 °C to 1900 °C. TiC-CDC films show capacitance of up to 180 $F \cdot cm^{-3}$ at 20 $mV \cdot s^{-1}$ scan rate in 1M $TEABF_4$/acetonitrile, which is the highest one reported for porous disordered carbons.

Properties and morphology of TiC-CDC film were greatly affected by the composition and morphology of the sputtered TiC film as well as chlorine gas etching conditions. Micro-cracks, which can be considered as macropores, develop because of tensile stresses in the CDC caused by the carbide-carbon transformation, and their orientation is controlled by the columnar structure of the TiC film. Less cracks was observed in TiC-CDC films synthesized at lower chlorine etching temperature.

Micro-supercapacitors using TiC-CDC film were fabricated via conventional micro-fabrication techniques and were characterized by electrochemical impedance spectroscopy and cyclic voltammetry. Micro-supercapacitors with TiC-CDC film electrodes showed good performance as double layer capacitors with a specific energy of 3.0 $mJ/cm^2$, and specific power of 84 $mW/cm^2$ on an 8-finger electrodes device. Integration of on-chip micro-supercapacitors onto a Si wafer was demonstrated successfully.

Nanoscale electrochemical dilatometry using AFM was carried out to study CDC film electrodes. It separates individual stages in charge/discharge processes based on strain generation due to ion insertion into the carbon micropores. Two distinct modes of the charging process for CDC films were identified, one is fast charging of the double layer in macropores/cracks and on the external film surface, unassociated with strain, and another much slower mass transport related to ion insertion into micropores and leading to a significant volume change of CDC film electrodes.

Future work on the CDC films and micro-supercapacitor should include a systematic study on micro-supercapacitor design for realistic integrated energy storage on a chip. Not only the dimensions and the form factor, but also material selection and process integration are important. To find a solid state electrolyte that suits microfabrication in vacuum and also has ions matching the carbon film pore size, would be crucial to creating reliable high-performance micro-supercapacitors.

For CDC film electrodes, there is still much to explore. Since vacuum processing is well suited for manufacturing nanoporous CDC films, a further study on rapid thermal treatment to modify the properties of CDC films would help to improve micro-supercapacitor performance. Deposition of transition metal oxide films onto the CDC films would be interesting as well. As seen from our in-situ AFM study on CDC films, CDC film can withstand volume change very well while charging/discharging. RTA-treated mesoporous CDC films could be used as a highly conducting backbone electrode for thin-film pseudocapacitor.

## 6. LIST OF REFERENCES

1. B. E. Conway, *Electrochemical supercapacitors: scientific fundamentals and technological applications*, Kluwer Academic/Plenum, New York, 1999.

2. J. R. Miller and P. Simon, *Electrochem. Soc. Interface*, 2008, 17, 31-32.

3. J. R. Miller and P. Simon, *Science*, 2008, 321, 651-652.

4. M. Endo, Y. J. Kim, T. Takeda, T. Maeda, T. Hayashi, K. Koshiba, H. Hara and M. S. Dresselhaus, *Journal of the Electrochemical Society*, 2001, 148, A1135-A1140.

5. M. Endo, T. Takeda, Y. J. Kim, K. Koshiba and K. Ishii, *Carbon Science*, 2001, 1, 117-128.

6. A. Halama, B. Szubzda and G. Pasciak, *Electrochimica Acta*, 2010, 55, 7501-7505.

7. K.-L. Yang, S. Yiacoumi and C. Tsouris, *Journal of Electroanalytical Chemistry*, 2003, 540, 159-167.

8. R. Saliger, U. Fischer, C. Herta and J. Fricke, *Journal of Non-Crystalline Solids*, 1998, 225, 81-85.

9. J. M. Miller, B. Dunn, T. D. Tran and R. W. Pekala, *Journal of the Electrochemical Society*, 1997, 144, L309-L311.

10. T. Bordjiba, M. Mohamedi and L. H. Dao, *Journal of Power Sources*, 2007, 172, 991-998.

11. J. N. Barisci, G. G. Wallace, D. R. MacFarlane and R. H. Baughman, *Electrochemistry Communications*, 2004, 6, 22-27.

12. C. Emmenegger, P. Mauron, P. Sudan, P. Wenger, V. Hermann, R. Gallay and A. Züttel, *Journal of Power Sources*, 2003, 124, 321-329.

13. J. H. Chen, W. Z. Li, D. Z. Wang, S. X. Yang, J. G. Wen and Z. F. Ren, *Carbon*, 2002, 40, 1193-1197.

14. T. Kyotani, J. Chmiola and Y. Gogotsi, in *Carbons for Electrochemical Energy Storage and Conversion Systems*, eds. F. Béguin and E. Frackowiak, CRC Press, Boca Raton, 2008, pp. 77-114.

15. C. Vix-Guterl, E. Frackowiak, K. Jurewicz, M. Friebe, J. Parmentier and F. Béguin, *Carbon*, 2005, 43, 1293-1302.

16. A. B. Fuertes, F. Pico and J. M. Rojo, *Journal of Power Sources*, 2004, 133, 329-336.

17. J. Chmiola, C. Largeot, P.-L. Taberna, P. Simon and Y. Gogotsi, *Science*, 2010, 328, 480-483.

18. B. E. Conway and W. G. Pell, *Journal of Solid State Electrochemistry*, 2003, 7, 637-644.

19. E. Frackowiak, *Physical Chemistry Chemical Physics*, 2007, 9, 1774-1785.

20. A. G. Pandolfo and A. F. Hollenkamp, *Journal of Power Sources*, 2006, 157, 11-27.

21. J. Ho, T. R. Jow and S. Boggs, *Electrical Insulation Magazine, IEEE*, 2010, 26, 20-25.

22. *US Pat.*, 2,800,616, 1957.

23. *US Pat.*, 3,288,641, 1966.

24. *US Pat.*, 3,536,963, 1970.

25. U. D. o. Energy, *Basic Research Needs for Electrical Energy Storage: Report of the Basic Energy Sciences Workshop on Electrical Energy Storage*, 2007.

26. D. Tuite, in *Electronic Design*, Penton Publishing, 2007, vol. 55, ch. 45, pp. 45-51.

27. F. Béguin and E. Frackowiak, *Carbons for Electrochemical Energy Storage and Conversion Systems*, CRC Press, 2010.

28. F. Belhachemi, S. Rael and B. Davat, 2000.

29. L. L. Zhang and X. S. Zhao, *Chemical Society Reviews*, 2009, 38, 2520-2531.

30. G.-L. Gouy, *Journal de Physique*, 1910, 9, 457-468.

31. D. L. Chapman, *Philosophical Magazine Series 6*, 1913, 25, 475 - 481.

32. O. Stern, *Zeitschrift fuer Elektrochemie und Angewandte Physikalische Chemie*, 1924, 30, 508-516.

33. P. Simon and Y. Gogotsi, *Nat Mater*, 2008, 7, 845-854.

34. A. Lewandowski, A. Olejniczak, M. Galinski and I. Stepniak, *Journal of Power Sources*, 2010, 195, 5814-5819.

35. P. Simon and Y. Gogotsi, *Philosophical Transactions of the Royal Society A: Mathematical,Physical and Engineering Sciences*, 2010, 368, 3457-3467.

36. M. Beidaghi and Y. Gogotsi, *Energy & Environmental Science*, 2014, 7, 867-884.

37. P. Huang, M. Heon, D. Pech, M. Brunet, P.-L. Taberna, Y. Gogotsi, S. Lofland, J. D. Hettinger and P. Simon, *Journal of Power Sources*, 2013, 225, 240-244.

38. Y. S. Yoon, W. I. Cho, J. H. Lim and D. J. Choi, *Journal of Power Sources*, 2001, 101, 126-129.

39. H. J. In, S. Kumar, Y. Shao-Horn and G. Barbastathis, *Applied Physics Letters*, 2006, 88, 083104-083103.

40. C. C. Ho, D. A. Steingart, J. P. Salminen, W. H. Sin, T. M. K. Rantala, J. W. Evans and P. K. Wright, *PowerMEMS 2006. Sixth International Workshop on Micro and Nanotechnology for Power Generation and Energy Conversion Applications*, 2006, 219-222.

41. Y. Honda, T. Haramoto, M. Takeshige, H. Shiozaki, T. Kitamura and M. Ishikawa, *Electrochemical and Solid-State Letters*, 2007, 10, A106-A110.

42. J. J. Yoo, K. Balakrishnan, J. Huang, V. Meunier, B. G. Sumpter, A. Srivastava, M. Conway, A. L. M. Reddy, J. Yu, R. Vajtai and P. M. Ajayan, *Nano Letters*, 2011, 11, 1423-1427.

43. J. R. Miller, R. A. Outlaw and B. C. Holloway, *Electrochimica Acta*, 2011, 56, 10443-10449.

44. J. R. Miller, R. A. Outlaw and B. C. Holloway, *Science*, 2010, 329, 1637-1639.

45. S. W. Lee, B. M. Gallant, H. R. Byon, P. T. Hammond and Y. Shao-Horn, *Energy & Environmental Science*, 2011, 4, 1972-1985.

46. D. Pech, M. Brunet, P. L. Taberna, P. Simon, N. Fabre, F. Mesnilgrente, V. Conedera and H. Durou, *Journal of Power Sources*, 2010, 195, 1266-1269.

47. D. Pech, M. Brunet, H. Durou, P. Huang, V. Mochalin, Y. Gogotsi, P.-L. Taberna and P. Simon, *Nat Nano*, 2010, 5, 651-654.

48. D. Chunsheng and P. Ning, *Nanotechnology*, 2006, 17, 5314.

49. S. J. An, Y. Zhu, S. H. Lee, M. D. Stoller, T. Emilsson, S. Park, A. Velamakanni, J. An and R. S. Ruoff, *The Journal of Physical Chemistry Letters*, 2010, 1, 1259-1263.

50. W. Yan, J. Y. Kim, W. Xing, K. C. Donavan, T. Ayvazian and R. M. Penner, *Chemistry of Materials*, 2012, 24, 2382-2390.

51. J. Duay, E. Gillette, R. Liu and S. B. Lee, *Physical Chemistry Chemical Physics*, 2012, 14, 3329-3337.

52. M. Beidaghi and C. Wang, *Electrochimica Acta*, 2011, 56, 9508-9514.

53. V. Presser, M. Heon and Y. Gogotsi, *Advanced Functional Materials*, 2011, 21, 800-800.

54. *Great Britain Pat.*, 971943, 1964.

55. Y. Gogotsi, A. Nikitin, H. H. Ye, W. Zhou, J. E. Fischer, Y. Bo, H. C. Foley and M. W. Barsoum, *Nature Materials*, 2003, 2, 591-594.

56. A. Janes, L. Permann, M. Arulepp and E. Lust, *Electrochemistry Communications*, 2004, 6, 313-318.

57. *US Pat.*, 1271713, 1918.

58. W. C. Schumb and J. R. Aronson, *Journal of the American Chemical Society*, 1959, 81, 806-807.

59. N. Batisse, K. Guérin, M. Dubois, A. Hamwi, L. Spinelle and E. Tomasella, *Thin Solid Films*, 2010, 518, 6746-6751.

60. N. Batisse, K. Guérin, M. Dubois and A. Hamwi, *Carbon*, 2011, 49, 2998-3009.

61. A. K. Kuriakose and J. L. Margrave, *The Journal of Physical Chemistry*, 1964, 68, 2343-2345.

62. G. N. Yushin, E. N. Hoffman, A. Nikitin, H. H. Ye, M. W. Barsoum and Y. Gogotsi, *Carbon*, 2005, 43, 2075-2082.

63. H. L. Wang and Q. M. Gao, *Carbon*, 2009, 47, 820-828.

64. Z. G. Cambaz, G. N. Yushin, Y. Gogotsi, K. L. Vyshnyakova and L. N. Pereselentseva, *Journal of the American Ceramic Society*, 2006, 89, 509-514.

65. L. Chen, H. Ye, Y. Gogotsi and M. J. McNallan, *Journal of the American Ceramic Society*, 2003, 86, 1830-1837.

66. E. N. Hoffman, G. Yushin, M. W. Barsoum and Y. Gogotsi, *Chemistry of Materials*, 2005, 17, 2317-2322.

67. E. N. Hoffman, G. Yushin, B. G. Wendler, M. W. Barsoum and Y. Gogotsi, *Materials Chemistry and Physics*, 2008, 112, 587-591.

68. R. K. Dash, G. Yushin and Y. Gogotsi, *Microporous and Mesoporous Materials*, 2005, 86, 50-57.

69. R. K. Dash, A. Nikitin and Y. Gogotsi, *Microporous and Mesoporous Materials*, 2004, 72, 203-208.

70. T. Y. Kosolapova, *Carbides. Properties, Production, and Applications*, Plenum Press, New York - London, 1971.

71. G. Busch, *The Electrical Conductivity of Silicon Carbide*, E. Birkhäuser, 1946.

72. D. V. Badami, *Nature*, 1962, 193, 569-570.

73. F. Meyer and G. J. Loyen, *Acta Electronica*, 1975, 18, 33-38.

74. M. Kusunoki, M. Rokkaku and T. Suzuki, *Applied Physics Letters*, 1997, 71, 2620-2622.

75. M. Kusunoki, J. Shibata, M. Rokkaku and T. Hirayama, *Japanese Journal of Applied Physics Part 2-Letters & Express Letters*, 1998, 37, L605-L606.

76. M. Kusunoki, T. Suzuki, K. Kaneko and M. Ito, *Philosophical Magazine Letters*, 1999, 79, 153-161.

77. M. Kusunoki, T. Suzuki, T. Hirayama, N. Shibata and K. Kaneko, *Applied Physics Letters*, 2000, 77, 531-533.

78. M. Kusunoki, T. Suzuki, C. Honjo, T. Hirayama and N. Shibata, *Chemical Physics Letters*, 2002, 366, 458-462.

79. M. Kusunoki, T. Suzuki, T. Hirayama and N. Shibata, *Physica B: Condensed Matter*, 2002, 323, 296-298.

80. H. Watanabe, Y. Hisada, S. Mukainakano and N. Tanaka, *Journal of Microscopy-Oxford*, 2001, 203, 40-46.

81. Z. G. Cambaz, G. Yushin, S. Osswald, V. Mochalin and Y. Goyotsi, *Carbon*, 2008, 46, 841-849.

82. G. Yushin, A. Nikitin and Y. Gogotsi, in *Nanomaterials Handbook*, ed. Y. Gogotsi, CRC Press, Boca Raton, 2006, pp. 211-254.

83. H. P. Boehm and H. H. Warnecke, Oxford, 1975.

84. R. Dash, J. Chmiola, G. Yushin, Y. Gogotsi, G. Laudisio, J. Singer, J. Fischer and S. Kucheyev, *Carbon*, 2006, 44, 2489-2497.

85. G. Laudisio, R. K. Dash, J. P. Singer, G. Yushin, Y. Gogotsi and J. E. Fischer, *Langmuir*, 2006, 22, 8945-8950.

86. J. Leis, A. Perkson, M. Arulepp, M. Käärik and G. Svensson, *Carbon*, 2001, 39, 2043-2048.

87. A. Janes, T. Thomberg and E. Lust, *Carbon*, 2007, 45, 2717-2722.

88. S. H. Yeon, P. Reddington, Y. Gogotsi, J. E. Fischer, C. Vakifahmetoglu and P. Colombo, *Carbon*, 2010, 48, 201-210.

89. Y. Korenblit, M. Rose, E. Kockrick, L. Borchardt, A. Kvit, S. Kaskel and G. Yushin, *ACS Nano*, 2010, 4, 1337-1344.

90. S. K. Gordeev, S. A. Kukushkin, A. V. Osipov and Y. V. Pavlov, *Physics of the Solid State*, 2000, 42, 2314-2317.

91. J. C. Palmer, A. Llobet, S. H. Yeon, J. E. Fischer, Y. Shi, Y. Gogotsi and K. E. Gubbins, *Carbon*, 2010, 48, 1116-1123.

92. J. Chmiola, G. Yushin, R. K. Dash, E. N. Hoffman, J. E. Fischer, M. W. Barsoum and Y. Gogotsi, *Electrochemical and Solid-State Letters*, 2005, 8, A357-A360.

93. J. Chmiola, G. Yushin, R. Dash and Y. Gogotsi, *Journal of Power Sources*, 2006, 158, 765-772.

94. L. Permann, M. Latt, J. Leis and M. Arulepp, *Electrochimica Acta*, 2006, 51, 1274-1281.

95. J. A. Fernandez, M. Arulepp, J. Leis, F. Stoeckli and T. A. Centeno, *Electrochimica Acta*, 2008, 53, 7111-7116.

96. C. Portet, M. A. Lillo-Rodenas, A. Linares-Solano and Y. Gogotsi, *Physical Chemistry Chemical Physics*, 2009, 11, 4943-4945.

97. J. Segalini, B. Daffos, P. L. Taberna, Y. Gogotsi and P. Simon, *Electrochimica Acta*, 2010, 55, 7489-7494.

98. C. Portet, G. Yushin and Y. Gogotsi, *Journal of the Electrochemical Society*, 2008, 155, A531-A536.

99. M. Lätt, M. Käärik, L. Permann, H. Kuura, M. Arulepp and J. Leis, *Journal of Solid State Electrochemistry*, 2010, 14, 543-548.

100. T. Thomberg, A. Jänes and E. Lust, *Electrochimica Acta*, 2010, 55, 3138-3143.

101. T. Thomberg, A. Jänes and E. Lust, *Journal of Electroanalytical Chemistry*, 2009, 630, 55-62.

102. J. Chmiola, G. Yushin, Y. Gogotsi, C. Portet, P. Simon and P. L. Taberna, *Science*, 2006, 313, 1760-1763.

103. J. Chmiola, C. Largeot, P.-L. Taberna, P. Simon and Y. Gogotsi, *Angewandte Chemie International Edition*, 2008, 47, 3392-3395.

104. M. Arulepp, J. Leis, M. Latt, F. Miller, K. Rumma, E. Lust and A. F. Burke, *Journal of Power Sources*, 2006, 162, 1460-1466.

105. E. Lust, A. Jänes and M. Arulepp, *Journal of Electroanalytical Chemistry*, 2004, 562, 33-42.

106. M. Heon, S. Lofland, J. Applegate, R. Nolte, E. Cortes, J. D. Hettinger, P.-L. Taberna, P. Simon, P. Huang, M. Brunet and Y. Gogotsi, *Energy & Environmental Science*, 2011, 4, 135-138.

107. R. d. Levie, in *Advances in electrochemistry and electrochemical engineering*, eds. P. Delahay and C. W. Tobias, Interscience, New York, 1967, vol. 6, p. 329.

108. J.-F. Fauvarque and P. Simon, in *Carbons for electrochemical energy storage and conversion systems*, eds. F. Béguin and E. Frackowiak, CRC Press, 2010.

109.D. S. Bethune, C. H. Klang, M. S. de Vries, G. Gorman, R. Savoy, J. Vazquez and R. Beyers, *Nature*, 1993, 363, 605-607.

110. A. Thess, R. Lee, P. Nikolaev and H. Dai, *Science*, 1996, 273, 483.

111. R. Sen, A. Govindaraj and C. N. R. Rao, *Chemical Physics Letters*, 1997, 267, 276-280.

112. Z. F. Ren, Z. P. Huang, J. W. Xu, J. H. Wang and et al., *Science*, 1998, 282, 1105-1107.

113. H. Konishi, H. Matsuoka, N. Toyama, M. Naitoh, S. Nishigaki and M. Kusunoki, *Thin Solid Films*, 2004, 464, 295-298.

114. M. Kusunoki, C. Honjo, T. Suzuki and T. Hirayama, *Applied Physics Letters*, 2005, 87, -.

115. N. Ogasawara, W. Norimatsu, S. Irle and M. Kusunoki, *Chemical Physics Letters*, 2014, 595–596, 266-271.

116. H. Pedersen, C.-C. Lin and L. Ojamäe, *Journal of Vacuum Science & Technology A*, 2013, 31, -.

117. R. Lin, P. L. Taberna, J. Chmiola, D. Guay, Y. Gogotsi and P. Simon, *Journal of The Electrochemical Society*, 2009, 156, A7-A12.

118. M. Hahn, O. Barbieri, F. P. Campana, R. Kötz and R. Gallay, *Applied Physics A*, 2006, 82, 633-638.

119. M. M. Hantel, V. Presser, R. Kötz and Y. Gogotsi, *Electrochemistry Communications*, 2011, 13, 1221-1224.

120. P. W. Ruch, D. Cericola, M. Hahn, R. Kötz and A. Wokaun, *Journal of Electroanalytical Chemistry*, 2009, 636, 128-131.

121. M. Hahn, O. Barbieri, R. Gallay and R. Kötz, *Carbon*, 2006, 44, 2523-2533.

122. M. Winter, G. H. Wrodnigg, J. O. Besenhard, W. Biberacher and P. Novák, *Journal of The Electrochemical Society*, 2000, 147, 2427-2431.

123. N. Balke, S. Jesse, A. N. Morozovska, E. Eliseev, D. W. Chung, Y. Kim, L. Adamczyk, R. E. Garcia, N. Dudney and S. V. Kalinin, *Nature Nanotechnology*, 2010, 5, 749-754.

124. T. M. Arruda, M. Heon, V. Presser, P. C. Hillesheim, S. Dai, Y. Gogotsi, S. V. Kalinin and N. Balke, *Energy & Environmental Science*, 2013, 6, 225-231.

125. C. Merlet, B. Rotenberg, P. A. Madden, P. L. Taberna, P. Simon, Y. Gogotsi and M. Salanne, *Nature Materials*, 2012, 11, 306-310.

126. M. Z. Bazant, B. D. Storey and A. A. Kornyshev, *Physical Review Letters*, 2011, 106, 046102.

127. P. M. Biesheuvel and M. Z. Bazant, *Physical Review E*, 2010, 81, 031502.

128. P. M. Biesheuvel, Y. Fu and M. Z. Bazant, *Physical Review E*, 2011, 83, 061507.

129. P. L. Taberna, P. Simon and J. F. Fauvarque, *Journal of The Electrochemical Society*, 2003, 150, A292-A300.

130. P. L. Taberna, C. Portet and P. Simon, *Applied Physics A: Materials Science & Processing*, 2006, 82, 639-646.

131. C. Portet, P. L. Taberna, P. Simon and E. Flahaut, *Journal of The Electrochemical Society*, 2006, 153, A649-A653.

132.C. W. Shen, X. H. Wang, W. F. Zhang, F. Y. Kang and C. Du, Piscataway, NJ, USA, 2011.

133. Y. Q. Jiang, Q. Zhou and L. Lin, 2009.

# VITA

Min Heon minheon@gmail.com

## Education

Drexel University: Ph.D. in Materials Science and Engineering (2014)
POSTECH, South Korea: MS in Materials Science and Engineering (2000)
BS in Materials Science and Engineering (1998)

## Professional Experience

Senior Research Engineer, Samsung Corning, Suwon, South Korea (2000 –2007)

## Publications


- T. M. Arruda, **M. Heon**, V. Presser, P. C. Hillesheim, S. Dai, Y. Gogotsi, S. V. Kalinin, and N. Balke, "In situ tracking of the nanoscale expansion of porous carbon electrodes", Energy Environ. Sci., 6, 225-231, 2013
- B. Dyatkin, V. Presser, **M. Heon**, M. R. Lukatskaya, M. Beidaghi, Y. Gogotsi, Development of a "Green" Supercapacitor Composed Entirely of Environmentally Friendly Materials, ChemSusChem, 6, 2269-2280, 2013 (cover article)
- Mashtalir, M. Naguib, V. N. Mochalin, Y. Dall'agnese, **M. Heon**, M. W. Barsoum, Y. Gogotsi, Intercalation and Delamination of Layered Carbides, Nature Communications, 4, 1716, 2013
- P. Huang, **M. Heon**, D. Pech, M. Brunet, P.-L. Taberna, Y. Gogotsi, P. Simon, "On-chip Micro-supercapacitors from Carbide Derived Carbon Films", J. Power Sources, 225, 240-244, 2013
- F. Odeyemi, M. Pekker, A. Rabinovich, A. Fridman, **M. Heon**, V. N. Mochalin, Y. Gogotsi, "Low Temperature Plasma Reforming of Hydrocarbon Fuels Into Hydrogen and Carbon Suboxide for Energy Generation Without CO2 Emission", IEEE Transactions on Plasma Science, 40 (5) pp.1362-70, 2012
- **M. Heon**, S. Lofland, J. Applegate, R. Nolte, E. Cortes, J.D. Hettinger, P.-L. Taberna, P. Simon, P. Huang, M. Brunet, and Y. Gogotsi, "Continuous Carbide-derived Carbon Films with High Volumetric Capacitance", Energy Environ. Sci., 4 (1) pp.135-138, 2011
- V. Presser, **M. Heon**, and Y. Gogotsi, "Review : Carbide-Derived Carbons – From Porous Networks to Nanotubes and Graphene", Adv. Funct. Mater., 21 (5) pp.810-833, 2011
- M. Naguib, M. Kurtoglu, V. Presser, J. Lu, J. Niu, **M. Heon**, L. Hultman, Y. Gogotsi and M.W. Barsoum, "Two-Dimensional Nanocrystals Produced by Exfoliation of Ti3AlC2", Adv. Mater., 23 (37) pp.4248-4253, 2011
- K. Jost, C. R. Perez, J. McDonough, V. Presser, **M. Heon**, Y. Gogotsi, "Carbon coated textiles for flexible energy storage", Energy Environ. Sci., 4 (12) pp.5060-5067, 2011